Filament Morphology in Highly Magnetized Capacitively Coupled Low Temperature Plasmas

by

Stephen Williams

A dissertation submitted to the Graduate Faculty of
Auburn University
in partial fulfillment of the
requirements for the Degree of
Doctor of Philosophy

Auburn Alabama
August 5th, 2023

Keywords: Filamentation, Low-temperature Plasma, Self-organization, Magnetized Plasma

Approved by

Edward Thomas, Jr., Charles W. Barkley Endowed Professor of Physics and
Dean of the College of Science and Mathematics
Yu Lin, Alumni Professor
Uwe Konopka, Professor
Ryan Comes, Thomas and Jean Walter Associate Professor

Abstract

Due to the small charge-to-mass ratio of dust particles, it is often necessary to use large magnetic fields of B $\geq$ 1 T, in order to observe the influence of magnetic forces in laboratory dusty plasmas. However, when experiments are performed at high magnetic fields in capacitively coupled, low temperature, radio frequency discharges, the background plasma is often observed to form filamentary structures between the electrodes that are aligned to the external magnetic field which disrupt the uniformity of the plasma and adversely impact our dust experiments. The filament structures are observed as bright columns distinct from the background plasma that, when viewed from above, can take several distinct morphological shape geometries from circular, to multi-armed spirals. The morphology of the structures are dependent on plasma conditions including the neutral gas pressure and the strength of the magnetic field. Filaments and their morphologies are similarly observed in plasmas of different neutral gas types and experiments performed in the Magnetized Dusty Plasma Experiment (MDPX) device have identified and characterized these filamentary structures. Moreover, there is strong evidence that each spatial mode has a threshold condition that is dependent on the ion Hall parameter – which is a function of magnetic field, neutral pressure, and ion mass. The criteria for the formation of the filaments and their shape evolution are shown to be somewhat consistent with predictions of numerical simulations.

Acknowledgements

Oh my gosh...I honestly can’t wrap my head around the fact that this is actually happening. I would be remiss if I did not take the time to give my acknowledgements to my tribe that has helped me achieve this prestigious academic goal. If you know me, this section might be a doozey, but I am grateful that I have so many people to thank; so I will begin by quoting the immortal words of Samuel L. Jackson in one of my favorite movies ever made, ”Hold on to your butts”.

First and foremost, I would like to thank my mother Alisa Robinson! Ya’ll don’t understand how much she’s put up with. A lot of people are not fortunate enough to have the support of such a loving mother nor one who also has the patience to help a knucklehead like me out of stupid situations I got myself into. I would like to thank my grandparents Sara and James Robinson for to helping raise this knucklehead. I really wish they were here to experience milestone with me. They encouraged me from the start, and always expressed how proud they were of me every time they had the chance.

I would like to thank all of my mentors throughout my journey as a student. I would like to thank Dr. Andy Hollerman for taking a chance on a mathematics student who wanted to pursue a career in physics. I’d like to thank Father Phillip J. Linden for the countless life lessons and teaching me how to think critically in real-world situations. Lastly, I would like to extend my thanks and appreciation to Dr. Edward Thomas and Darrick Artis who each molded me into the physicist that I am today while simultaneously taking time out of their days to either push me, support me, or simply lend a listening ear. And Saikat, who helped me through many discussions in, and out of, the office. Oh, and Dr. Maurer for just being you. Haha thanks for that.

I also want to extend my greatest appreciation to my friends that have helped me keep pushing and giving me a space to unwind. From my Party Cruu, Jalaan Averitt (couch killer), Ali Fisher, Curtis Johnson, Omar Lopez (Dr. big strong boy), Nic Allen, Centucky, Ahmad Nemer (Dr. Daddy), and of course Tiny (I'll come back to you). My work husband Dr. Lori Scott, my Louisiana boy Spencer Leblanc (Dr. Sparky), Dr. Peter Traverso (Dr. Petey), Dr. Taylor Hall, and Dr. Richard Strom. The whole BGPSA group here at auburn, and my line brothers...we still going to those stars! Thank you, Hannah Brown, for keeping me on track by helping to maintain my productivity. Tiny, we've been though a lot to say the least, some good...mostly degenerate, but there's no one else I'd rather go through this experience with. You've been there for me every step of the way and I will never not be there for you.

Finally, thank you to all the staff that keeps me and the department in line. Mary Prater, Jennifer Morris, Glenda Stroud, you've all helped me tremendously. And to my cats Castiel and Crowley, your cuddles mean more than you know...but also, stop stepping on my laptop.

Contents

List of Figures

Introduction

Physics plasmas are a fourth state of matter following the well-known terrestrial phases of solid, liquid, and gas. Although they are only found in certain conditions on Earth, plasmas are the most common state of matter in the universe. Adding external energy to a solid system, typically in the form of heat, the system eventually reaches a critical point where is changes phase from solid to liquid. Continuing to add energy to the liquid system results in another phase change from liquid to gas. And continuing the trend of adding energy, one or more of the electrons in the gas atoms or molecules can be freed such that an electron-ion pair can be formed. When this process creates enough ionic pairs, the system forms a plasma. Because plasmas consist of positively charged ions and free electrons, the system is susceptible to electromagnetic fields. Therefore, in addition to gas-like properties, plasmas can also exhibit collective fluid-like motion under influence of electric and magnetic force fields.

Plasmas are studied today for numerous applications such as space, energy, health, and defense. Irving Langmuir first studied thermionic emission from heated tungsten filaments in inert gases [1], which ultimately led to his work with plasmas. At Auburn University, plasmas are produced and studied in a variety of ways. Some of these methods include fusion sciences, semi-conductors and etching, simulations for plasmas produced in space, and complex or ”dusty” plasmas. It follow that understanding plasmas and how to manage their properties for specific purposes is essential to moving science forward.

This dissertation will focus specifically on capacitively coupled low-temperature plasmas (LTP) in a high magnetic field environment. The magnetic fields are produced by the 4 Tesla class superconducting magnet housed in the Magnetized Plasma Research Lab (MPRL). This superconducting magnet is known as the Magnetized Dusty Plasma Experiment device (MDPX) and is designed to allow for plasma experiments with uniform magnetic field strengths of up to 4 T.

The plasmas generated in this work are composed of plasma densities and temperatures on the order of plasmas observed in the aurora borealis on the magnetic poles. The application of high magnetic fields on these LTPs results in the formation of self-organized structures at certain conditions. This research will provide insight into the formation of the imposed ordered structures, new analysis techniques for the characterization of the structures, and the morphological changes of the structures in magnetization space. Lastly, evidence of a relation of the structure sizes to well-known physical parameters will be presented.

Chapter 1

Theory and Background

The physical properties of complex plasmas have been studied in great detail in radio frequency (rf) plasmas. These complex, or dusty systems consist of ions, electrons and microparticles (dust) that range from tens of micrometers to a few nanometers in diameter [2, 3]. Because the electrons are much lighter and have a much higher mobility compared to their ion counterparts, the microparticles collect electrons and thus become negatively charged, under typical laboratory conditions [4]. The large electrostatic charge on the dust particles leads to coupling between particles in the system. Moreover the behaviors exhibited can range from a weakly coupled, gaseous-like state [3, 4], to a strongly coupled, crystalline-like state [3, 4]. Complex dusty plasmas allow for direct visualization of a wide variety of self-organized phenomena on macroscopic scales over relatively long time frames [3, 4, 5].

The self-organization of the coupled dusty plasma system has been studied extensively without the presence of external magnetic fields. However, a great deal of interest has grown in understanding the behavior of dust self-organization in a magnetic field environment. In next-generation fusion experiments with large B, dust production and dust dynamics may be a central concern [6, 7, 8]. Furthermore in astrophysical settings, the magnetic field can have a significant influence on dust dynamics by modifying charging, changing transport, etc. [9, 10, 11] Additionally, it is critical to know how the magnetic field modifies pattern formation of the dust system and the background plasma [12, 13].

In Section 1.1.3, the criteria necessary to accurately describe the magnetization of the dust particles will be formally defined. This criterion, known as the Hall parameter, allows us to describe a condition for magnetization that will scale linearly with magnetic field and inversely with atomic mass and neutral pressure. Therefore, to achieve the conditions necessary for dust magnetization, it is desirable to operate an experiment at high magnetic field in a uniform plasma at moderate pressures 1 to 15 Pa (10 mTorr to 120 mTorr). Due to the low charge-to-mass ratio of the dust grains, a large magnetic field ($B \geq 1T$) is necessary to magnetize the charged dust [14] (this will be discussed in further detail in the first section of chapter 2). Although operating at high magnetic fields is generally a requirement to achieve magnetization of the dust particles, under certain plasma conditions, the application of such large fields can lead to the formation of non-uniform structures in the background plasma [15, 16, 17].

The formation of these self-organized structures in the plasma that ultimately disrupt many of the plasma phenomena that we seek to study is referred to as plasma filamentation and has been observed previously as reported in the literature and depicted in figure 1.1 below [17].

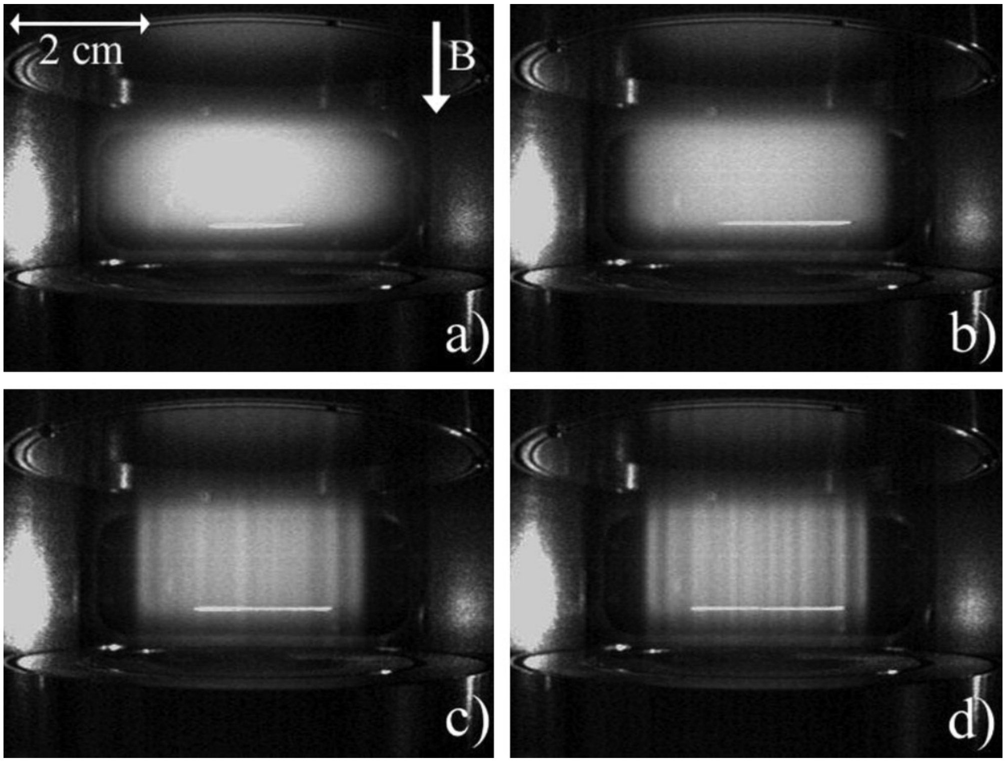

Figure 1.1: Plasma filamentation process in an argon plasma at Max Planck Institute at a pressure of 6 Pa in an experiment performed by Schwabe et. al [17]. The magnetic field is increased while images of the plasma are taken at (a) 0.0, (b) 0.5, (c) 1.0, and (d) 1.6 T. The bright horizontal line is produced by microparticles levitating in the plasma that are illuminated by laser light.

One of the earliest reported observation of the filamentation phenomenon was by Meirk Schwabe in 2011 from an experiment performed at the Max Planck Institute in Munich, Germany [17]. Here, the authors reported the filamentation process in their work with the addition of dust particles observed just above the lower electrode. For the experiment performed at Max Planck, the background plasma is viewed to be somewhat uniform with no field applied, but when exposed to a large field ($B \geq 0.5\ T$) vertical striations in the plasma begin to form that resemble bright columns aligned in the direction of the magnetic field. The filaments appeared in the plasma at low pressure ($p = 6\ Pa$) and low power applied. Filaments are shown in figure 1.1 from the side to emphasize the column structures that clearly form as magnetic field increases. Konopka et. al [15] also reported filamentation by imaging the plasma glow from above at similar plasma conditions with and without dust grains present. The authors also observed that if dust is present with the formation of filaments, the dust behavior and mobility change due to the structures present. Filamentation was also explored by P. Bandyopadhyay et. al [18].

Despite the fact that the initial experiments reported which featured plasma filamentation were designed for observations of magnetized dust grains, they demonstrated that the background plasma is also affected by the high field environment. Furthermore, the experiments show clearly that the plasma itself exhibits self-organizational behavior. Though this was an unexpected and a secondary result, it is the basis for this projected to be presented.

This dissertation focuses on the characterization and systematic evolution of filamentary structures that form in a capacitively coupled, rf-generated plasma at high magnetic field without the presence of dust particles. The goal of this work is the better understand the properties of these strongly magnetized plasmas in order to better understand how to perform dusty plasma studies at high magnetic field.

More recent experiments, which will be presented in this work, have shown the terminating end of filament structures viewed from above (i.e. filaments extending through the plasma and terminating on the top electrode). It will be demonstrated that the pattern formation of the filament structures evolve with pressure and magnetic field. Figure 1.2 illustrates the filament structures in MDPX when viewed from both the top and the side. From the side, filaments resemble the columns as seen in figure 1.1 above. However, from above, the filaments are seen to take different shapes in the same system.

1.1 Magnetization of the Plasma

A plasma (the fourth state of matter) is achieved by energizing the atoms (or molecules) in a gas such that the resulting system consists of neutral atoms and millions of free electron and positive ion pairs. Plasma systems range in internal energy from high temperature to low temperature and can also range from being highly ionized to being weakly ionized. The plasmas

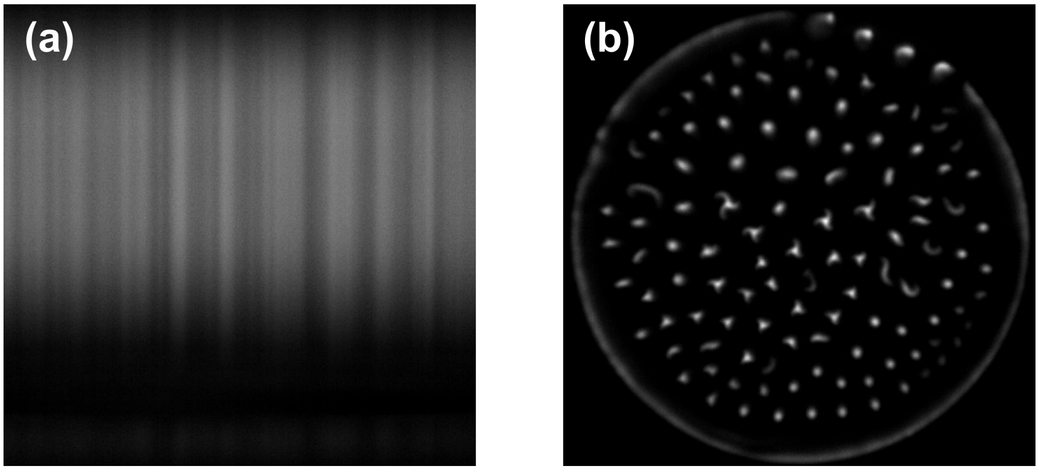

Figure 1.2: MDPX filaments viewed (a) from the side and (b) from above with the same pressure and magnetic field ($p = 3.5$ Pa and $B = 2$ T). With visible access to the plasma from the top, various shapes of filamentation are clearly seen which have not been viewed previously due to optical access to the plasma only allowed from the side.

developed in these studies are exclusively weakly ionized, low temperature plasmas which means the ionization fraction is on the order of one pair per million neutral atoms with generally cold, room temperature ions, $T_i \sim 0.025$ eV, and electron temperature typically 1 eV $\leq T_e \leq$ 5 eV. Because the plasma consists of charged particles, an applied electric or magnetic field will affect the motion of the charged particles and therefore the collective behavior of the plasma.

Particularly, in a magnetic field, charged particles exhibit gyromotion around the magnetic field lines which is dependent on the strength of the field applied. Since the presence of a magnetic field imposes gyromotion on the charged particles, it effectively changes their behavior from randomized motion to gyromotion trajectories in which the magnetic field can “guide” the drift of particles. Furthermore, the characteristics of the particle transport will be defined by a competition between the gyromotion, as defined by the Larmor radius, and the collision mean-free-path. The mean free path is the average distance a particle is able to travel before colliding into another particle. Since these low temperature plasmas consist of mainly neutral atoms, the probability of charged species collisions is quite low compared to collisions with neutrals. Apropos, the degree of magnetization of ions/electrons is highly dependent on the motion of the charged particles around the magnetic field lines relative to their collisions with a neutral atom.

1.1.1 Gyromotion

The gyromotion and mean free path quantities are very well known and discussed in physics classrooms as well as textbooks such as Francis F. Chen *Introduction to Plasma Physics and Controlled Fusion* [19]. It is essential to introduce these two concepts in depth due to their essential role they play in the magnetization of the plasma. To present the gyromotion first, it is derived from the Lorentz force. For a force, F, a magnetic field, B, and a particle of mass, m, with charge q,

$$F = q\,\mathbf{v} \times \mathbf{B} = m\frac{d\mathbf{v}}{dt} \tag{1.1}$$

Generally the direction of **B** is taken as being uniform in the z-direction, which is applicable to the experiment presented in the next chapter. Therefore, with $\mathbf{B} = B_z$,

$$m\dot{v}_x = qBv_y \tag{1.2}$$

$$m\dot{v}_y = -qBv_x \tag{1.3}$$

$$m\dot{v}_z = 0 \tag{1.4}$$

Taking the derivative of the equations above and solving for the second derivative terms gives,

$$\ddot{v}_x = \frac{qB}{m}\dot{v}_y = -\left(\frac{qB}{m}\right)^2 v_x \tag{1.5}$$

$$\ddot{v}_y = -\frac{qB}{m}\dot{v}_x = -\left(\frac{qB}{m}\right)^2 v_y \tag{1.6}$$

In the absence of any other force terms, the equations above are in the same form as the fundamental simple harmonic oscillator. Therefore we can define a *cyclotron frequency*, ω_c as

$$\omega_c \equiv \frac{|q|B}{m} \tag{1.7}$$

This describes how many revolutions around a central axis the charged particle will complete in a collisionless system per second (in units of rad/s). Moreover there is a simple harmonic motion solution to Eq[1.5] and [1.6] in the form of

$$v_{x,y} = v_{\perp} exp(\pm i\omega_c t + i\delta_{x,y}) \tag{1.8}$$

where $v_{\perp}$ is the velocity perpendicular to the direction of the magnetic field. From here we can set the phase $\delta = 0$ such that

$$v_x = v_{\perp} e^{i\omega_c t} = \dot{x} \tag{1.9}$$

Using Eq [1.6], it follows that the velocity can be placed in terms of the cyclotron frequency as well such that

$$v_y = \frac{m}{qB}\dot{v}_x = \pm\frac{1}{\omega_c}\dot{v}_x = \pm i v_{\perp} e^{i\omega_c t} = \dot{y} \tag{1.10}$$

Integrating velocities in Eq [1.9] and [1.10] gives position in terms of ω_c where

$$x - x_0 = -i\frac{v_{\perp}}{\omega_c} e^{i\omega_c t} \tag{1.11}$$

$$y - y_0 = \pm\frac{v_{\perp}}{\omega_c} e^{i\omega_c t} \tag{1.12}$$

with $(x_o,\ y_0)$ as an origin point. Finally we can define a *Larmor radius* or *gyroradius* to be

$$\mathbf{r_L} \equiv \frac{v_{\perp}}{\omega_c} = \frac{m v_{\perp}}{|q|B} \tag{1.13}$$

where the value of $\mathbf{r_L}$ represents the radial distance the charged particle reaches from the central axis during its motion. Thus the gyromotion of a charged particle in a magnetic field can be described with the cyclotron frequency and the Larmor (gyro) radius.

1.1.2 Mean Free Path

In a plasma, there are at least three separate species that populate the system; free electrons, ions, and neutral atoms. As these species of particles move around in the system there is a statistical probability that two particles may collide at some location in time. Therefore the *mean free path* is a quantity used to describe the average distance a particle will travel before colliding with another particle in the system. In a weakly ionized plasma, the probability that a charged particle collides with a neutral atom is much higher than the probability of colliding with another charged particle; meaning that neutral collisions dominate the system. The following derivation for mean free path is based on chapter 5 of Chen [19].

Assume a slab of area A and thickness dx which contains n_n number of neutral atoms per cubic meter (m^3). All are assumed to have a spherical cross-sectional area σ. Therefore the number of atoms in the slab is

$$n_n A_x dx \tag{1.14}$$

The fraction of the area slab that is blocked by the atoms is

$$n_n \sigma dx \tag{1.15}$$

The flux of electrons (or ions) incident on the slab and passing through on the other side is

$$\Gamma'_{e,i} = \Gamma_{e,i}(1 - n_n \sigma dx) \tag{1.16}$$

And the change of $\Gamma_{e,i}$ with distance is

$$\frac{d\Gamma_{e,i}}{dx} = -n_n \sigma \Gamma_{e,i} \tag{1.17}$$

and can be interpreted as the change in flux with the change in slab thickness. One can integrate Eq[1.16] to reach the following form for the flux such that

$$\Gamma_{e,i} = \Gamma_{0(e,i)} e^{-n_n \sigma x} \equiv \Gamma_{0(e,i)} e^{-x/\lambda_{mfp}} \tag{1.18}$$

Finally we arrive at the mean free path quantity λ_{mfp} with

$$\lambda_{mfp} = 1/n_n \sigma \tag{1.19}$$

This is the average distance traveled before making a collision most likely with a neutral. In other words, after traveling a distance of λ_{mfp}, a particle will have a good probability of making a collision.

It is necessary to determine the value of the collision cross-section of σ in the context of neutral collisions. When it comes to ion-neutral collision cross-sections in weakly ionized low temperature plasmas, there is not much information available because of the complexity of the cross-section calculations. Additionally, since argon is most widely and commonly used for laboratory plasmas, much focus is not given to other plasmas when it comes to the ion-neutral collision cross-section.

It follows that the mean-free path is inversely proportional to the collision cross-section and depends on the mass of the neutral atoms. According to Khrapak, the ion-neutral collisional cross-section for room temperature argon is $2.06 \times 10^{-14}\ cm^2$ [20]. In the report, Khrapak defines the ion thermal velocity as $\sqrt{k_b T_i / m_i}$, but when the three dimensional Maxwell-Boltzmann distribution is applied, the expectation value of the atomic (ion) velocities is given by $\sqrt{8 k_b T_i / \pi m_i}$. Therefore to describe the full plasma system, a factor of $\sqrt{8/\pi}$ is included to the collision cross-section calculation and, when converted to units of m^2, the value of $3.28 \times 10^{-18}\ m^2$ is obtained. This is the ion-neutral collision cross-sectional value applied to the mean-free path calculation in argon.

Khrapak gives values for He^+ in He, Ne^+ in Ne, and Ar^+ in Ar but because the experiments described in chapters 3 and 4 include krypton plasmas, a cross-section is needed for krypton as well. Moreover, to have a universal value for the ion-neutral collision cross-section in order for later Hall parameter comparison (the Hall parameter will be discussed in the next section) is necessary.

Therefore, the Phelps database was used to determine that value with the data retreived from lxcat on October 12, 2022 [21]. The figure below shows the values for the ion-neutral collision cross-section for different ion temperatures for the three ion-neutral pairs (He^+/He, Ar^+/Ar, and Xe^+/Xe) represented in yellow, blue, and green respectively. The light blue range indicates the range of ion temperatures from 0.01 to 0.1 eV while red value is the average value of the three pairs within that energy range. From this, the value of sigma that was selected was $\sigma = 1.14 \times 10^{-18}\ m^2$. This value corresponds with the typical ion temperature in all MDPX plasmas in this work - which is 0.025 eV (i.e. room temperature).

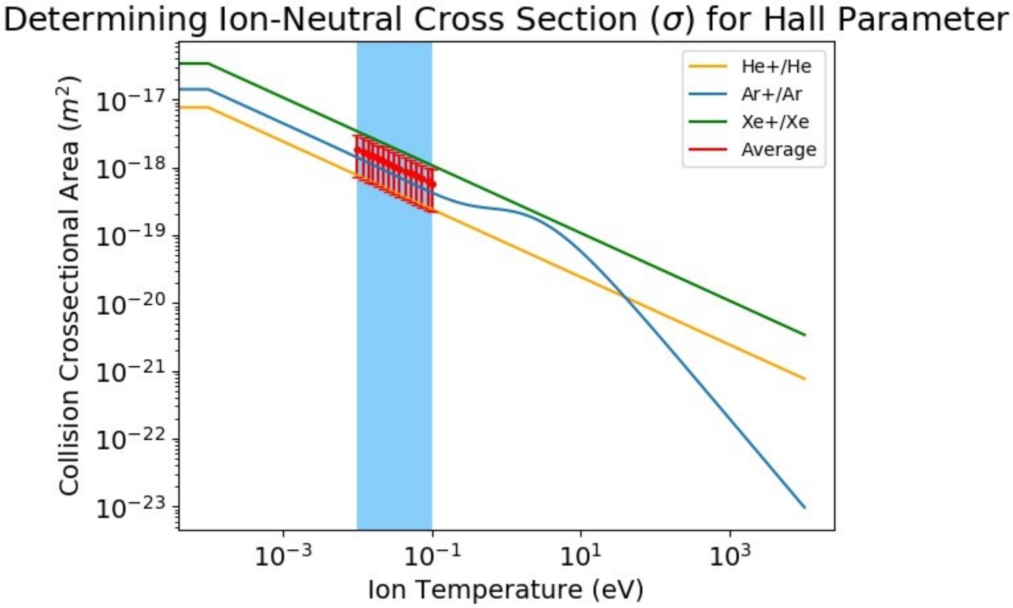

Figure 1.3: Phelps database retrieved on Oct 12, 2022 from www.lxcat.net [21] used to determine a "universal" ion-neutral cross sectional area, σ, for the different masses. The value for the universal σ was determined to be 1.14×10^{-18} m^2

Just as in the previous section, the mean free path describes a distance but a collision frequency is also associated with this notion. When a particle does collide with another, the momentum changes and it is a matter of time (and distance) for it to make another collision. Thus the time between collisions can be written as

$$\tau = \lambda_{mfp}/v \tag{1.20}$$

for particles of velocity, v. Then taking the inverse of the time gives a frequency of collisions to be

$$\tau^{-1} = v/\lambda_{mfp} = v n_n \sigma \tag{1.21}$$

Lastly, assuming the charged particles are Maxwellian and averaging the velocities, we can present the collision frequency ν as

$$\nu = n_n \sigma v_{th} \tag{1.22}$$

where v_{th} is the particle thermal velocity. The collision frequency represents the average number of collisions a particle makes in a second. Of course, the more neutral atoms there are, or the higher the velocity of the particle, the more collisions it will make in the system. This notion is extremely important when estimating the degree of magnetization of a particle is when an external magnetic field is introduced. The idea of magnetization is embodied in a dimensionless quantity called the Hall parameter, which will be described in the next section.

1.1.3 Hall Parameter

The Hall parameter has been utilized in previous reported experiments performed on the Magnetized Dusty Plasma Experiment (MDPX) device [22, 23, 24]. It is used as a parameter to quantify the degree in which a charged particle can be considered magnetized. Understanding the magnetization of a charged species is imperative in filamentation experiments. Using the concepts introduced in sections 1.1.1 and 1.1.2 above, a form for the Hall parameter is written in terms of frequencies as

$$H_s = \frac{\omega_{c,s}}{\nu_{n,s}} \tag{1.23}$$

with the subscript, s, representing the particular species of either ion or electron. This ratio of frequencies can be interpreted as the number of rotations around a central axis compared to the number of collisions made. To completely describe this notion, we take note that the gyrofrequency is the number of rotations (i.e. revolutions) performed per second. Formally, the gyrofrequency is an angular velocity (rad/sec) and a collision frequency is a true frequency (Hz). To "normalize" the units between the two quantities, a factor of 2π is introduced to the collision frequency to have a modified Hall parameter given by:

$$H'_s = \frac{\omega_{c,s}}{2\pi\nu_{n,s}} \tag{1.24}$$

Similarly, we can also represent the Hall parameter in terms of distances as a ratio of the mean free path and gyroradius.

$$H_s = \frac{\lambda_{mfp,s}}{\rho_s} \tag{1.25}$$

However just as in the case of the frequency representation, the distance also requires a factor of 2π in the denominator due to the fact that the gyroradius does not completely describe the path of the charged particle. Since the path truly traversed by the particle is the circumference of the circle the gyroradius describes, the path is truly represented as $2\pi\rho$. Thus, we again arrive at the form for the modified Hall parameter such that

$$H'_s = \frac{\lambda_{mfp,s}}{2\pi\rho_s} \tag{1.26}$$

For the purposes of this work, the modified Hall parameter will used to define the degree of magnetization. Additionally, we assume the cross-section does not appreciably change with magnetic field. This same approach was taken by M. Schwabe to define the magnetization of charged particle species in argon [17]

Recall that the cyclotron frequency $\omega_{c,s} = \frac{qB}{m_s}$ and the collision frequency $\nu = n_n\sigma_{i-n}v_{th,s}$ and give,

$$H_s = \frac{qB}{2\pi m n_n \sigma_{i-n} v_{th,s}} \tag{1.27}$$

The Hall parameter is quite useful for the experiment that will be described in the following chapters because the quantity scales with magnetic field and pressure, which are the two main control variables for the system. This scaling can be easily seen when written in this form with

$$H_s = \left(\frac{q}{2\pi m \sigma_{i-n} v_{th,s}}\right)\left(\frac{B}{n_n}\right) \propto \frac{B}{p} \tag{1.28}$$

since pressure is effectively the number of neutral atoms per unit volume.

1.2 Qualitative Filament Theory

Stationary and local Plasma filamentation has been observed in a few experiments [15, 16, 17, 18], however, the underlying physical processes are not yet well understood. Observations of very similar behavior such as shear-flow instabilities of the global plasma system under the influence of magnetic fields has also been reported [25, 26]. With laboratory experimentation potentially sharing a common phenomenon, it follows that a theoretical framework may help describe the plasma behaviors reported.

1.2.1 Filament Simulation in MDPX

The MDPX device at Auburn University is a unique device in that a very high (up to 4 T) magnetic field can be applied to a weakly ionized capacitively coupled plasma (CCP). Moreover, plasma filamentation has only been observed in similar systems that generate high fields which are not very common. As a result, it was not until recently (in the last 3-4 years) that a simulation was developed to model the particular conditions in MDPX. In 2019, M. Menati et. al [27] developed the first simple characteristic model of filaments. This early model investigated how an argon plasma becomes filamented in an increasing magnetic field. The author's simulations compared how the electron density and Ar(4P) density (surrogate for optical emission), in MDPX conditions, respond to the applied magnetic field strengths. In figures 1.4 and 1.5 [27], the authors show that over a range of magnetic field ($0 \leq B \leq 6000\ G$ (0 - 0.6 T), the electron and Ar(4p) densities transition from smooth to striated discharges.

The simulations are consistent with experimental observations of a filamented plasma from the side such as the observations presented in figure 1.1 at Max Plank. Filament observations in the MDPX device with the same plasma conditions as implimented in the simulation code is seen in figure 1.6.

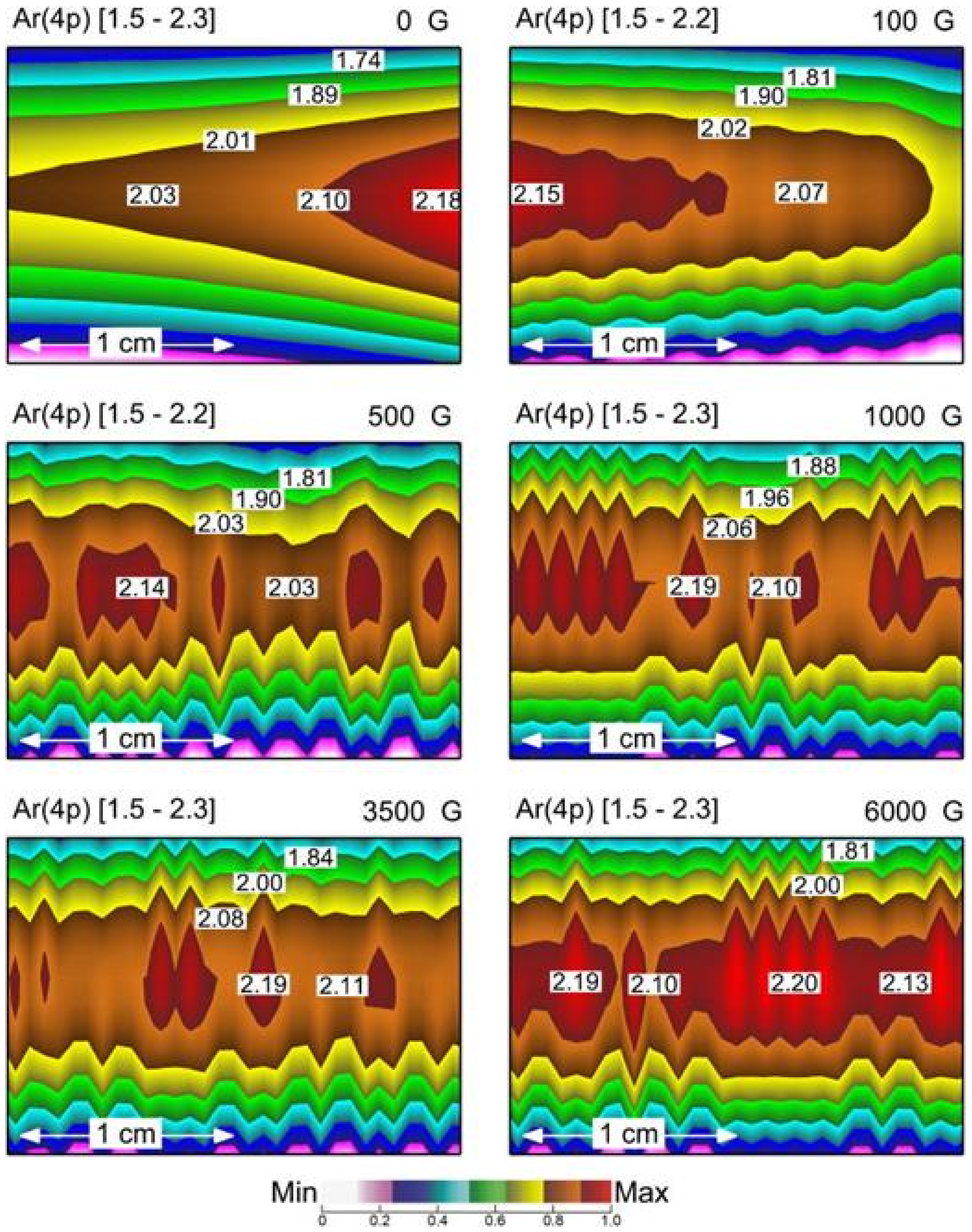

Figure 1.4: Simulation by Menati et. al [27] illustrating the transition of the Ar(4p) density from smooth to striated as a function of axial magnetic field strength, $\mathbf{B_z = 0 - 6000\ G\ (0.6\ T)}$

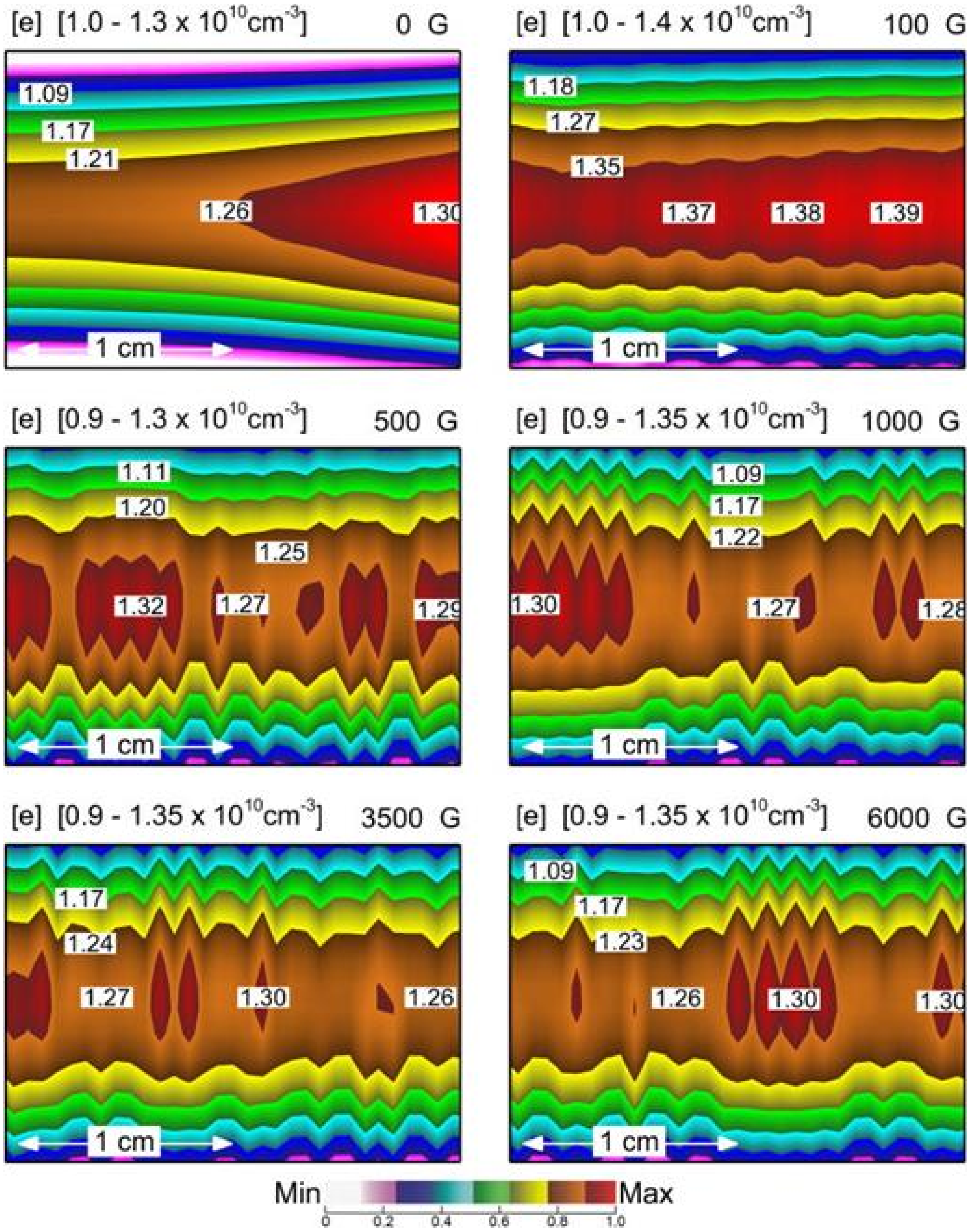

Figure 1.5: Simulation by Menati et. al [27] illustrating the transition of the electron density from smooth to striated as a function of axial magnetic field strength, $\mathbf{B_z = 0 - 6000}$ G $(\mathbf{0.6}$ T$)$

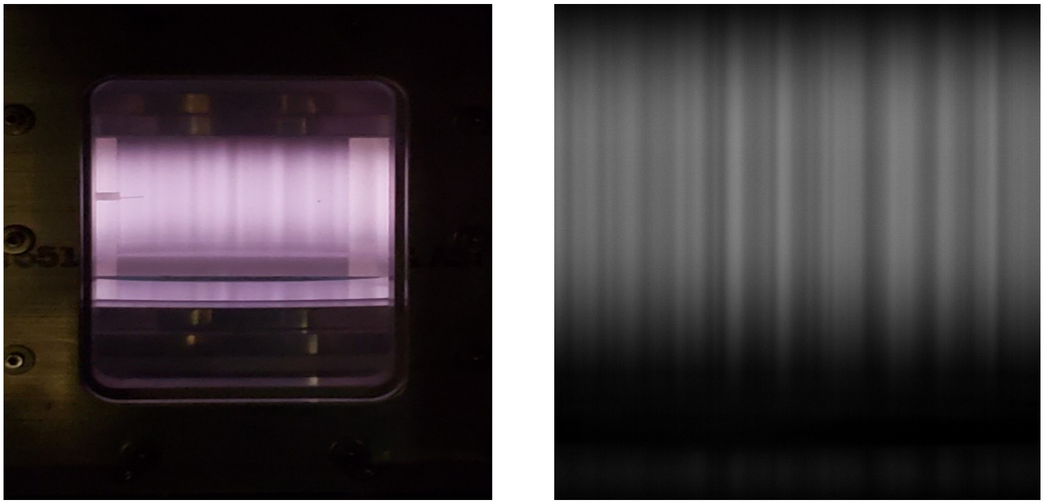

Figure 1.6: Images of the MDPX argon plasma as viewed from the side in a 1 T (10^4 G) magnetic field. The left image is taken with a typical RGB camera, while the image on the right is taken with a Ximea 4 MP monochromatic camera.

The results from the early 2D model by Menati were successful in that it captured the plasma filamentation columns forming in the system from a side view. Because of the success of these results, a new 3D numerical fluid model was rendered to give a more complete picture of the formation of filaments within the plasma. The new model developed by Menati et. al [28] incorporates the dynamics of the ions and electrons subject to neutral collisions and seeks to determine how the interactions lead to filamentary structures aligned parallel to the magnetic field.

The model solves the Poisson equation everywhere in the volume to calculate the electric potential at each point. Then the electric field is calculated and subsequently used in the momentum equation and ion/electron fluxes. Lastly the continuity equation is solved to maintain quasineutrality if there are any losses. It should be noted that the numerical model uses a simulation time step of 10^{-11} s in order to keep the time steps shorter than the dialectric relaxation time of the plasma [29]. With this short of a time step, it becomes computationally expensive in terms of run time and available memory. Therefore, the simulations are stopped at 40 μs which is efficient to replicate the formation of the filaments even though the lifetime of individual filaments can last for an extended amount of time. The figure below shows similar results to figures 1.4 and 1.5 as filament formation is viewed from the side and very closely resembles the images taken in figure 1.6. It shows the progression of the system at different times with a magnetic field of $B = 1$ T and a pressure, $p = 10$ Pa.

The model produces filaments of various shapes, and allows us to visualize them from above. Figure 1.7 is a series of predictive images produced by the algorithm of a single filament structure from looking at the electron density profile at a magnetic field of $B = 1$ T for three different pressures. The evolution of the shape of the filament changes from a three-arm spiral, to 4-arm, to circular with increasing pressure. The circular and three-arm spiral filaments are observed in argon plasmas as seen in figure 1.2, and the 4-arm spiral is observed in Krypton plasmas (see figure 4.10).

The simulations were developed between late 2019 and early 2020, predicting filament shapes in the system and their dependencies on magnetic

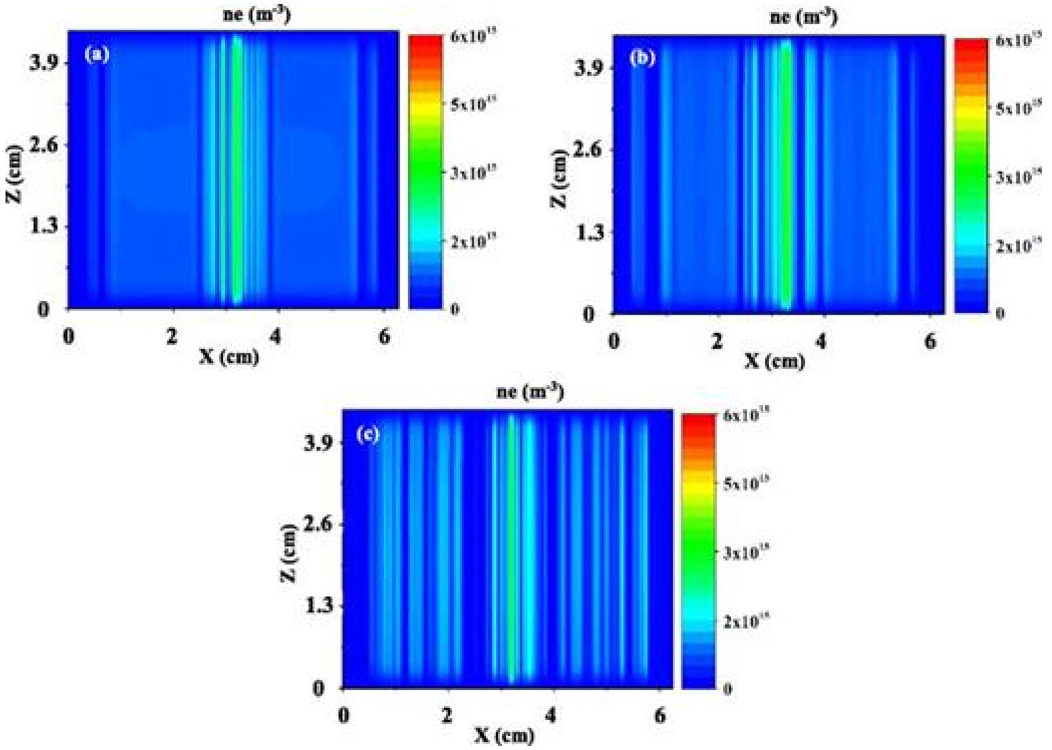

Figure 1.7: Presented by Menati et. al [28], a side view of the evolution of filament formation in an MDPX plasma at three different time stamps (a) 20 μs (b) 30 μs and (c) 40 μs.

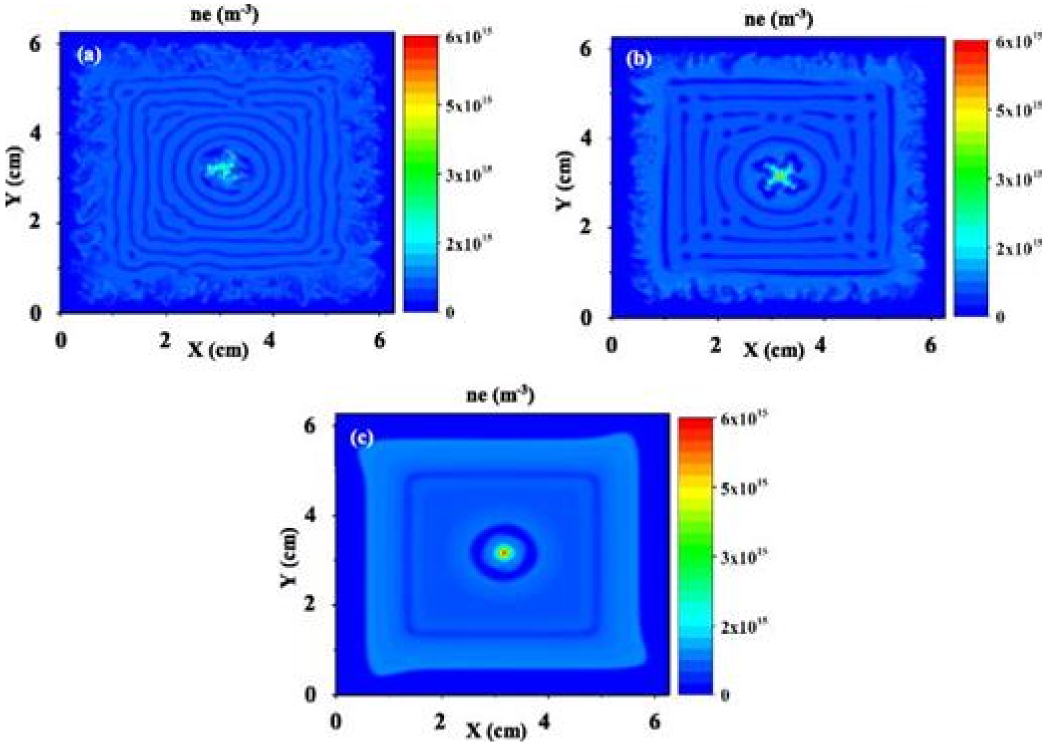

Figure 1.8: Presented by Menati et. al [28], a top view of the electron density profile in an MDPX plasma at a magnetic field of $B = 1$ T. The filaments are shown at pressures of (a) 5 Pa, (b) 10 Pa, (c) 20 Pa.

field and pressure. At the time, the only image of filaments recorded from above, which was provided by Konopka et. al [15] in 2005, showed only the presence of circular filaments when viewed from above. It was not reported until 2022 that experiments performed by S. Williams et. al [30] characterized the morphology of the filament structures from above, confirming the predictions of the model developed two years earlier.

Although simulations were confirmed through the experiments performed by Williams et. al, there is still no theory that exists to describe in detail the physical processes that lead to the formation of these structures or their interactions with the background plasma and other filaments. Therefore, it is obvious that a basic theoretical framework should be considered to potentially provide physical insight for the formation of filaments in a magnetized plasma. And, it may be beneficial to begin with an exploration of the processes that form the spiral filaments because the extension of the arms out from the center may give additional clues to some of the dynamics that lead to the formation of the self-organized structures.

1.2.2 A Model for Spiral Stuctures in Plasmas

Spiral structures in magnetized plasmas are not limited to filaments found in the MDPX plasmas. Although found on a larger scale, magnetized plasmas have been observed to show a global stationary and/or rotating spiral structures. Since filament theory is in the process of being developed, using a theory already developed for rotating magnetized plasmas may provide useful insights to understand the filament formation process in the MDPX device. The framework for this model is based on the observations of stationary spiral patterns observed in an argon electron cyclotron resonance (ECR) plasma [31]. As a result, Mitsuo Kono and Masayoshi Tanaka developed a theoretical model for stationary spiral patterns in an ECR plasma [32] based on an experiment performed by Okamoto et. al [31] where the authors observed multiple spontaneous vortices self-organize in a rotating ECR plasma. We will show that the model of Kono and Tanaka, when scaled to conditions in the MDPX device, leads to results that have a qualitative form similar to the experimental observations and may provide some helpful insights into the physical processes that lead to the formation of filamentary structures. Filament theory based on the ECR model from Kono and Tanaka [32] will be left for future development.

The theoretical model presented solves the coupled set of continuity and momentum fluid equations shown below (respectively)

$$\frac{\partial n_s}{\partial t} + \nabla(n_s \mathbf{v}_s) = 0 \tag{1.29}$$

$$\frac{\partial \mathbf{v}_s}{\partial t} + \mathbf{v}_s \cdot \nabla \mathbf{v}_s = \frac{e_s}{m_s}\left(-\nabla\phi + \frac{1}{c}\mathbf{v}_s \times \mathbf{B}\right) - \delta_{s,e}\frac{1}{nm_s}\nabla p_s - \nu_s \mathbf{v}_s \tag{1.30}$$

where n_s, $\mathbf{v}_s$, and ν_s (s is the species, either ion or electron) are the density, velocity, collision frequency of ions and electrons with neutrals, and ϕ is the plasma potential. The model assumes the formation of a rotating, sheared, cylindrical column with radial and axial coordinates, r and z, respectively, and will assume an azimuthal rotation in the theta direction with a mode number l. The density, potential, and velocity are separated into stationary parts and fluctuation parts:

$$\begin{pmatrix} n \\ \phi \\ \mathbf{v} \end{pmatrix} = \begin{pmatrix} n_0(r,z) \\ \phi_0(r,z) \\ \mathbf{v}_0(r,z) \end{pmatrix} + \Sigma \begin{pmatrix} n_l(r,z) \\ \phi_l(r,z) \\ \mathbf{v}_l(r,z) \end{pmatrix} e^{i(l\theta-\omega t)} + c$$

Thus, a form for the fluctuating parts of the ion and electron velocities in radial, azimuthal (with l being the mode number), and axial components can be written and substituted into the continuity equation Eq[1.27]. Then invoking quasineutrality ($n_{l,i} = n_{l,e} = n_l$) and assuming the axial dependence of the potential with normalizations $\xi = r/r_d$ and $\eta = z/r_d$, where r_d is the plasma radius, is

$$\phi(\xi,\eta) = \phi_l(\eta)e^{-(\kappa-ik)\eta} \tag{1.31}$$

They derived a second-order differential equation of the potential as

$$\frac{d^2\phi_l}{d\xi^2} + \left[\frac{1}{\xi} + \frac{dln(n_0)}{d\xi}\right]\frac{d\phi_l}{d\xi} + \left[\beta(\xi) - \frac{l^2}{\xi^2}\right]\phi_l = 0 \tag{1.32}$$

with $\beta(\xi)$ incorporating the drift wave instability, flute mode instability (the gravitational instability due to the centrifugal force acting on the ions), and the Kelvin-Helmholtz instability terms. Further investigation from the authors show that the main contributor to the spiral pattern formed in the Okamoto experiment is the drift wave instability that is driven by the radial density gradient across the rotating "column" of plasma in the system. This is because when the contributions from the centrifugal and Kelvin-Helmholtz instabilities are neglected, the spiral pattern still forms with no significant change.

With the density profile assumed to be Gaussian ($n_0(r)$), both stationary and rotating spiral solutions are found with the calculations. Figure 1.8 illustrates the numerical results for the stationary solution (for $l = 2$). Figure 1.9(a) depicts the radial potential profile of the system with the normalized potential ($e\phi/T_e$) as a function of η. While 1.8(b) depicts the density perturbation contour that resembles a two-arm spiral.

The thermal energy stored in the non-uniform plasma gives rise to the drift wave instability that then spreads outward across the uniform magnetic field. Because the plasma is non-uniform, the differences in density and velocity lead to shear and hence a phase difference between real and imaginary parts (i.e. eigenfunctions) which drive the spiral pattern. Unlike flute mode instabilities, the drift wave instability has finite wavelengths along the field. Additionally the plasma motion is decoupled from the magnetic field so there in no energetically unfavorable bending of the field lines. Furthermore, the notion of drift waves being the prominent instability in the system which gives rise to a self-organized structure is consistent with experiments because it is stabilized by an increase in collisions with neutrals (i.e. an increase in neutral pressure). This is also observed with MDPX filaments in which above a certain neutral pressure, filaments no longer exist in the system.

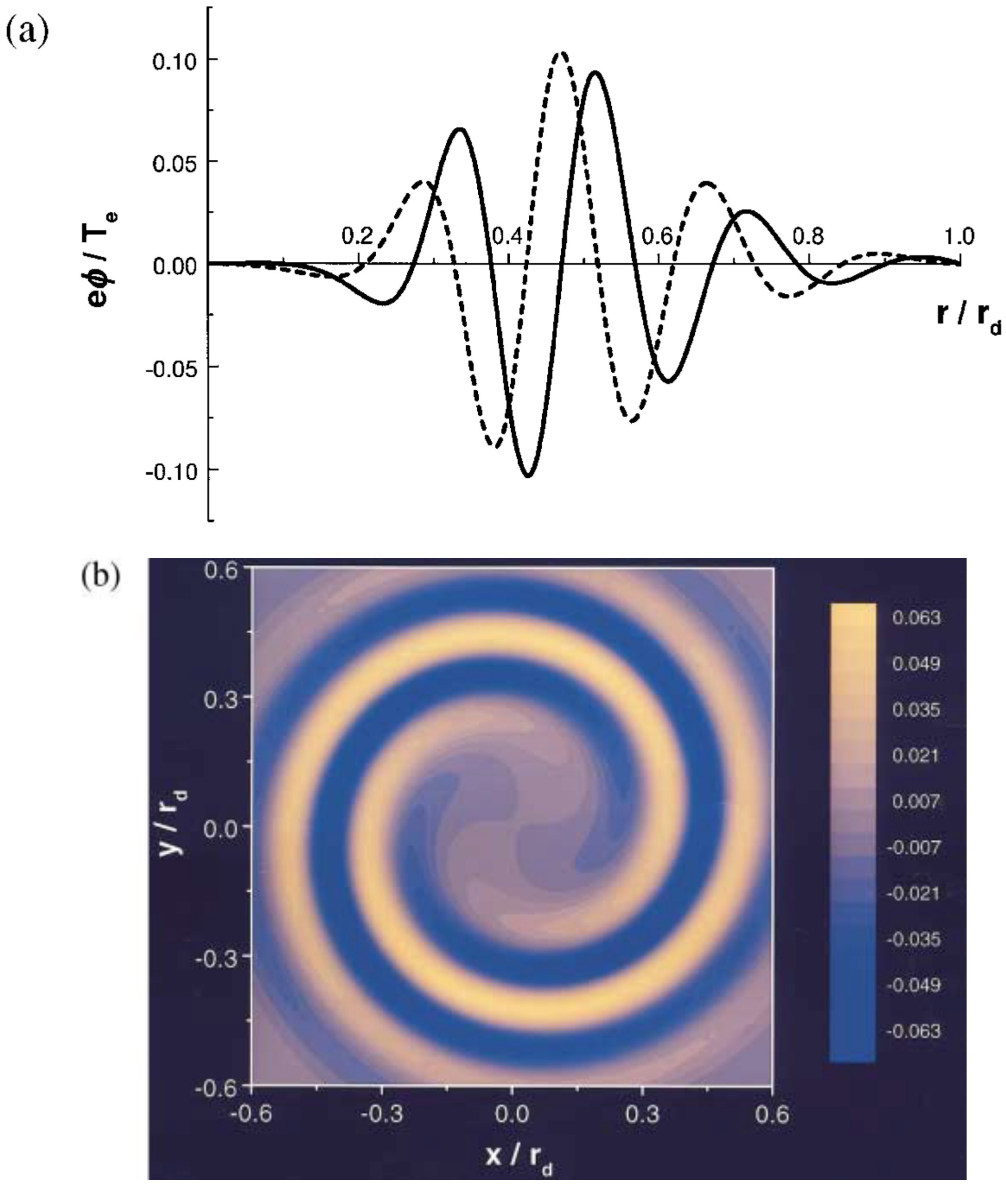

Figure 1.9: The numerical result of a stationary spiral solution given by Kono and Tanaka [32] in an argon plasma ($\mathbf{M_i/m_e = 80,000}$), with $\kappa = \mathbf{0.067}$, wavenumber $\mathbf{k = 0.0225}$, and the ratio of drift wave frequency to gyrofrequency $\gamma/\ = \mathbf{0.024}$.(a) The radial profile of the perturbed potential $\phi_l(\xi)$ where the solid line represents the real part and the dotted line represents the imaginary part. (b) The density perturbation contour $\mathbf{Re[(n_l/n_0)exp(il\theta)]}$.

In the next section, we will incorporate the drift wave spiral equations into a mathematica code under MDPX conditions in which filaments are formed to determine if the numerical model gives qualitatively similar results to what has been observed in experiments.

1.2.3 Mathematica Code

With the success of the theory applied to stationary spiral structures observed in magnetized ECR plasmas whose overall structure depends on plasma conditions, it follows that we try to begin to apply these same ideas to the MDPX CCP filaments. The first approach is to take the results from the Kono and Tanaka paper and use the solution as a test to see if we can recreate similar spirals simulated in our code developed in Mathematica.

Figure 1.9 below is an illustration of the Mathematica routine in which the plasma variables and constants are initiated and the spiral solution (Eq.[1.30]) is solved using the Ikehata and Tanaka experiment parameters [33, 34]. The spiral simulated is a representation of the density perturbation contour that arises from the 2D solution of the stationary $l = 2$ mode. The typical ECR magnetized argon plasma parameters were given with $B = 875$ G (0.875 T), $T_e = 5$ eV, $T_i = 0.025$ eV, plasma radius of 10 cm, pressure $p = 20$ mTorr, and $\omega_r = 0$ which is the stationary plasma condition. This Mathematica simulation is a proof of concept in our attempt to use the equations provided to begin to use the idea of drift wave instabilities to try to explain the pattern formation of the filaments.

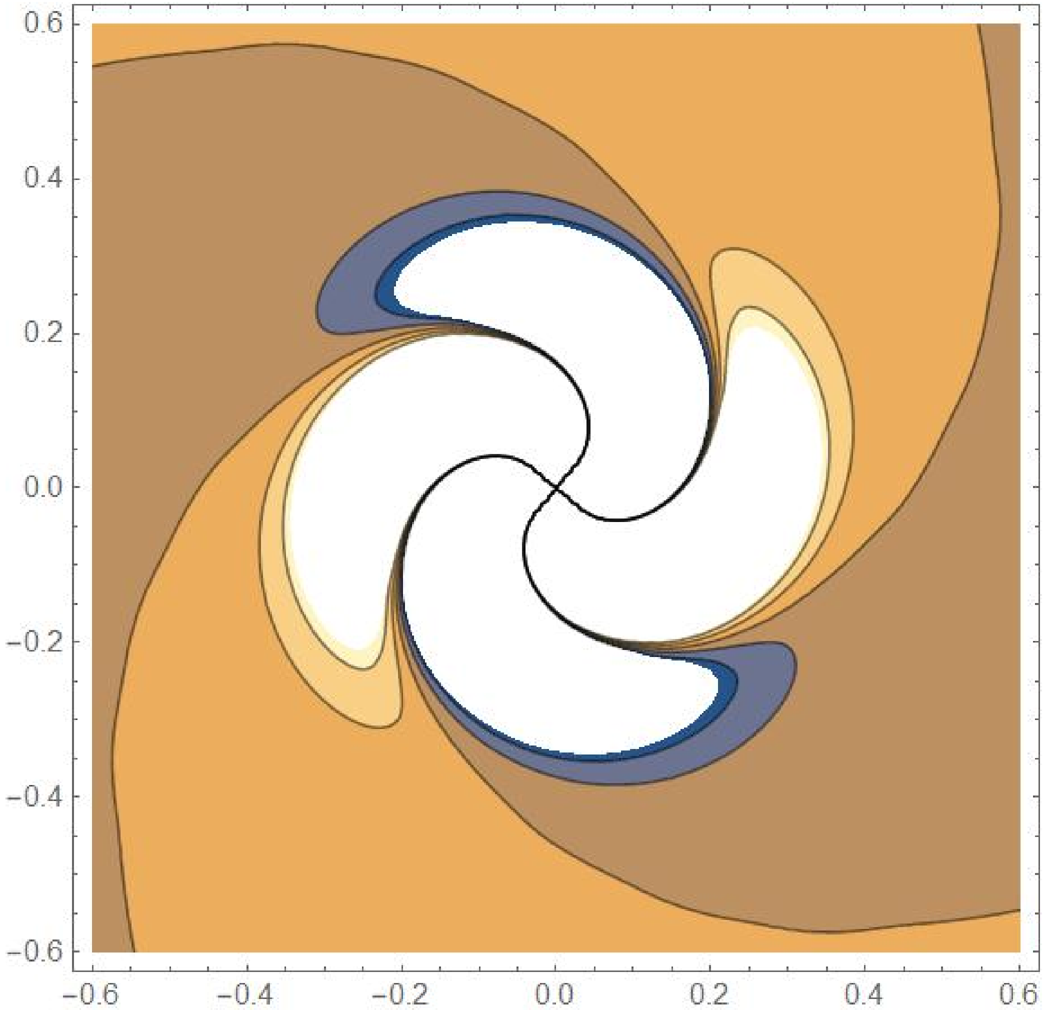

Figure 1.10: Numerical results for a stationary spiral solution with a Mathematica code to recreate a similar spiral as presented in figure 1.8(b) under very similar conditions as proof of concept. The real and imaginary parts are shown here (in blue and yellow respectively) for the $\mathbf{l = 2}$ mode.

We apply the filament conditions to the Mathematica simulation to investigate the result of the code for the different types (azimuthal modes) of filaments observed in the experiments such as a circular mode (m = 0) as well as spirals with various "arms" (m = 2, 3, 4, etc.) as a function of magnetic field strength and pressure. These various modes correspond to filament types that are observed in MDPX experiments for different magnetic field strengths that will be described in Chapters 3 and 4 of this dissertation. The figures below illustrate the solutions for the different density perturbation modes at various magnetic fields. The typical plasma parameters we have for the MDPX CCP system are $T_e = 3$ eV, $T_i = 0.025$ eV, effective filament diameter size of 3 mm, and the pressure range given was $30 \leq p \leq 40$ mTorr ($4 \leq 5.3$ Pa), with $\omega_r = 10$ for slight global $E \times B$ rotation. The blue contours indicate real solutions while the orange contours indicate the imaginary parts.

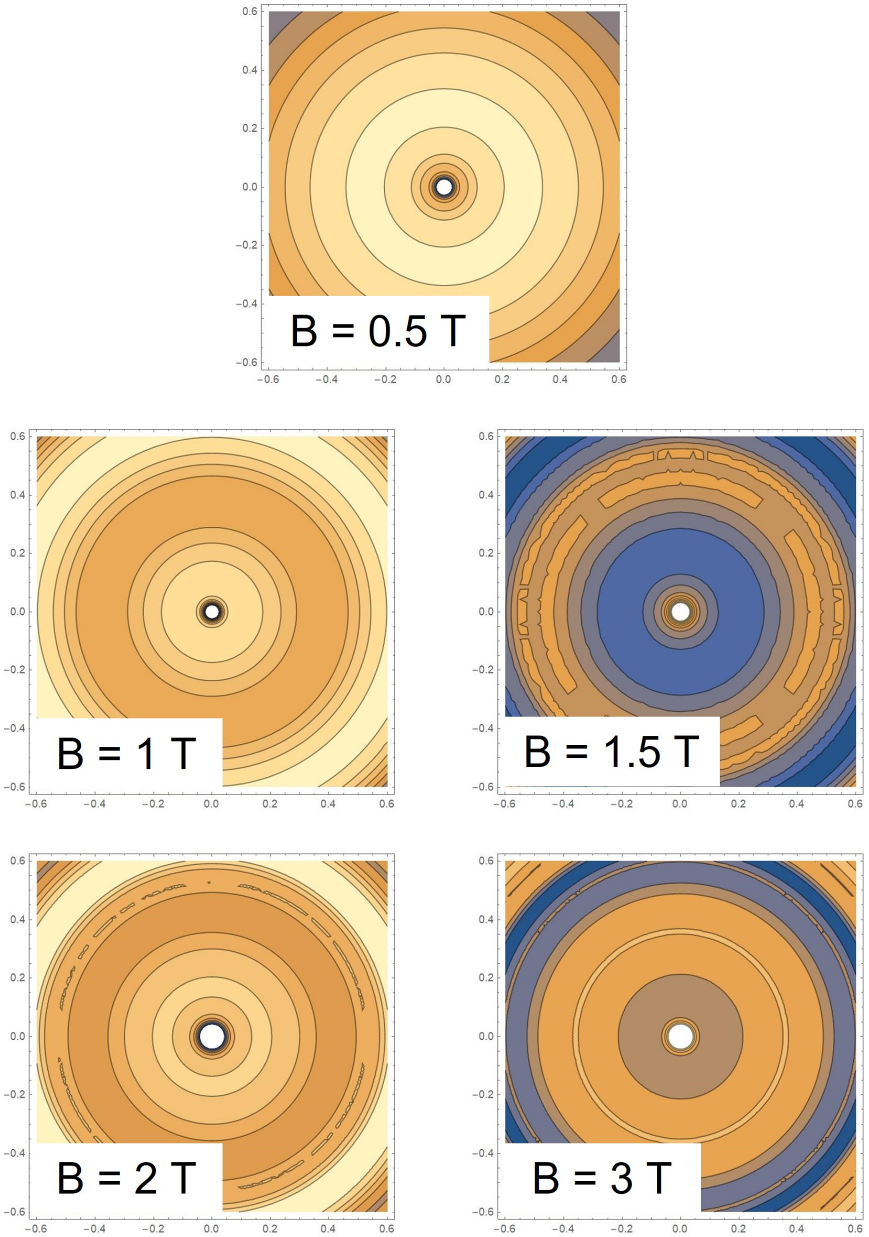

Figure 1.11: Numerical model for an MDPX Type 1 filament for various magnetic field strengths at a pressure, p = 30 mTorr.

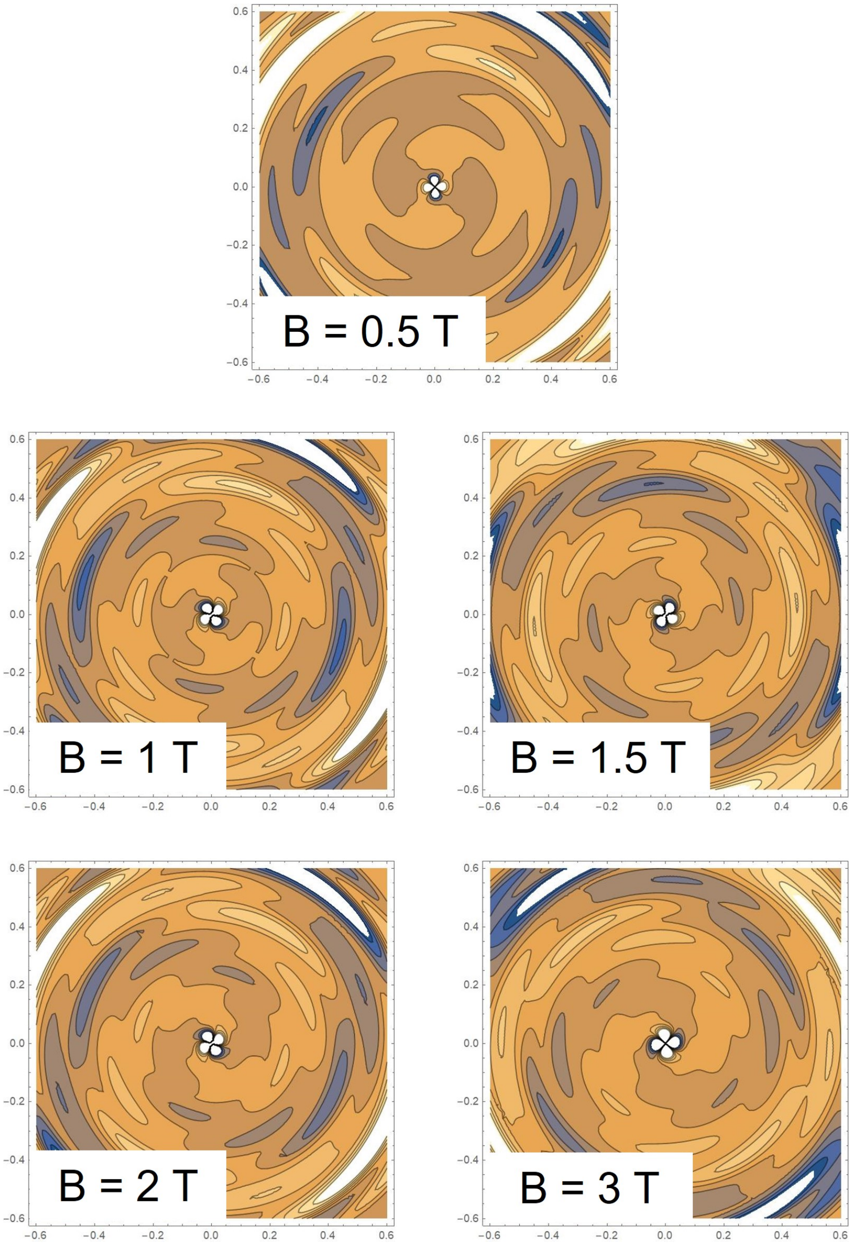

Figure 1.12: Numerical model for an MDPX Type 2 filament for various magnetic field strengths at a pressure, p = 30 mTorr.

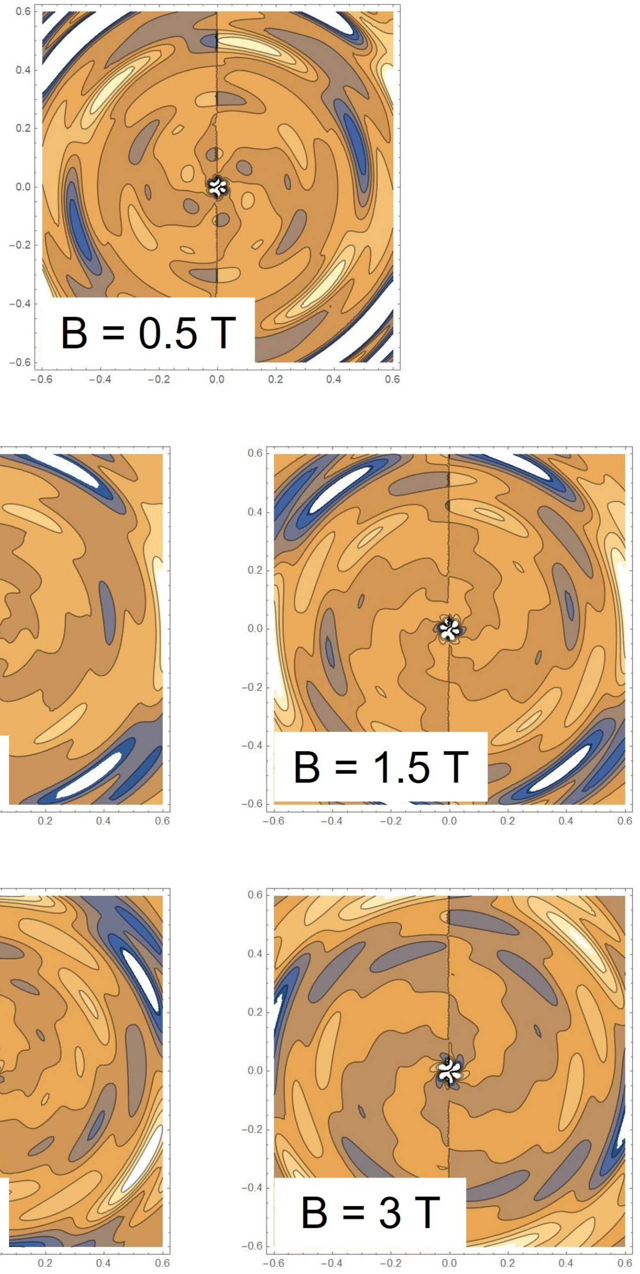

Figure 1.13: Numerical model for an MDPX Type 3 filament for various magnetic field strengths at a pressure, p = 40 mTorr.

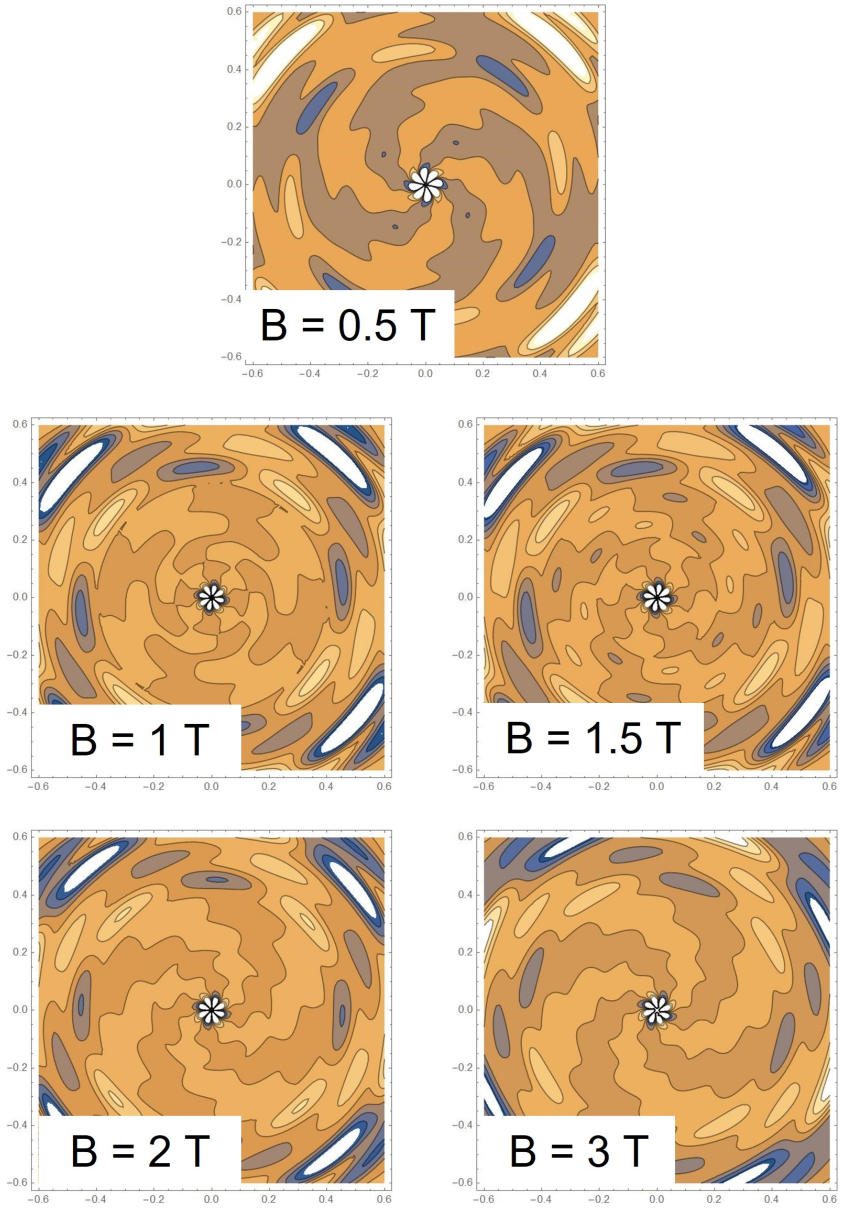

Figure 1.14: Numerical model for an MDPX Type 4 filament for various magnetic field strengths at a pressure, p = 40 mTorr.

Interestingly, and expectantly, all four modes give nonsensical results for the $B = 0$ case. The Type 1 gives a completely imaginary solution, while the Type 2 gives a very large unstable solution, and Type 3 and 4 both give uninterpretable results. As magnetic field increases to $B = 0.5$ T, the Type 1 and Type 4 solution becomes stable while the Type 2 solution starts to develop into a more stable result, and the Type 3 solution remains unstable. Although the Type 1 and 4 solutions give real and stable results, observations in the experiment only show the Type 1 solutions at $B = 0.5$ T. Therefore, it may be that solutions exist for different modes at the same magnetization, but are not energetically able to be reached. At $B = 1$ T, the Type 1, 2, and 4 solutions are all stable with the Type 3 solution remaining unstable. Experiments show Type 1 and 2 filaments can exist at 1 T, with the Type 1 filaments dominant. Increasing the magnetic field further to 1.5 T, the Type 1, 2, and 4 solutions remain stable, and the Type 3 begins to show some convergence to a stable solution. Again, the experiment confirms the existence of circular and elongated (Type 1 and 2 respectively) filaments at this magnetization, while Type 3 and 4 are not observed although their solutions seem to exist as well. For $B = 2$ and 3 T, we see Type 1 filament solutions as being real for the 2 T case but not for the 3 T (the solution is only imaginary). This is confirmed through experiments with the number density of Type 1 filaments essentially zero for 4 Pa (30 mTorr) when the magnetic field is above 2.5 T. As for Type 2, 3, and 4 filaments, those solutions seem to exist as real solutions for both 2 and 3 T. Experimental observations also support this result as elongated filaments seem to begin between 1 and 1.5 T and persist at higher fields with spirals (Type 3 and 4) emerging at fields around 2 T or higher.

The results of the Mathematica code are somewhat promising in that they predict some of the filament behavior seen in the MDPX experiments. Particularly the different modal patterns formed at certain magnetic fields. This suggests that the drift wave instability may be responsible for driving the filament patterns observed in the experiments. Of course there is more theory groundwork that needs to be done to give a more complete picture of the filamentation phenomenon. However, the code provides a potentially useful direction for a place to begin to develop a theoretical framework.

In the next chapters, we will present the experiments performed and the following data analysis. Chapter 2 will discuss the MDPX device, the experiment hardware setup, and the software used to collect the image data. Next, chapter 3 will cover the experiment procedures and observations for the different set of experiments performed as well as the pre-processing steps taken before the analysis. In chapter 4, we will present the analysis of the data and the results obtained. Finally, we will conclude this work with final thoughts and the broad avenues for the future of filamentation work.

Chapter 2

Experiment Hardware

2.1 Magnet

All experiments described were performed on the Magnetized Dusty Plasma Experiment (MDPX) device, which is a 4 T class split bore, superconducting magnet. The MDPX device is composed of two primary components, a large cryostat that houses the four Nb:Ti (Niobium-Titanium) superconducting magnetic field coils and the vacuum chamber where plasma experiments are performed. The cryostat has a cylindrical shape with an overall outer diameter of 122 cm and an axial length of 157 cm. In order to maintain a superconducting state, the coils must be cooled and held at very low base temperatures of 4.5 - 5 Kelvin. The cryostat features an open, 50 cm diameter, 157 cm long cylindrical ”warm bore” that gives users the ability to access equipment placed within the split-bore. This allows users to utilize diagnostic components or manipulate experimental conditions without removing any secured equipment. The predominant advantage of the magnet configuration is the unique ability to ”ramp” the magnetic field from anywhere between 0 T to up to 4 T in strength. Another key advantage of the MDPX system is that the use of type II superconductors with Nb:Ti strands within copper exhibit the ability to reach high magnetic fields below its critical temperature ($T_c = 6.4$ K) while maintaining efficient performance even in a mixed Normal/Meissner state [35, 36]. More importantly, the coil system can be operated using cryocompressors instead of liquid helium enabling cost effective and highly reliable magnetic field operations.

Magnetic strengths between 0.5 T and 3.5 T were used for the filamentary experiments. The currents introduced into the system to achieve these field strengths range from 16 to 110 Amps (A). Due to the geometry of the cryostat and coils, the magnetic field direction within the bore is uniform vertically, with a downward orientation (north to south). This ensures that any equipment placed in the bore for experimentation will be exposed to a uniform field direction. Furthermore the magnet can be rotated from verticle through four angles (at 15° increments) through 90° horizontally. The magnetic field direction aligns with the coils, thus the angle of field direction follows the orientation of the magnet with respect to the vertical. An image of the MDPX device and schematic of the experimental configuration can be seen in figure 2.1.

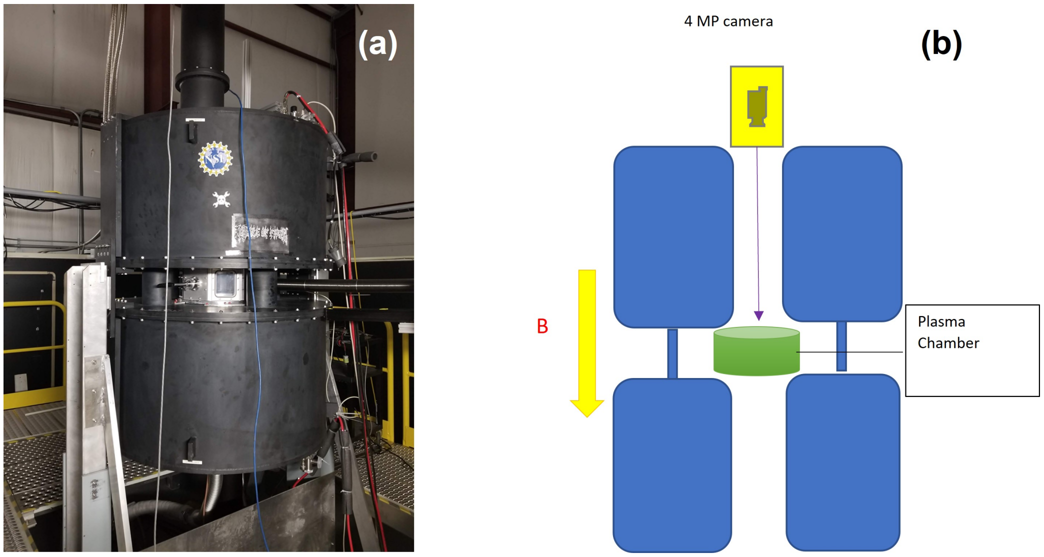

Figure 2.1: Images of the Magnetized Dusty Plasma Experiment (MPDX) system. (a) View of the MPDX system showing the cryostat (painted black) that houses the four superconducting coils and the integrated vacuum chamber. (b) A schematic drawing that shows the overall experimental configuration and magnetic field orientation.

2.2 Vacuum Chamber

The vacuum chamber used for these experiments was the standard octagonal aluminum chamber used for previously reported MDPX experiments [14, 22, 23, 30]. Figure 2.2 shows the vaccum chamber and a schematic detailing the setup of the experimental conditions in the chamber. It has a height of 17.78 cm, an inner diameter of 35.56 cm, and outer diameter of 45.7 cm. Each chamber side has adaptable thru ports measuring 12.7 cm (5 in) in height and 10.16 cm (4 in) in width. The top and bottom flanges of the chamber each have a 15.24 cm (6 in) diameter thru port for viewing/vacuum components. The top and bottom flanges also have several ports for diagnostic equipment including a gas inlet.

There are two electrodes, each with a diameter of 27.9 cm (11 in), within the chamber that are isolated from ground and can be either powered with an RF generator, left floating, or connected to ground. It should be noted that the top cover and top electrode both feature circular cutouts that allows for viewing from above. The top electrode, in particular, has a 14.6 cm (5.75 in) diameter centered hole.

For the experiments described in this dissertation, the vacuum chamber was configured such that the inter-electrode spacing was set to 5.7 cm with the lower electrode powered and the top electrode allowed to float. A 10 cm by 10 cm by 0.3 cm glass plate with one side coated with Fluorine-doped Tin Oxide (FTO) is placed, conducting side down, in the designated cut-out in the top electrode. This allows uniformity in the potential profile created from the electrodes while maintaining visibility into the plasma created from above. A second 10 cm x 10 cm x 0.3 cm FTO glass plate is placed within the 15.24 cm diameter, 3.1 mm deep depression of the bottom electrode with the FTO coated side facing downward, toward the electrode. While the uncoated side (i.e., the insulated side) faces upward toward the plasma and top electrode. The purpose for a second glass plate is to allow charge accumulation to help the formation of the filament columns as described in the paper by Menati, et al [27]. Eight Plexiglas windows were placed on the sides which allowed optical access to the plasma from any angle. Two MKS baratron pressure transducers were fitted on the top of the chamber in order to accurately determine the neutral pressure within the chamber. A gas inlet was also placed on the top of the chamber for neutral gas input. A high-power Rf adapter is placed on the bottom of the chamber to power the lower electrode. An Edwards nEXT240D 160 W turbopump is connected in line to the bottom 15.24 cm thru port with a KF-63 adapter.

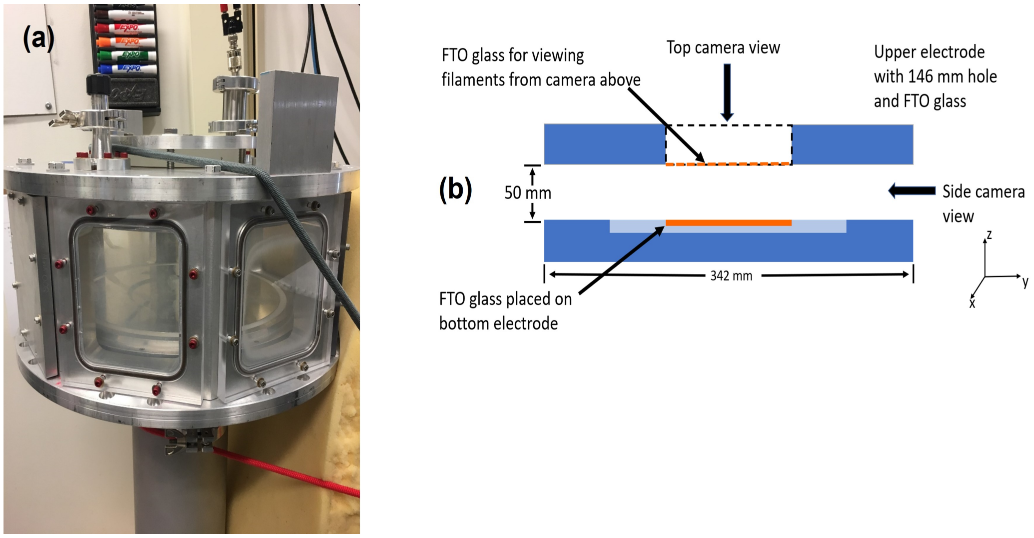

Figure 2.2: (a) Closeup view of the vacuum chamber. For the experiments reported here, the vacuum chamber uses a capacitively coupled plasma (CCP) configuration using an electrically floating upper electrode and powered lower electrode. (b) A schematic drawing showing the MDPX octagonal vacuum chamber electrode configuration.

2.3 Gas System

The gas system utilized through each experiment was installed to flow all neutral gases using the same systematic method. The gas for the different plasma experiments are injected into the chamber through the top cover and are pumped out through the turbopump connected to the bottom cover. The inlet system is maintained by an MKS 1179A12CS18V 100 sccm Mass

Flow Controller (MFC). Depending on which gas is being flowed, the chamber neutral pressure can range from ∼4 mTorr (0.1 Pa) to ∼50 mTorr (6.6 Pa). Furthermore, to increase gas input beyond the limits of the MFC, an Edwards LV10K needle valve bypass was installed in line. The chamber pressure is monitored throughout the experiments with two baratron pressure transducers. A full scale 1 Torr model 722B baratron was used to monitor pressures above 100 mTorr accurately while a full scale 0.1 Torr model 627H baratron was used to monitor pressures accurately between 1 and 100 mTorr.

2.4 Plasma Generation and Camera

The plasma gerenated throughout all experiemnts were capacitively coupled radio frequency (RF) plasmas created with the 13.56 MHz fixed frequency, RF generator. Once the plasma is generated, it is maintained within the inter-electrode gap of the vacuum chamber. The power deposited into the chamber for plasma generation is controlled by T&C AIT-600-03 HNAU3 RF Power Source and tuning of the T&C AG 0313 auto-matching network. The rf generator is rated to provide input power up to 100W, however most experiments were performed at very low power of ∼1 W. To further control the power input levels, the auto-tuning matching network was operated in its ”manual mode” such that the user can manually control the load and tune capacitor positions thereby achieving fine tuned control over the input power.

In order to study the formation of filaments and their associated spatial structures, the experiment setup was configured to allow direct observation of the filaments through the top port of the MDPX vacuum chamber. This is accomplished by using a Ximea 4MP xiQ series model MQ042MG-CM camera to image the filaments created. The camera is a 4 mega pixel, 16-bit, grayscale camera with a 2048 x 2048 full-scale cmos array with a full-resolution frame rate of 90 frames per second (i.e. 90 fps). The camera was placed on a housing which fits on the top of the magnet and gives the ability to view the chamber from above through the bore of the magnet as can be seen in figure 2.3. A 200 mm Nikon macro lens was placed on the camera and focused to view the filaments for the various experiments performed. The Ximea camera was operated using the XIMEA CamTool software that is provided with the camera hardware. The software configuration includes options to adjust for region of interest (ROI), exposure, gain, bit-depth, frame rate, and bandwidth.

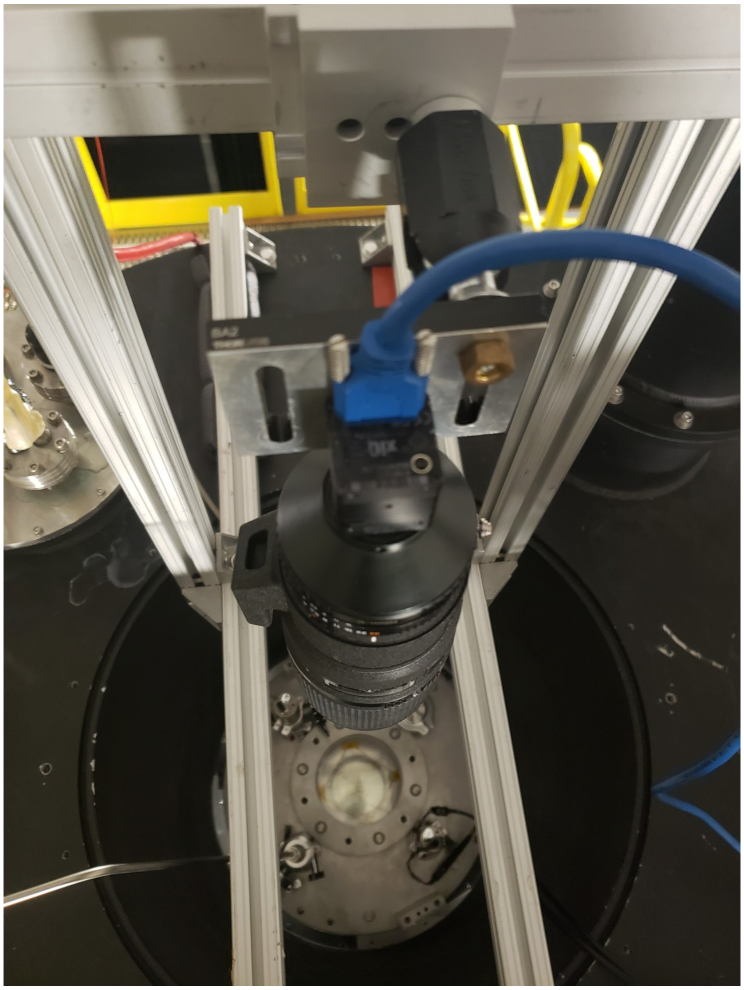

Figure 2.3: Ximea 4MP xiQ series camera with a 200 mm Nikkon lense attached to an 80-20 stainless steel structure mounted on the top of the MDPX device, allowing optical view of the chamber from above.

Chapter 3

Observations and Image Preprocessing

This chapter will focus on the qualitative analysis by introducing the experimental observations and data preparation processes. Chapter 4 will incoporate a more detailed quantitative analysis of the data collected.

As shown in figure 3.1(a), in the absence of a magnetic field, plasmas in the MDPX device are visually uniform and fill the plasma volume between the electrodes. While plasma operations in MDPX at high magnetic fields ($B \geq 0.5$ T) can have stable plasma operations, under certain low RF power ($RF \leq 10$ W) and low neutral pressure ($p \leq 10$ Pa) operating conditions, filaments can appear. Filaments appear in the chamber from a side view as bright vertical columns along the direction of the magnetic field with dark gaps between individual filaments, as shown in figure 3.1(b). Similarly from above, filaments appear as bright spots in a background of a ”uniform” plasma (see figure 1.2(a)). The filament phenomena that are studied in this work are very long-lived structures ($\Delta t >>$ minutes) that persist as long as appropriate conditions within the plasma are met. Moreover, the filament observations and dependencies on operating conditions of MDPX are generally consistent with the observations in the original, foundational studies performed at the Max Planck Institute and reported by M. Schwabe et al. [17]

As a reminder, these experiments on the MDPX device were performed with several goals in mind. First, as discussed in Ch. 1, the ultimate mission of the MDPX device is to perform studies of dusty plasmas at high magnetic fields and the presence of the filaments disrupts the stability of the plasma. Therefore, it is critical to establish the conditions under which filaments form. Second, as the studies of the filaments have continued, they are a unique and scientifically interesting phenomenon in a bounded, highly magnetized, low temperature plasma and study of the filaments is intrinsically valuable to gain an understanding of the physics of a magnetized plasma. This dissertation will report on several different studies of filamentary behavior in the MDPX device in which the magnetic field, pressure, and gas species will be the critical experimental parameters that will be varied from one experiment to another.

The experimental studies begin with the study of argon plasmas in the MDPX device. Argon is the same working gas used in the Max Planck studies

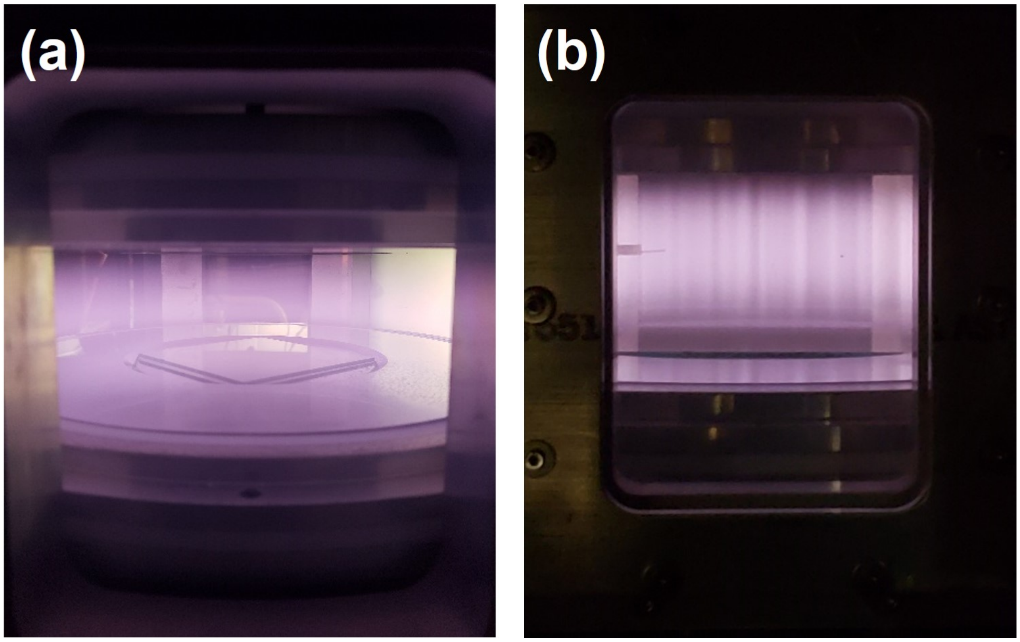

Figure 3.1: (a) Argon glow discharge plasma with no magnetic field present. An FTO glass plate that is placed on the bottom electrode is visible in this image. (b) Argon plasma glow discharge with high magnetic field present. Filaments can be observed in the interelectrode gap (5 cm) between the upper and lower electrodes. A single tip Langmuir probe can be seen in this image (inserted into from the left).

and provides an important reference that can be used to compare against the studies reported in this work. The MDPX argon filament experiment was performed as a two-fold exercise. The first features a scan through multiple pressures at selected magnetic field strengths. The second is a scan over magnetic field while keeping power input and pressure consistent. Section 3.1.1 will discuss the observations while varying pressure, and show how the filament morphology responds to those changes in neutral gas pressure. Section 3.1.2 and 3.1.3 will discuss the observations of filament morphology through the magnetic field discharge scan.

3.1 Filament Observations in Argon Plasmas

Several of the observations and analysis of the argon filaments were reported in Williams et al. (2022) [30] and are incorporated into this document.

3.1.1 Pressure Scan

Filaments begin to appear within the plasma with an applied magnetic field strength of approximately 0.5 T at low neutral pressure and low applied RF power combinations. For observations described in this section, the power input was fixed at 1 W and the pressure was varied over a range of p = 3.4 to 6.6 Pascal (Pa) while the filament response to the changes in pressure over this range was recorded. This same pressure range in alternate units is approximately 25 to 50 mTorr. As stated in chapter 2, the top electrode was allowed to float while the bottom electrode was powered. It should be noted that filaments appear under operations where the top electrode is either floating or grounded.

As seen in figure 3.2(a) the elongated filament columns are clearly visible from the side. However, when viewed from above, the filaments are observed to take on three distinct shapes on the terminating end of the column (figure 3.2(b)). The three ”types” of filaments can be indentified as seen in figures 3.2(c-e): Type 1:circular, Type 2: elongated, and Type 3: 3-arm spiral. It is shown in figure 3.2(b) that at certain chamber conditions, all three shapes can co-exist in the system.

A scan of pressure was conducted with an applied magnetic field of 2 T and a power input of 1 W illustrated in figure 3.3. Observations reported here at 2 T were also obtained at $B > 2$ T (2.5, 2.75, 3 T, etc.). At the lower pressure range, filaments are observed to begin to coalesce into the individual structures. As the neutral pressure increases, the individual filament structures become more distinct in brightness and shape. At 3.45 Pa ($\sim$25 mTorr), all three filament types are present within the system and remain relatively stable. As the pressure continues to increase only type 1 filaments were observed to exist in the system. Furthermore, it was observed that as the pressure reached $\sim$5 Pa ($\sim$37 mTorr) the number of filament columns began to decrease, the occupied area in the plasma where filaments are created also began to reduce above this threshold, and average filament brightness increase in intensity. At pressures $p \geq 6$ Pa, the number of dis-

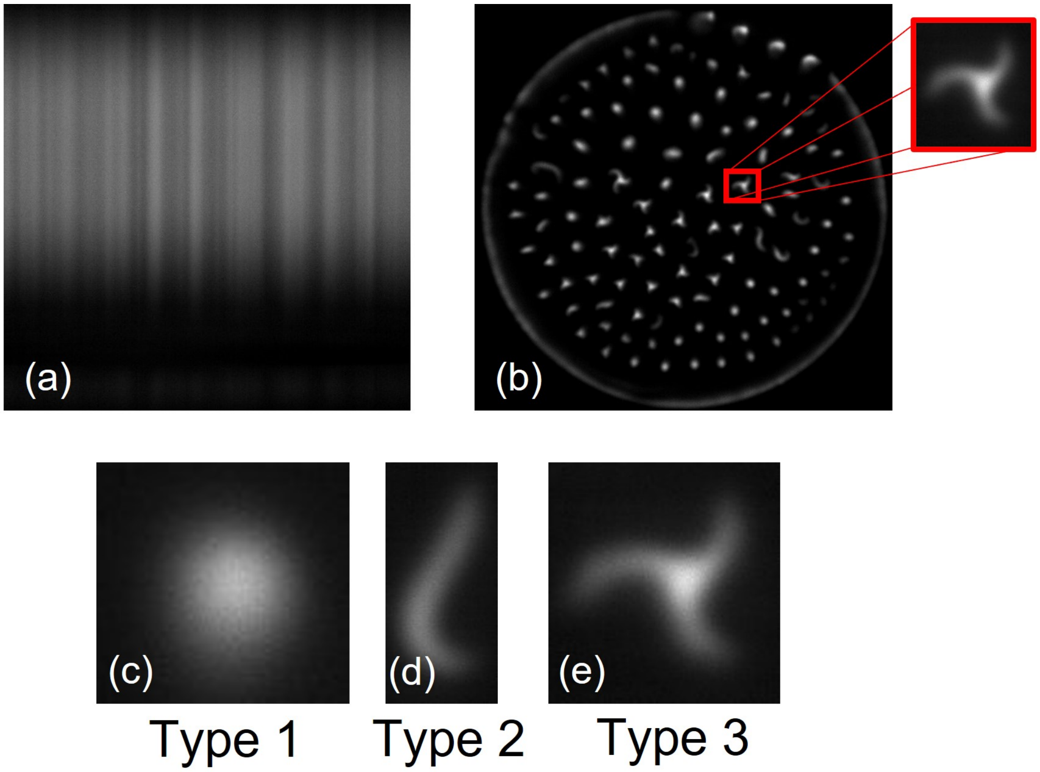

Figure 3.2: Observations of plasma filaments in an argon plasma from (a) side and (b) above for the same operating parameters in MDPX: B = 2 T, p = 3.5 Pa, P_{RF} = 1 W. The insert in Fig. 3(b) shows a closeup of one of the spiral type filament morphologies. Over a range of experimental conditions, three distinct and reproducible filament "types" are identified: (c) Type 1 – circular, (d) Type 2 – Elongated, and (e) Type 3 – Spiral.

crete filaments continues to decrease to where no filaments are visible within the plasma above $p = 6.6$ Pa. These observations illustrate filament creation and structure have a clear dependence on neutral pressure within the system. It should be noted, that although other morphologies may be present, e.g.

as in figure 3.3(c), the focus of the analysis is conducted on the most stable, robust, and repeatable filament structures that appear within the plasma.

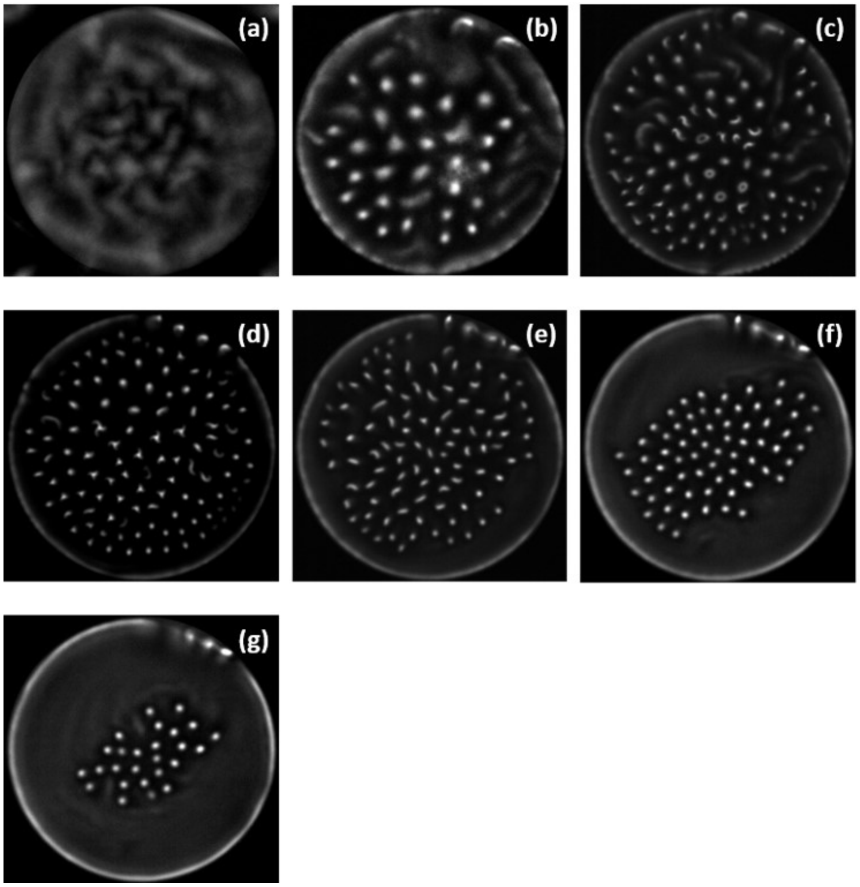

Figure 3.3: Images of filaments from above with increasing pressure for a constant operating magnetic field of $\mathbf{B = 2}$ T and applied RF power of $\mathbf{P_RF = 1}$ W. Filaments begin to become distinct around 1.60 Pa (12 mTorr) and fill the volume of the observable area, peaking between 3.40-4.45 Pa (25-35 mTorr) with scale length reduction and clear boundaries. As pressure increases further, there is a reduction in the number of filaments which occupy the observable area. Additionally, with high pressure (around 5.3 Pa), type 1 filaments highly dominate the population. (a) 0.665 Pa (5 mTorr), (b) 1.60 Pa (12 mTorr), (c) 2.66 Pa (20 mTorr), (d) 3.45 Pa (26 mTorr), (e) 4.40 Pa (33 mTorr), (f) 5.32 Pa (40 mTorr), (g) 6.0 Pa (45 mTorr).

3.1.2 Magnetic Field Scan in Argon Plasma

With the second set of filament parameter space scan experiments, we consider the variation of filaments with respect to the applied magnetic field strength. It was demonstrated in earlier experiments that a magnetic field is required for filament formation and strongly depends on the strength of the field. For this study, an argon plasma is formed in the vacuum chamber at constant RF power and pressure. The superconducting coils in the magnet are charged such that fields of $B \geq 3$ T are achieved. Subsequently the current in the coils is allowed to discharge at a fixed rate which allows for a controlled magnetic field decrease over a period of ~2 hours. The magnetic discharge experiment procedure is as follows:

1. The magnetic field is set to a high value 3 to 3.5 T with a fixed RF power, pressure, and gas species.
2. At t = 0, the current in the magnetic field coils is then allowed to discharge, allowing the magnetic field to begin to fall. The magnetic field measurements are recorded by the MDPX data acquisition system at a rate of 10 Hz.
3. Simultaneously, the video camera begins recording single frame images of the plasma at a rate of 1 Hz (1 frame per second)

In a typical single run, approximately 2 to 3 hours is required for the magnet to slow discharge from 3 T to 0.5 T (i.e., $\Delta B/\Delta t$ (max) $\sim$ 1 T/hour $\sim$

2.8×10^{-4} T/s), so that the experiment is effectively in a quasi-equilibrium state at each video image. This process is shown in figure 3.4 in which pressure is maintained at $p = 3.45$ Pa (26 mTorr), input power of $P_{RF} = 1$ W, and the magnetic discharge that began at $B = 3.5$ T.

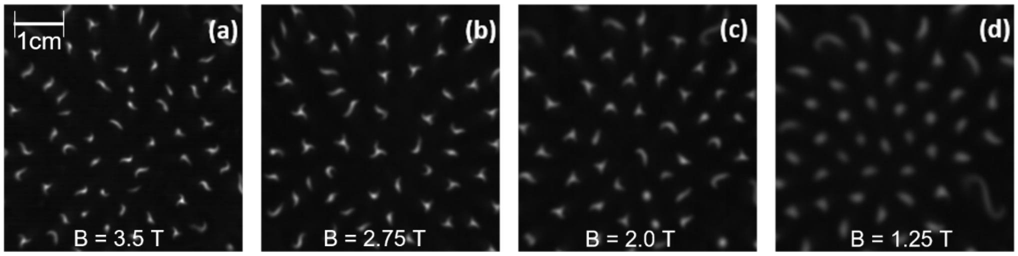

Figure 3.4: Observations of plasma filaments as the magnetic field is decreased. Both power input and pressure remain constant during discharge (1 W and 3.45 Pa respectively). At high magnetic field strength, filaments maintain relatively high light intensity, distinct boundaries, smaller area, and all three filament types are present. As field decreases, light intensity decreases, individual filament area increases, boundaries become less distinct, and some filament types are unobserved. At low field (1 T or less), only type 1 filaments are observed while their area increases over two times their area at high field (above 2.5 T). (a) 3.5 T, (b) 2.75 T, (c) 2.0 T, (d) 1.25 T.

Much like the pressure scan experiment, multiple filamentary mode structures were observed. As seen in figure 3.4(a) at $B = 3.5$ T, the dominant structures present in the system are Type 2 (elongated) and Type 3 (spiral) whereas the Type 1 (circular) filaments are virtually absent. As field decreases to $B = 2.75$ T (illustrated in figure 3.4(b)), filaments appear larger, spiral arms appear larger and more defined in comparison to the $B = 3.5$ T case, and the system remains dominated by spiral and elongated structures. With the magnetic field decreasing further to $B = 2$ T, the number of Type 1 filaments increase as does the general size of all the Type structures. Additionally, the filaments are considerably less bright than at 3.5 T. Lastly, as the magnetic field decreases to $B = 1.25$ T, Type 3 filaments have vanished and only Type 1 and 2 filaments remain in the system. While dominated by mostly Type 1 filaments, the brightness of the filaments continue to reduce in intensity, the filament boundaries are much less distinct, and the effective size of the filaments are larger than in the 3.5 T case. The measurements shown in figure 3.4 were repeated with for neutral pressures of $p = 4.4$, 5.3, and 6 Pa (33, 40, and 45 mTorr respectively) in which all trials yielded very similar results.

3.2 Filament Observations Using Different Gas Species

As in the first experiment outlined above with only argon plasma, the same two-fold experiment was performed in helium, neon, and krypton plasmas. One purpose of using different gas species was to investigate if filament formation and morphology was a phenomena common to other plasma gas species types. Filaments observed in gases other than argon would provide strong evidence that the phenomena is driven by a general magnetization property of the plasma. This is also a novel experiment as the filament structures have not been reported as observed in plasmas made from other gas species. The second purpose of this study is to scan through a larger range of the Hall parameter space. Since the magnetization of the ions is described by the Hall parameter, which is a function of the magnetic field to neutral pressure ratio as well as ion mass, introducing a difference in mass (i.e. different gases) provides the ability to possibly explore a greater span of the Hall parameter regime. This will be discussed in more extensively in the beginning of chapter 4.

As stated above, both pressure and magnetic field scan measurements were taken with the different plasmas. Although the pressure scan provided some information on the filament structure, the magnetic field discharge gave more insight into the morphology evolution of the filaments. Therefore, the focus of the observation and analysis that follows will be on the magnetic field scan results.

It is shown in figure 3.5 filaments are observed to exist in plasmas generated in all four gas species that have been tested. As seen in figure 3.5(a) helium filaments formed are not as distinct in morphology as previously seen in argon or other plasmas. These filaments are also similar to the less stable filaments found in argon depicted in figure 3.4(c). Figure 3.5(b) shows neon in which Type 1, 2, and 3 filaments co-existing in the same system much like argon as shown in figure 3.2(b). Lastly krypton filaments in figure 3.5(c) show distinct filament structure with Type 2 and 3 filaments as dominant

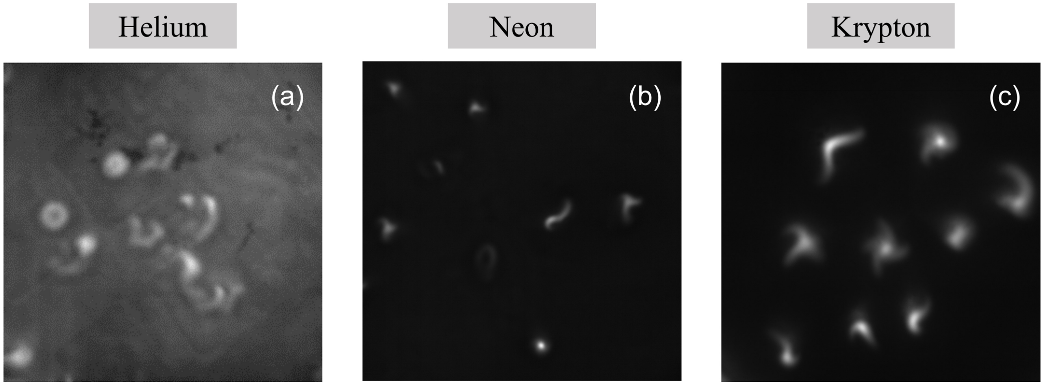

Figure 3.5: Three separate experiments in which filaments are shown to exist in MDPX plasmas of different neutral gas types. (a) Filaments in a helium plasma at $\mathbf{B = 0.65}$ T and pressure $\mathbf{p = 2.66}$ Pa (20 mTorr). (b) Filaments in a neon plasma at $\mathbf{B = 1}$ T and pressure $\mathbf{p = 4}$ Pa (30 mTorr). (c) Filaments in a krypton plasma at $\mathbf{B = 2.2}$ T and pressure $\mathbf{p = 6}$ Pa (45 mTorr).

in the system. The krypton experiments also revealed a new ”type” of filament appropriately categorized as a Type 4: 4-arm spiral filament. This new structure type typically features a bright center with four spiral arms curving radially outward. This type of filament appears to be an experimental validation of a four-arm filament orginally observed in the simulation results by Menati et al. [28]

Very similar patterns of filament evolution are observed in each of the other gases as observed in the argon experiment. As the neutral gas pressure increases, filaments begin to coalesce into individual columns. Increasing pressure further gives more stable conditions for filaments resulting in the existence of different types of long-lived filaments. Finally, further increasing pressure leads to stable Type 1 filaments that then decrease in number until none are visible in the plasma. Additionally, as in the argon magnetic field scans, the filament morphology is strongly dependent on the strength of the field applied as seen in figures 3.6 - 3.8. The table shown in figure 3.9 summarizes the information presented below.

In the context of this dissertation, a formal definition of filament stability should be introduced. A filament can be considered stable if it takes a distinct shape, such as a circle or multi-arm spiral, for a time of 2 seconds or more. This is time frame is chosen because the experiments are performed with images taken every second; therefore, if a filament is seen in one image, it should be confirmed to retain that shape in the following image. If the general system of filaments does not exhibit distinct shapes for the stated time frame, and individual filaments quickly move from one morphology to another while coalescing into stream-like patterns, the system is then said to be turbulent.

Figure 3.6 shows that filaments were obtained in helium with a constant input RF power of 1 W different pressure ranges between 1.33 and 2.66 Pa (10 and 20 mTorr respectively). The example illustrated was taken at various magnetic fields at a pressure $p = 2.66$ Pa. The evolution of the filament shape is demonstrated in the figure, however there are differences in helium when compared to other plasmas.

At low field, $B = 0.25$ T figure 3.6(a), the filament shape is mostly Type 1 with striated structures in areas of the system. Figure 3.6(b) exhibits interesting behavior unseen in other plasmas. Type 2 and 3 filaments are

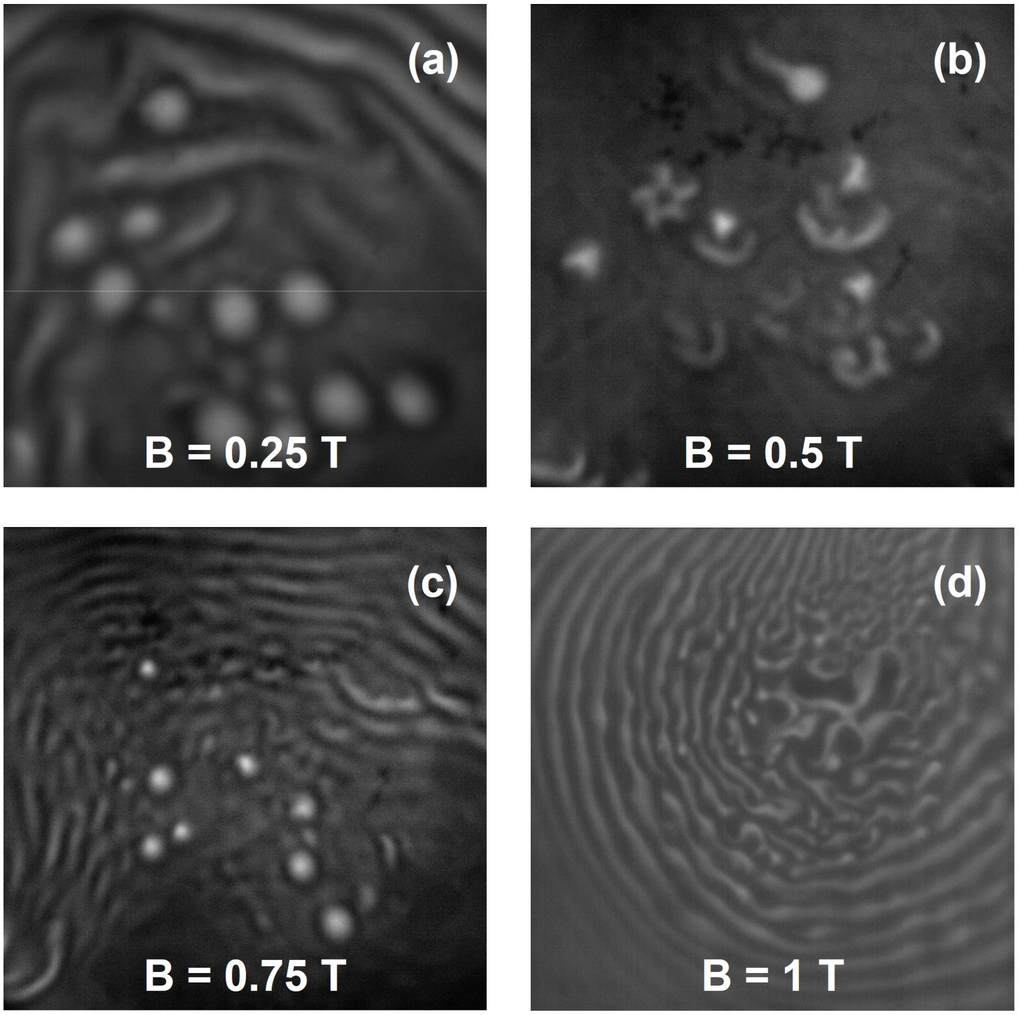

Figure 3.6: Shows the existence of filaments in a helium plasma in the MDPX device with pressures between 1.33 and 2.66 Pa at 1 W for various magnetic field strengths. Image (b) shows interesting star-like pointed structures that have only been observed in helium.

observed in the plasma in addition to a five-pointed filament with a dark center. Figure 3.6(c) shows Type 1 and 3 filaments in the plasma with smaller effective areas with striated filaments found to occupy a larger area of the system and are thinner in width. Finally, figure 3.6(d) illustrates there are no stable filament columns present in the system. Moreover the figure shows the turbulent behavior of filamentation subject to a higher magnetic field.

Filaments in a helium plasma are much less stable than in other plasmas tested. Finally, it is noted that filaments in a helium plasma are much less stable than observed in other gas species. Here, stability refers to the lifetime of individual filaments observed in the plasma. Compared to the observations in neon and argon, where individual filaments may persist in the plasmas for many 10's of seconds, for helium, this time may be as little as 1 second or less.

Figure 3.7 exhibits the evolution of filament geometry in a neon plasma at different magnetic field strengths with an input power of 1 W and at a pressure $p = 3.32$ Pa (25 mTorr). Figure 3.7(a) illustrates at lower field, $B = 0.5$ T, Type 1 and 2 filaments are observed in neon while figure 3.7(b) shows Type 2 and 3 filaments at $B = 1$ T. These filaments tend to dominate the system at this magnetic field and feature more distinct boundaries than in the $B = 0.5$ T case. All three filament types are found to coexist in figure 3.7(c) with distinct boundaries and Type 1 filaments seeming to have higher light intensity than the other types. At magnetic fields above $B \sim 1.5$ T,

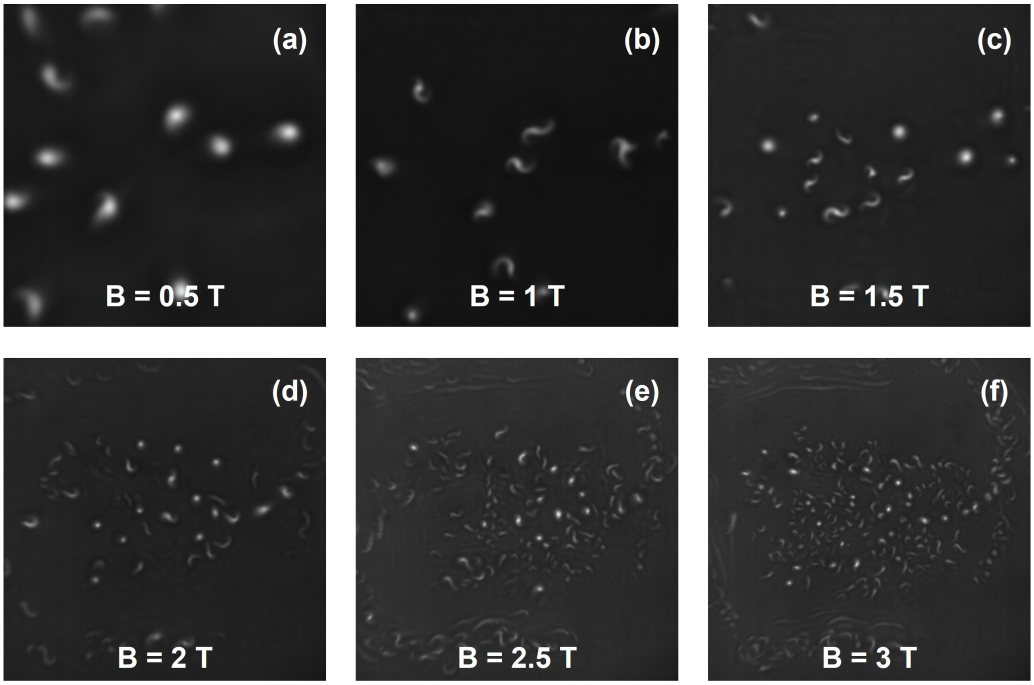

Figure 3.7: Filaments are presented as a function of magnetic field in a neon plasma with pressure, p, and power, P_{RF}, constant (3.3 Pa and 1 W respectively). Filament evolution can be seen as magnetic field increases. Type 1, 2, and 3 filaments are observed in the plasma similarly to argon. At relatively low fields, B $\sim$ 0.5 T, the plasma self-organizes such that mostly Type 1 filaments are observed with a few additional Type 2 filaments. As magnetic field increases with, 1 T $\leq$ B $<$ 2 T, Type 2 and 3 filaments appear and populate the system while Type 1 filaments seem to remain at a reduced number, but do not vanish as much as in argon or krypton. Above B $\geq$ 2 T, the neon filaments appear to transition into a turbulent regime.

neon filament behavior begins to transition into a more turbulent regime as can be seen in figures(d)-(f). The filaments become more striated and any shape taken does not exist in its state for a long time period. Typically filaments exist in a stable shape for a few seconds. However, when exhibiting turbulent behavior, the time frame that filaments take a stable shape is much less; typically less than a second. As previously stated, the focus of this discussion will be on the stable filament regime.

Similarly to the figures above, figure 3.8 shows the evolution of filaments in a krypton plasma. Filaments begin forming in the plasma above $B = 1$ T. The first filaments observed in krypton are Type 1 circular filaments just as in other plasmas tested. Figure 3.8(a) illustrates this trend with $B = 1.5$ T. Type 2 filaments are seen on the outer edges of the image, but the system is dominated by the Type 1. Increasing to 2 T in figure 3.8(b), the morphology primarly takes the Type 2 shape with a few filaments appearing to reach the edge of the transition state to Type 3 filaments. Figures 3.8(c)-(d) are similar in that approximately the same amount of Type 2 and 3 filaments are found to occupy the system while figure 3.8(e) shows Type 3 filaments dominating the system at $B = 3$ T. In addition, the shape progression agrees with the similar observations found in argon and neon plasmas such that the initial filaments observed are effectively larger in area, less bright on average, and exhibit less distinct boundaries. As magnetic field increases to 3 T, the observed filament area decreases, intensity may increase, and the boundaries become much more distinct.

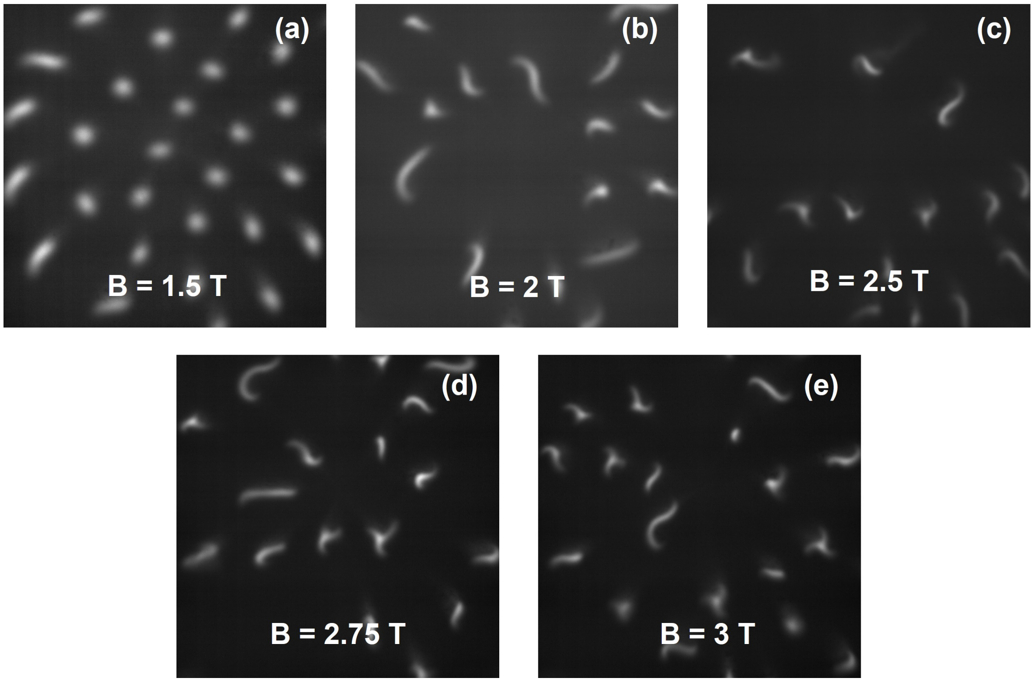

Figure 3.8: Filaments are presented as a function of magnetic field in a krypton plasma with pressure, $\boldsymbol{p}$, and power, $\mathbf{P_{RF}}$ constant (5.3 Pa and 2 W respectively). The evolution of the krypton filaments can be seen as magnetic field increases. Similarly to argon and neon, the filament system begins with a Type 1 dominant configuration and few Type 2 filaments with Type 3 and 4 unobserved. As field increases, Type 2 filaments become the dominant shape with some Type 3 shapes entering the system while Type 1 filaments reduce in number. At very high fields, i.e. $\boldsymbol{B > 2.5}$ T, essentially only Type 2 and 3 filaments are observed to occupy the system. Lastly, similar features in brightness and effective area is seen in krypton as in the other plasmas.

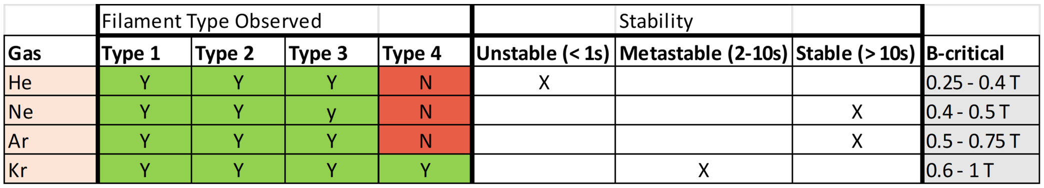

	Filament Type Observed				Stability			
Gas	**Type 1**	**Type 2**	**Type 3**	**Type 4**	**Unstable (< 1s)**	**Metastable (2-10s)**	**Stable (> 10s)**	**B-critical**
He	Y	Y	Y	N	X			0.25 - 0.4 T
Ne	Y	Y	y	N			X	0.4 - 0.5 T
Ar	Y	Y	Y	N			X	0.5 - 0.75 T
Kr	Y	Y	Y	Y		X		0.6 - 1 T

Figure 3.9: A tabular summary of the types of filaments observed in each gas species, their relative stability when formed, and the critical magnetic field range needed to begin filament formation in the respective gas species. All gas species tested, aside from helium, produce filament structures that last a few seconds at minimum. Argon and neon produce the most stable observable filaments.

3.3 ImageJ (FIJI) and Image Processing

Because these studies seek to classify the filament morphologies in a systematic fashion, it is essential to develop techniques to classify the shape of the filaments observed (i.e. Type 1, 2, 3, or 4) and degree of filamentation (i.e. the area in pixels occupied by filaments). The software used to pre-process the raw data imported was the open source Java image processing program *FIJI* [37]. *FIJI* (an acronym which stands for 'Fiji Is Just ImageJ') is an improved ImageJ package that provides the user with additional macros and plug-ins that ImageJ does not posses. The *FIJI* software is extremely popular in the life sciences due to its ability to allow the user to create or run different plug-ins in order to track and identify objects within a system.

The particle outputs from *FIJI* are then used as inputs for a routine written in Python to finalize the analysis and output the quantitative results.

3.3.1 Image Processing Method: Argon Measurements

The original method for analyzing the filaments involved recording the observations with the Ximea xiQ camera CamTool software as video files (.avi) and loading the raw image data into *FIJI*. Importing .avi files into the software can only be done with the **File** → **Import** → **AVI** sequence. This method defaults to uploading the file as an 8-bit image sequence with a length preset by the user that establishes the recording time and frame rate in the CamTool software. However, this approach did not provide sufficient image depth (i.e., the 8-bit images resulted in only 256 grayscale levels), which was ultimately insufficient to resolve the structural features of the filaments and additional pixel intensity information was needed.

Therefore recording the observations as .tiff files with the image sequence option in the CamTool software was the best option due to the ability to save each image as a 16-bit image file (i.e. 65,536 grayscale levels). These files can then be loaded into *FIJI* via the **File** → **Import** → **Image Sequence** method. This allows the images to be loaded in the form in which they are recorded, allowing for the retention of the pixel intensity information. It should be noted that the full sequence of images taken at 1 image per second during the discharge period and is typically more than 7200 images which is a little over 2 hrs for the discharge. The argon data imported into *FIJI* was only a subset of the full sequence; ~100 equally spaced frames were selected to be analyzed (every 72nd image frame).

Once the image sequence has been loaded with a 16-bit format, the sequence could then be prepared for processing. The first step was to threshold the images with a setting of about only the top 8% of the pixels remaining illuminated. Those that remained were set to a level of 65535, while those that were not were set to a level of 0 (i.e. white and black pixels respectively). Figure 3.10 shows the **Analyze → Set Measurements** method used to set what optional preset *FIJI* measurements will be output after processing is complete. The *AREA*, *CENTER OF MASS*, *BOUNDING RECTANGLE*, *SHAPE DESCRIPTORS*, *SKEWNESS*, *MEAN GRAY VALUE*, *CENTROID*, *FIT ELLIPSE*, *KURTOSIS*, and *STACK POSITION.*

After proper measurements are selected, the **Analyze → Analyze Particles** method is used to finally process the data loaded such that the results are displayed and the option to ”Show Outlines” is chosen. The *ANALYZE PARTICLES* plug-in scans each binary image in the stack and uses a ”wand tool” to locate the outer boundary of an object in the image. The *MEASURE* command works in tandem with the wand tool to apply the preset measurements for each object found. After the scan and object measurements are complete for every image in the stack, the ”Results” window (see figure 3.11), in which all of the measurement information is stored for each object in each ”slice” (i.e. image), is automatically displayed. This table numbers each object by when it is measured by the wand tool and records the slice. The results

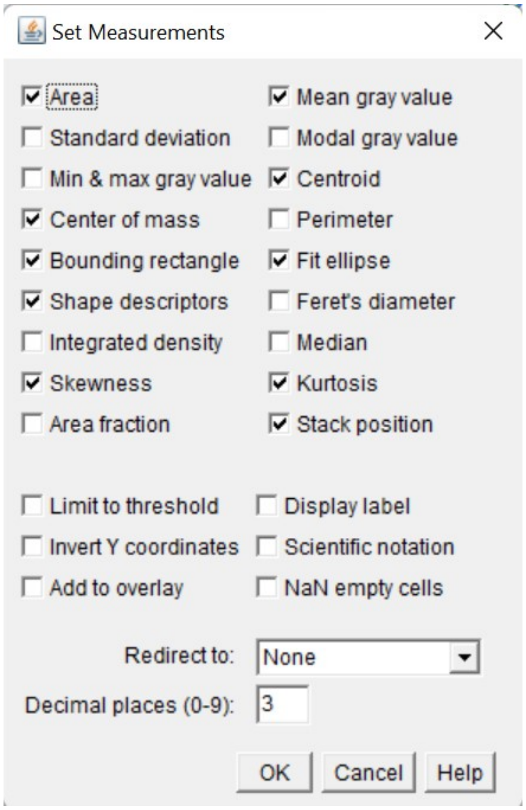
Set Measurements

☑ Area ☑ Mean gray value
☐ Standard deviation ☐ Modal gray value
☐ Min & max gray value ☑ Centroid
☑ Center of mass ☐ Perimeter
☑ Bounding rectangle ☑ Fit ellipse
☑ Shape descriptors ☐ Feret's diameter
☐ Integrated density ☐ Median
☑ Skewness ☑ Kurtosis
☐ Area fraction ☑ Stack position

☐ Limit to threshold ☐ Display label
☐ Invert Y coordinates ☐ Scientific notation
☐ Add to overlay ☐ NaN empty cells

Redirect to: None
Decimal places (0-9): 3

Figure 3.10: Example of the measurement parameters set for the *FIJI* pre-processing using the "Analyze Particles" method.

window can be saved in multiple formats. For the purposes of this analysis the table was saved in comma-separated values (csv) format for input into Microsoft Excel and, eventually, for post-processing using a Python code.

In order to use the information output from *FIJI*, a Python routine was developed to utilize the results obtained as mentioned above. In figure 3.12, the process is illustrated schematically. Figures 3.12(a) through (c) depicts the steps that were previously described, while the final image shows the output from the Python routine. The algorithm sorts the csv filament data

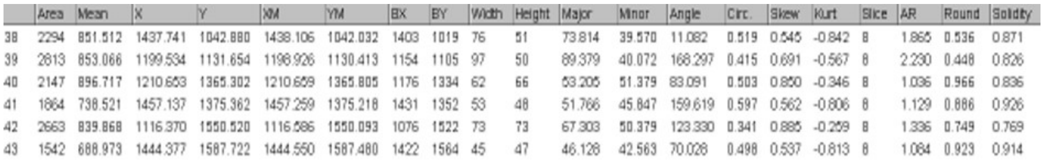

	Area	Mean	X	Y	XM	YM	BX	BY	Width	Height	Major	Minor	Angle	Circ.	Skew	Kurt	Slice	AR	Round	Solidity
38	2294	851.512	1437.741	1042.880	1438.106	1042.032	1403	1019	76	51	73.814	39.570	11.082	0.519	0.545	-0.842	8	1.865	0.536	0.871
39	2813	853.066	1199.534	1131.654	1198.926	1130.413	1154	1105	97	50	89.379	40.072	168.297	0.415	0.691	-0.567	8	2.230	0.448	0.826
40	2147	896.717	1210.653	1365.302	1210.659	1365.805	1176	1334	62	66	53.205	51.379	83.091	0.503	0.850	-0.346	8	1.036	0.966	0.836
41	1864	738.521	1457.137	1375.362	1457.259	1375.218	1431	1352	53	48	51.766	45.847	159.619	0.597	0.562	-0.806	8	1.129	0.886	0.926
42	2663	839.868	1116.370	1550.520	1116.586	1550.093	1076	1522	73	73	67.303	50.379	123.330	0.341	0.885	-0.259	8	1.336	0.749	0.769
43	1542	688.973	1444.377	1587.722	1444.550	1587.480	1422	1564	45	47	46.128	42.563	70.028	0.498	0.537	-0.813	8	1.084	0.923	0.914

Figure 3.11: Example of the Results window after implementing the "Analyze Particles" method. This shows the results for the measurement parameters selected for each "tagged" filament after processing.

results table by "slice" and uses a series of conditional statements based on the shape descriptors given by *FIJI* to classify the filament by type.

3.3.2 Multiple Plasma Processing Method

While the image processing method described in section 3.3.1 was successful in the argon case, it was was not robust enough to be applied to the cases when different gases were used to generate the plasma. There was sufficient variation in image intensity, filament shape, and filament density that a more advanced method of image analysis was needed. The *ANALYZE PARTICLES* sequence is used to gather information on each object found, similar to the analysis of images with argon plasmas. Additionally a custom Java class macro is developed in order to store individual pixel information for each slice in the *FIJI* stack in separate text file formats. Therefore, the complete image information (all 2048 x 2048 pixels) is saved for every image in the stack, and imported into python such that the classification routine can operate on each consecutive image and store the information as a func-

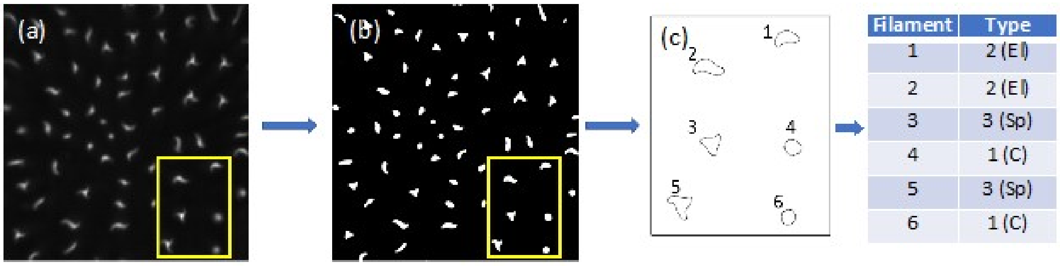

Filament	Type
1	2 (El)
2	2 (El)
3	3 (Sp)
4	1 (C)
5	3 (Sp)
6	1 (C)

Figure 3.12: Sequence to illustrate the processing of images in order to obtain shape parameters and characterize the filament "type". (a) Raw image of Ximea xiQ camera. (b) The image is then processed in the FIJI implementation of the ImageJ software framework, creating the "threshold" image (filaments white and background black). (c) Filaments within a region of interest are tracked and assigned shape parameters by FIJI; the output tables of these shape parameters are then processed using a Python code developed by our group to characterize the filaments into their different, "types": 1 (C – circular), 2 (El – elongated) and 3 (Sp – spiral). For the region of interest shown in Figs. 6(a) and 6(b), the output table of identified filament types is shown to the right.

tion of magnetic field or Hall parameter. A copy of the macro is presented in Appendix A. This approach is presented in chapter 4, section 4.2.1.

Chapter 4

Results and Analysis

This chapter will focus on the results of the image analysis after importing the information produced by the *FIJI* preprocessing. Initially the results of the argon experiment will be presented along with possible interpretations of the results. Subsequently, the more general results of filamentation in multiple plasmas will be presented in the context of Hall parameter and theoretical framework presented in chapter 1. The argon results were previously reported in the paper Williams et al. (2022) [30] and are incorporated in this chapter. The analysis of measurements in helium, neon, and krypton plasmas is presented here for the first time.

4.1 Argon Results

4.1.1 Image Analysis Using Customized Python Code

As described in section 3.3.1, the analysis of argon filaments uses a Python algorithm that incorporates the shape descriptors provided by *FIJI* to classify the filaments by type. Sec. 3.3.2 provides a detailed description of the image analysis process using a combination of FIJI and python routines. A flow chart summarizing the argon filament analysis scheme is presented in Appendix B.

As a result of this analysis, for each image that is processed, each filament is identified and characterized by its shape into a type 1, 2, or 3 filament. Then, a count is made of the number of types 1, 2 or 3 filaments. The output of this analysis approach is that each image represents a measurement of the filament morphology at an instant in time. Because the magnetic field is being ramped as a function of time and its value is recorded simultaneously, the sequence of images corresponds to a set of measurements as a function of magnetic field.

Therefore, this method provides a technique to measure the evolution of filament morphology as a function of magnetic field. Furthermore, a single magnetic field ramp is performed at a fixed pressure and applied rf power. Therefore, sequential measurements are performed by choosing a fixed pressure, gas, and rf power and varying the magnetic field.

Figure 4.1 shows the full results from processing the 150 images selected and uploaded and processed by *FIJI*. The magnetic field values were calculated for each image over the length of the discharge and correlated to match the appropriate ”slice” in the image stack. The figures show the characterization of filaments, by type, over a range from $B = 0.5$ T to 3.5 T at constant RF power of $P = 1$ W at three different pressures P. Figure 4.1(a) shows measurements at $p = 3.5$ Pa (26 mTorr), figure 4.1(b) shows measurements at $p = 4.4$ Pa (33 mTorr), and figure 4.1(c) represents measurements taken at $p = 5.3$ Pa (40 mTorr). The data represented in here shows the total number of filaments characterized as Type 1, 2, or 3 by the Python code as a function of magnetic field. Each shows the evolution of the filament shape with the change of magnetic field. The color coded data points correspond to the different filament types found in the argon magnetic discharge. A commonality shared in each of the three plots, regardless of pressure, is that at lower magnetic field strengths, Type 1 filaments are virtually the only geometry observed and dominate the system. As the field increases, Type 2 filaments begin to be observed in the system and continue to increase in number; while Type 1 filament number decreases. Lastly, a further increase in magnetic field shows Type 3 filaments begin to become observed in the plasma and increase in number density as $B \geq 2$ T. At these magnetic fields, the system is dominated by Type 2 and 3 filaments while Type 1 filaments are relatively absent from the system. Generally, Type 3 filaments are only found at higher magnetic fields, Type 1 filaments mostly appear at lower magnetic fields $B < 2$ T, whereas Type 2 filaments appear at nearly all magnetic fields. Moreover, the total number of filaments existing in the system tends to be low at lower fields and generally increases as the field increases. An interesting result shows that there may be a ”threshold condition” for the different filament types as the absence of the respective data points at magnetic fields below these critical points imply that type of filament was not found.

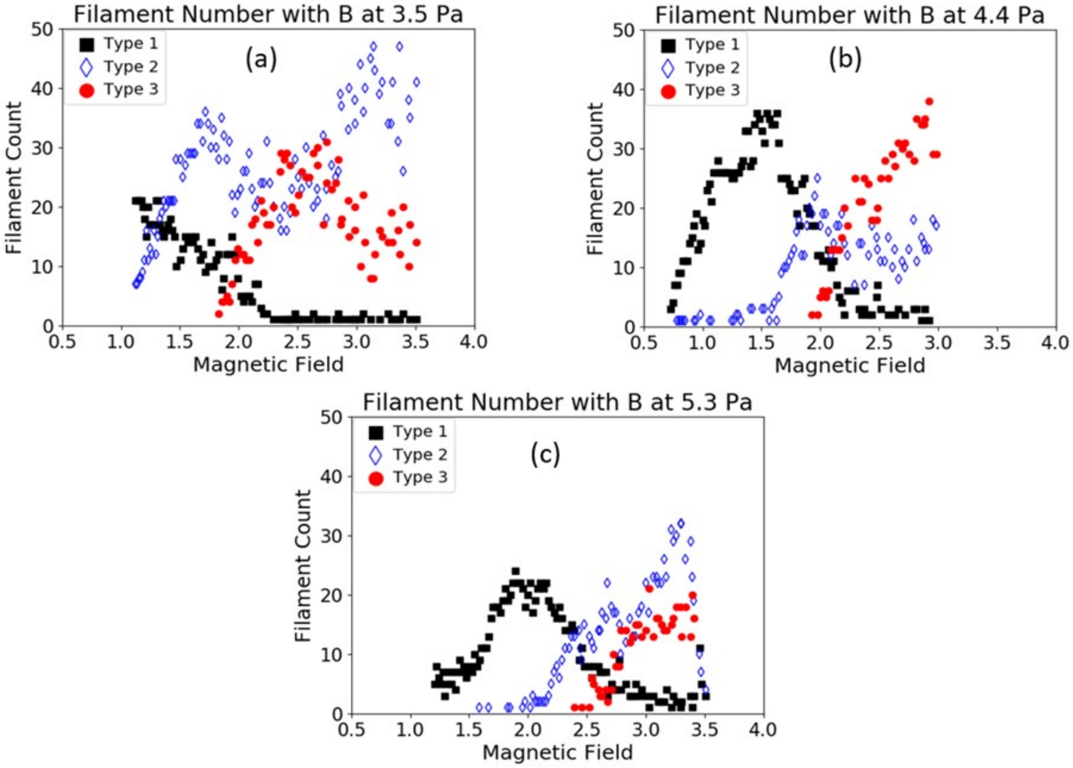

Figure 4.1: Evolution of the observed plasma filaments with magnetic field. The "filament count" represents a larger occurrence of that type of filament. This representation shows that the Type 3 (spiral) appears at higher magnetic field, with a "turn-on" threshold that shifts to higher magnetic field (B = ~1.8 T to ~2 T to ~2.3 T) with increasing neutral pressure. A similar effect may be occurring with the Type 2 (elongated) filaments. (a) p = 3.5 Pa, (b) p = 4.4 Pa, and (c) p = 5.3 Pa. In all cases, the Type 1 (circular) filaments appear to have specific range of magnetic field over which they are present in the plasma and they dissipate at the higher magnetic field settings.

In conjunction with the results discussed above, the data collected over the three pressures, effectively making a small pressure scan, also shows an interesting result. Though the same trend has been described in all three of the magnetic field discharge plots, there is an apparent ”shift” of this trend with pressure. There is evidence that the respective threshold magnetic field condition for each filament type increases with increasing pressure. This result suggests there may be a relation associating magnetic field and pressure and filament formation/evolution.

As discussed in chapter 1, the Hall parameter demonstrates a dimensionless relation between the magnetic field and pressure, which effectively describes the magnetization of the ions within the plasma. The ion Hall parameter is represented as

$$H = \frac{\omega_i}{2\pi\nu_i} \tag{4.1}$$

with the gyrofrequency ω_i and ion-neutral collision frequency ν_i. The ion Hall parameter has been investigated as an effective scaling parameter in many previous studies that investigated magnetized plasmas or dust in magnetized plasmas involving the MDPX device and other lab experiments including works by S. Leblanc, T. Hall, and S. Williams [22, 23, 30].

The gyrofrequency in the numerator of the Hall parameter incorporates the charge $q = 1.602 \times 10^{-19}\,C$, magnetic field B, and ion mass of argon $m = 40u$. The denominator is determined by the thermal velocity of the ions which are at room temperature $(0.025\,eV)$, the ion-neutral collision cross section $\sigma = 3.287 \times 10^{-18}\, m^2$, and the neutral pressure p. A second look at the data above with the type of filaments as a function of Hall parameter is shown in figure 4.2. Plotting the data in this way gives a more insightful representation of how argon filaments evolve through Hall parameter space. Since the Hall parameter is proportional to the ratio of the magnetic field to pressure, i.e. $H \propto \frac{B}{p}$, the field strength and three separate pressures are integrated into the modified Hall parameter itself.

The evolution of the argon filament geometries with respect to the ion Hall parameter shows evidence of a threshold condition for each type. The Type 1 filaments begin to become observed at a magnetization of about $H \geq 1.5$ and increase in number until $H \sim 3$. Afterwards, the number of Type 1 filaments decrease until virtually there are less than a few in the plasma. Type 2 filaments begin to become observed and begin to increase in number with $H \geq 3$. Type 3 filaments appear within the plasma once the magnetization reaches $H \sim 4$ and increase in number until $H \sim 6 - 6.5$. After this the Type 3 filaments begin to decrease in number with still increasing magnetization. It may be captured in the Type 2 data where a decline in number density begins with $H \sim 4.5$ to about $H \sim 6$. Then the number begins to increase again when $H \geq \sim 6$; possibly signifying the beginning of a transition into a turbulent mode.

With the filaments observed in argon as a function of magnetic field and Hall parameter, not only are the structures observed to change in morphology but they also seem to change in relative size with magnetic field as well. At

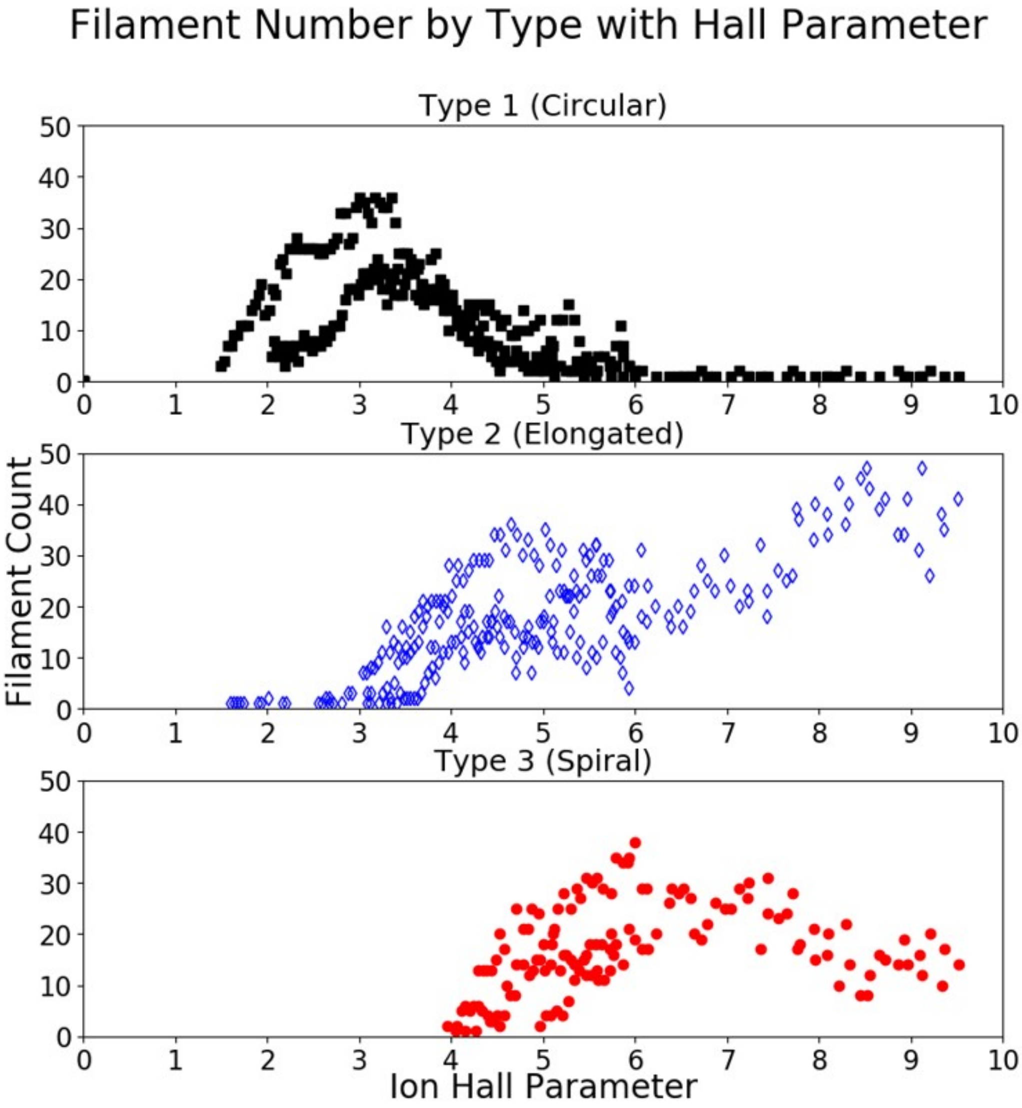

Figure 4.2: Characterization of the filament "type" as a function of the ion Hall parameter using the data that is presented in Fig. 7. It is observed that, when comparing across the three pressures, 3.5, 4.4, and 5.3 Pa, with a scan over the magnetic field, there appears to be a very clear threshold for the appearance of each filament type. Additionally, as type 1 filament count decreases, type 2 and 3 filament count increases.

lower fields, as seen in chapter 3 in figure 3.4(d), at $B = 1.25$ T the filaments appear larger in size in comparison to figure 3.4(a) when $B = 3.5$ T. This trend seems to occur for any of the neutral gas pressures associated with filamentation.

Thus, to estimate an effective filament size, it is necessary to perform a spatial calibration of the viewing area. To accomplish this, the camera is left untouched while the plasma is terminated and the vacuum chamber brought up to atmospheric pressure. Once up to atmosphere, the chamber is opened and a ruler is placed in focus, as seen in figure 4.3, where an image is taken. Since the image area is 2048 x 2048 pixels, a ratio of pixels per mm can be used to calculate the size of the filaments.

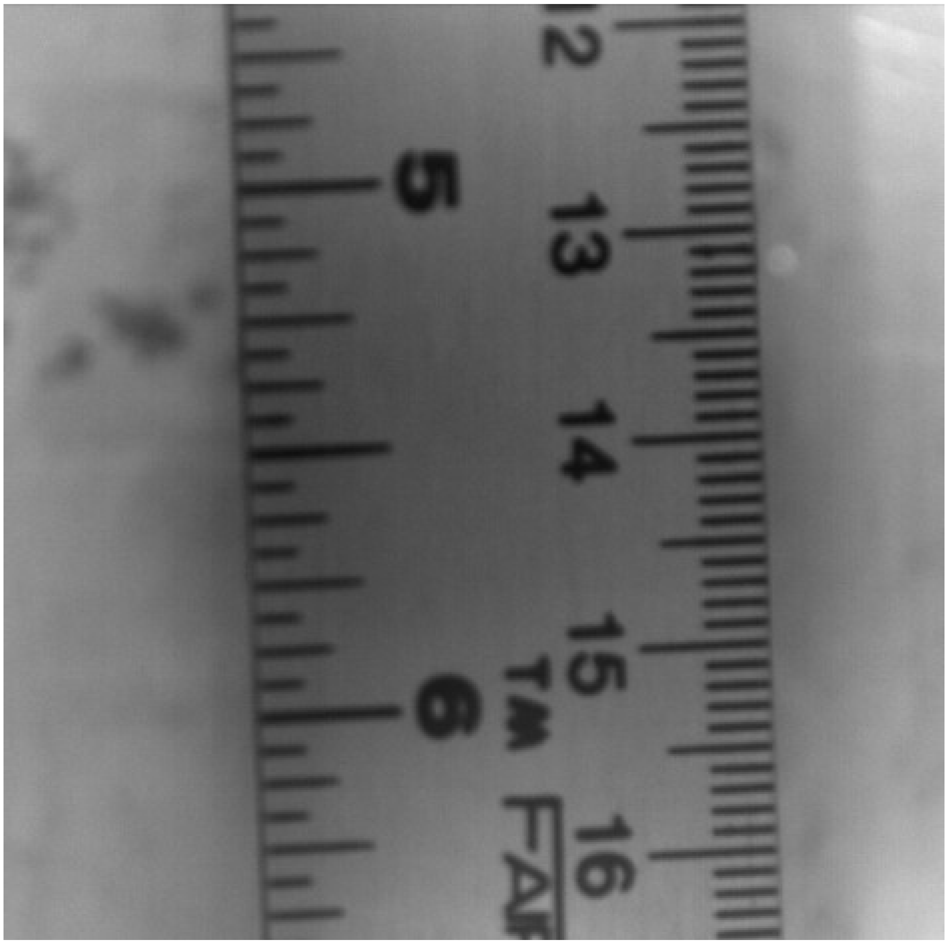

Figure 4.3: Ruler placed in the octagon chamber in the MDPX device. This method allows for a rough spacial calibration for the relative filament size. Given the region of interest of the cmos camera to be 1660 pixels x 1660 pixels, a ratio of pixels per mm can be estimated and applied. The spatial calibration was determined to be 36 pixels per mm (0.027 mm/pixel)

Because the filament morphology can take on more complex shapes like with Type 2 and 3 filaments, the size of the Type 1 (circular) filaments as a function of magnetic field allows for a more robust size comparison. Figure 4.4 illustrates the effective radius of the circular filaments as a function of magnetic field at a constant pressure of 4.4 Pa (33 mTorr). The effective radius of each filament was calculated from the area measurement for that filament given by FIJI (which is the number of square pixels within the bounded region) and the calibration measurement mentioned above (the FIJI process is described in detail in section 3.3.1). We see that generally, the size of the Type 1 filaments decrease as magnetic field increases. This result may suggest that the filament size could have some correlation to the size of the ion gyro orbit. Moreover, the effective diameter of the filaments generally lies in the range of a few millimeters.

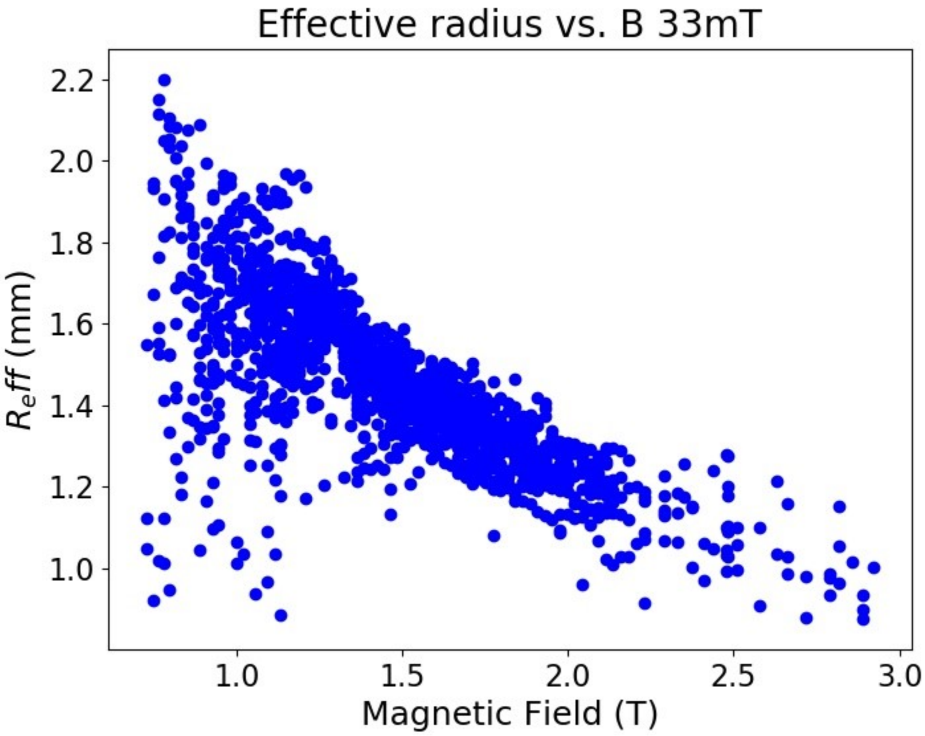

Figure 4.4: Effective area of Type 1 (circular) filaments as a function of magnetic field strength. The data shows that the size of the circular filaments generally decreases as the magnetic field increases. The effective diameter of the filaments are typically on the order of a few millimeters.

Finally, experimental observations of filament behavior give evidence of filament geometries reducing in area as magnetic field increases, while simultaneously increasing in light intensity; i.e. filaments seem to become smaller and brighter with increasing magnetic field. Figure 4.5 verifies this observation by taking a light profile across a Type 1 filament at different magnetic fields. At B = 0.5 T, the profile peak is low in intensity of $\sim$ 287 and a full width half max (fwhm) distance of 163 pixels ($\sim$ 4.5 cm). As the field increases, the peaks intensity and the slope of the profile increase as well. At B = 3 T, the peak height increases to an intensity of 1402 with a fwhm distance of 36 pixels ($\sim$ 1 cm).

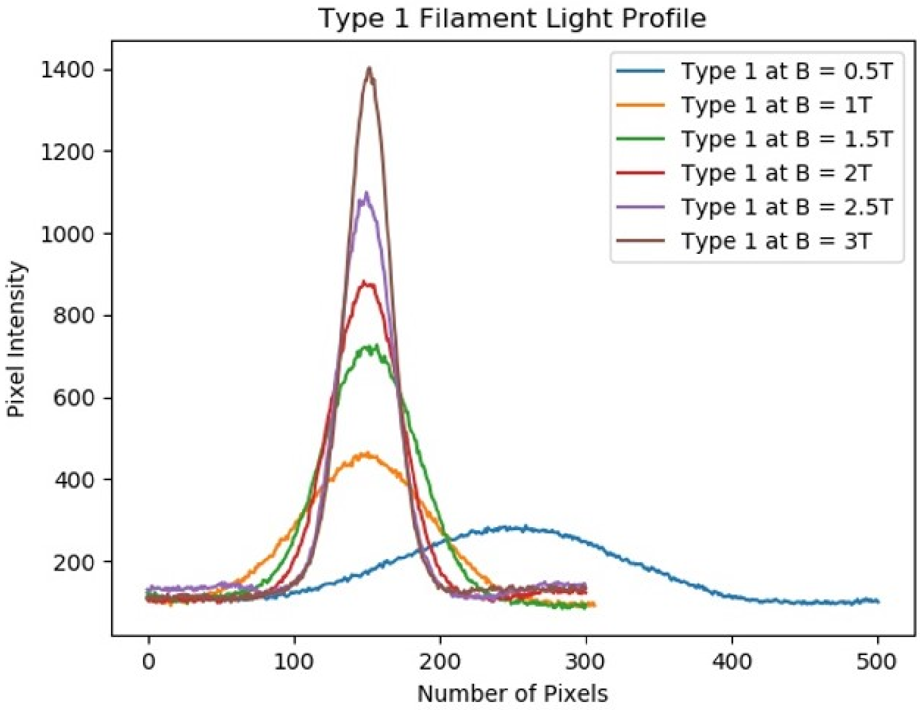

Figure 4.5: Light profiles across a Type 1 filament at different magnetic fields. The plot shows the pixel light intensity as a function of distance in pixels. Profiles were taken at magnetic fields of B = 0.5, 1, 1.5, 2, 2.5, and 3 T. The light profiles increase in intensity and slope as a function of magnetic field. This indicates that the Type 1 filaments decrease in size but increase in light emission with increasing magnetic field.

4.1.2 Argon Discussion

The results indicate that the plasma must be at least partially magnetized for filaments to form (i.e. $H_e >> 1$ and $H_i \geq 0.5$). Therefore this supports the filament formation condition hypothesized in chapter 1 that a combination of ion magnetization and local plasma density gradients may provide the conditions to establish the drift wave instability which may be necessary to form filaments and determine individual shape.

The various plasma behaviors and dynamics occur due to a sensitive balance regimes between gyroradius, magnetization, and Debye length in magnetized plasmas are achieved. Examples of these plasma behaviors were simulated by Menati et. al [28, 24], and Hall et. al [23] observed dust behaviors in the MDPX device with a mesh grid. The work by T. Hall showed that the ion Hall parameter may be an indicator of how the bonding parameter, Ψ, changes with magnetization and, as a result, affects the ordered structures observed in the dust grid. Both works highlight and attempt to understand the physical mechanisms within the mentioned regimes using the ion Hall parameter as a partial guide.

4.1.3 Conjectured Criteria for Filament Formation in Argon

M. Menati's three-dimensional simulation results [28, 24] indicate that in order for plasma filamentation to occur, there are two important conditions that must be met. The ion gyroradius must be below the ion-neutral mean free path length and the electron Debye length; i.e.

$$\rho_i \leq \lambda_{mfp} \tag{4.2}$$

$$\rho_i \leq \lambda_{De} \tag{4.3}$$

For the experiments with argon, the ions and neutral atoms are assumed to remain at room temperature $T_i = T_n = 0.025$ eV and the field range of 0.75 T $\leq B \leq$ 3.5 T, ion gyroradii takes approximate values of 0.21 mm $\geq \rho_i \geq$ 0.046 mm respectively. The mean free path for the full range of pressures tested, 0.67 Pa (5 mTorr) $\leq p \leq$ 6.0 Pa (45 mTorr), takes the value range of 1.2 mm $\geq \lambda_{mfp} \geq$ 0.2 mm. Therefore, it follows that Eq.[4.2] is met such that $\rho_i \leq \lambda_{mfp}$.

The second criterion, $\rho_i \leq \lambda_{De}$ Eq.[4.3], is much more difficult to test. In the majority of low temperature plasmas such as these, a Langmuir probe is the mostly frequently used diagnostic tool to make these measurements. While there are extensive and detailed theoretical models to extract the electron density and temperature from an unmagnetized plasma, theories of probe performance in strongly magnetized plasmas are limited.

The key physical reason for the limited performance of the Langmuir probe with increasing magnetic field is that the effective collecting surface of the probe becomes severely limited with increasing magnetic field. This is illustrated conceptually in figure 4.6. As a result, electron and ion fluxes to the probe are reduced.

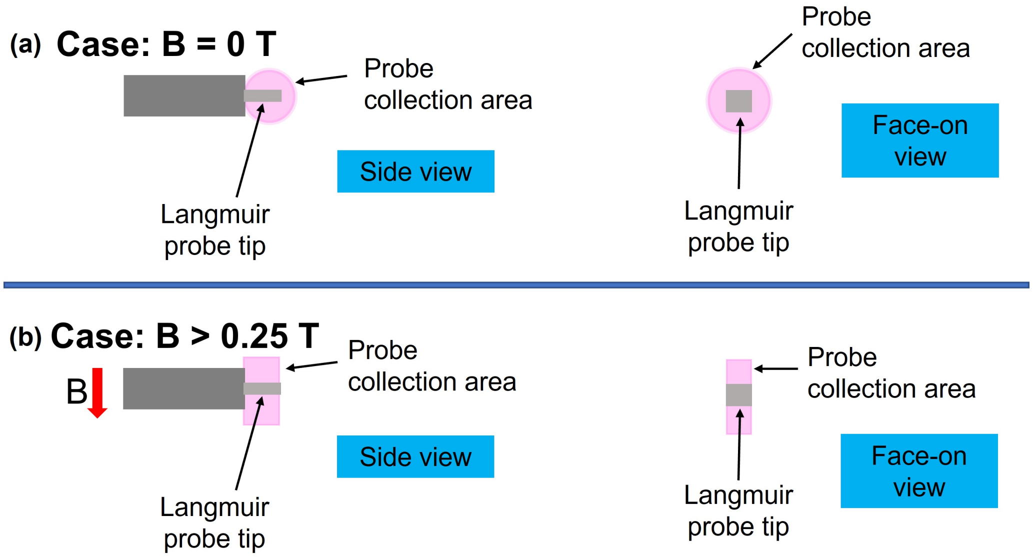

Figure 4.6: Illustration of the plasma collection area geometry from the side and from a face-on view for a Langmuir probe. The probe placement within the chamber remains at the same location, however when a magnetic field is applied, the collection area geometry changes from a spherical geometry as in (a) to a rectangular area illustrated in (b).

Thus, it becomes very difficult to measure the electron density and electron temperature in magnetic fields above $B \sim 0.25$ T. This becomes an obvious issue when trying to diagnose the plasma in a filamented regime since the filaments begin to form at magnetic fields of $B \sim 0.5$ T. This geometric effect is shown in the Langmuir probe trace data taken on MDPX from B = 0 to B = 1 T. The figures below illustrate the difficulties of applying Langmuir probe theory to magnetized plasmas. All probe measurements were taken with a consistent input RF power, $RF = 1$ W, and a probe tip with a radius, $r = 0.5$ mm.

The first example, which is shown in figure 4.7, is a normal probe trace taken with no magnetic field applied (i.e. $B = 0$ T). The trace is performed for multiple pressures with constant RF power of 1 W. This measurement was consistent with previous probe measurements performed on MDPX. The floating point voltage ranged from 9 V to 12 V depending on pressure with a corresponding electron temperature $T_e = 3.2 \pm 0.5$ eV and densities of $n \sim$ 0.4 to $1.2{\times}10^{15}$ m^{-3}. These values give electron Debye lengths of $\sim$ 0.38 to 0.68 mm. All values given are typical for an MDPX argon plasma and are consistent with results presented by Menati.

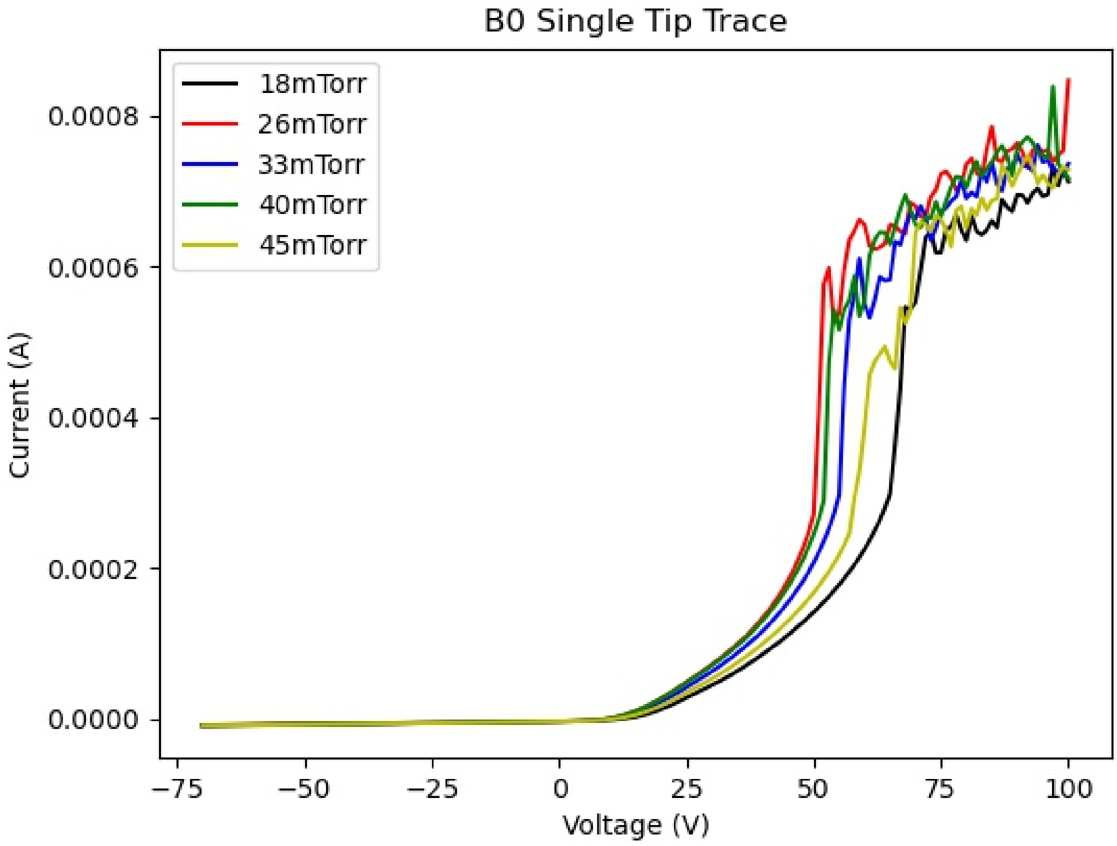

Figure 4.7: Single tip Langmuir probe I-V trace of MDPX argon plasma for multiple pressures with an input power, $\mathbf{P_{RF} = 1}$ W. The plot shows the current collected by the probe over a sweep of voltages from -70 V to 100 V without a magnetic field present, $\boldsymbol{B} = 0$ T.

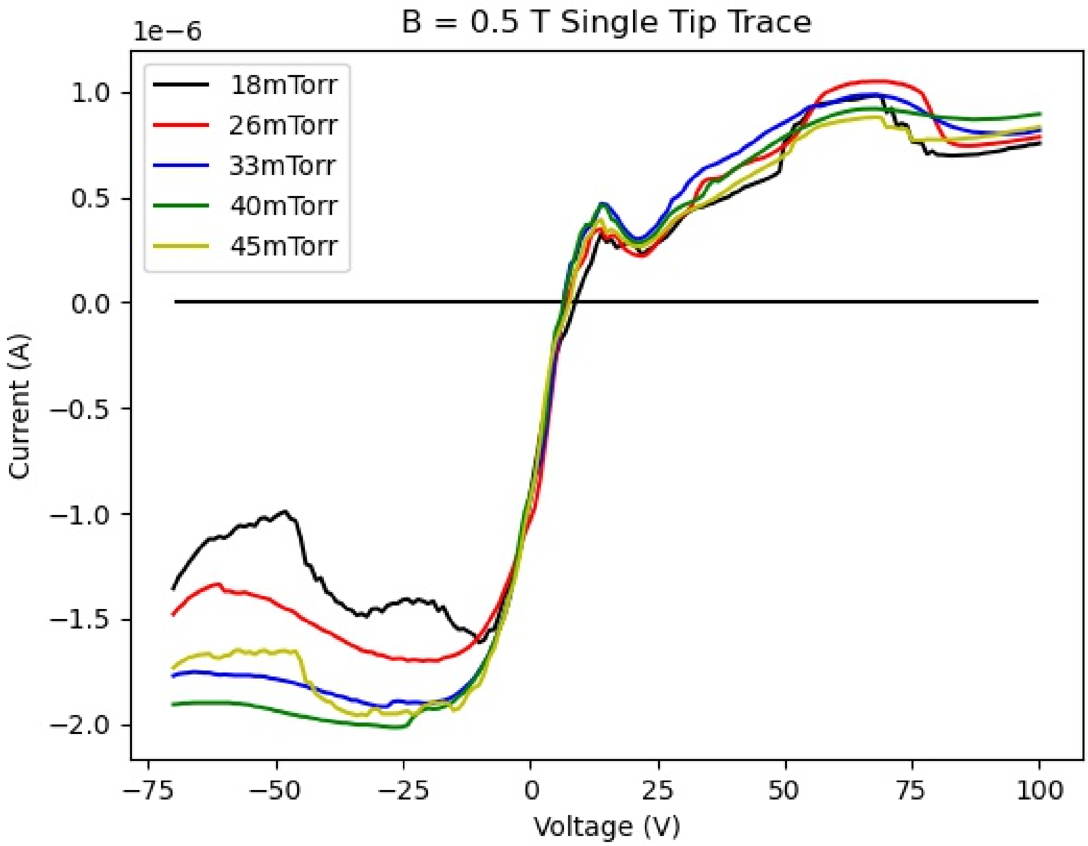

Figure 4.8: Single tip Langmuir probe I-V trace of MDPX plasma for multiple pressures with an input power, $P_{RF} = 1$ W. The plot shows the current collected by the probe over a sweep of voltages from -70 V to 100 V with an applied magnetic field, $B = 0.5$ T. There is a clear difference in this trace compared to the $B = 0$ T case. Probe theories break down in the presence of strong magnetic fields.

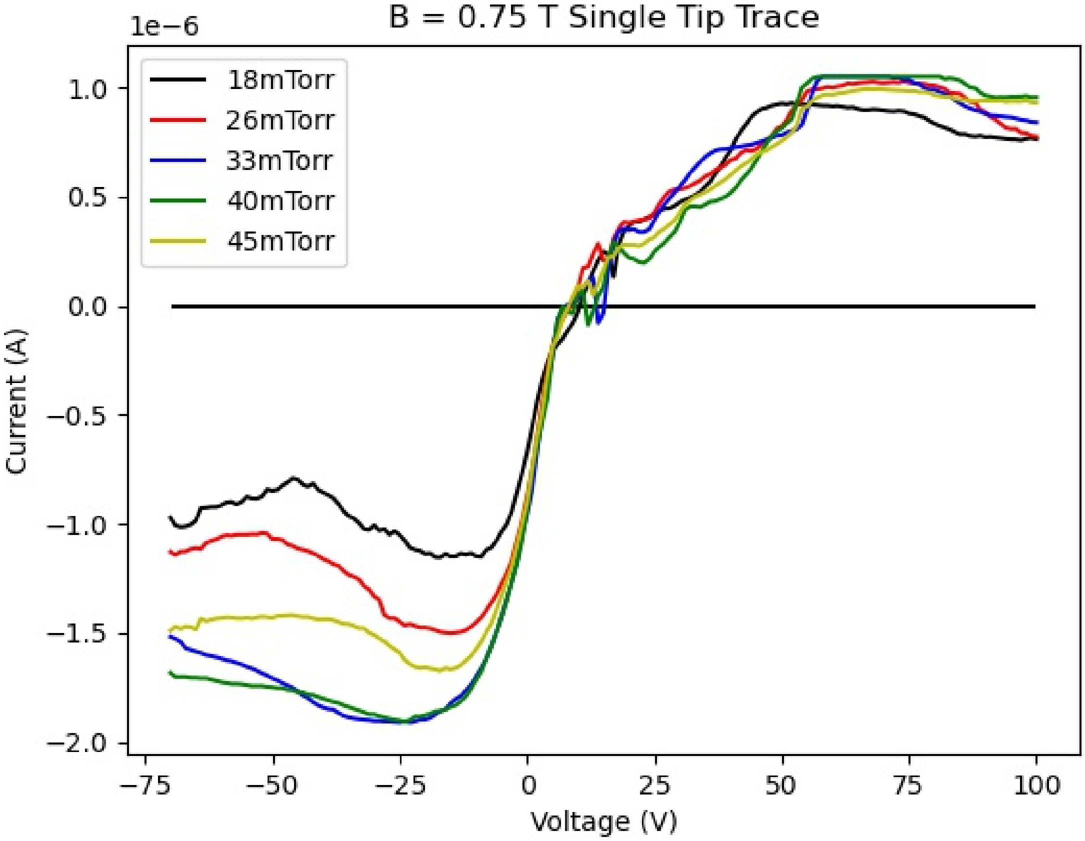

Figure 4.9: Single tip Langmuir probe I-V trace of MDPX plasma for multiple pressures with an input power, $\mathbf{P_{RF} = 1}$ W. The plot shows the current collected by the probe over a sweep of voltages from -70 V to 100 V with an applied magnetic field, $\boldsymbol{B}$ = 0.75 T.

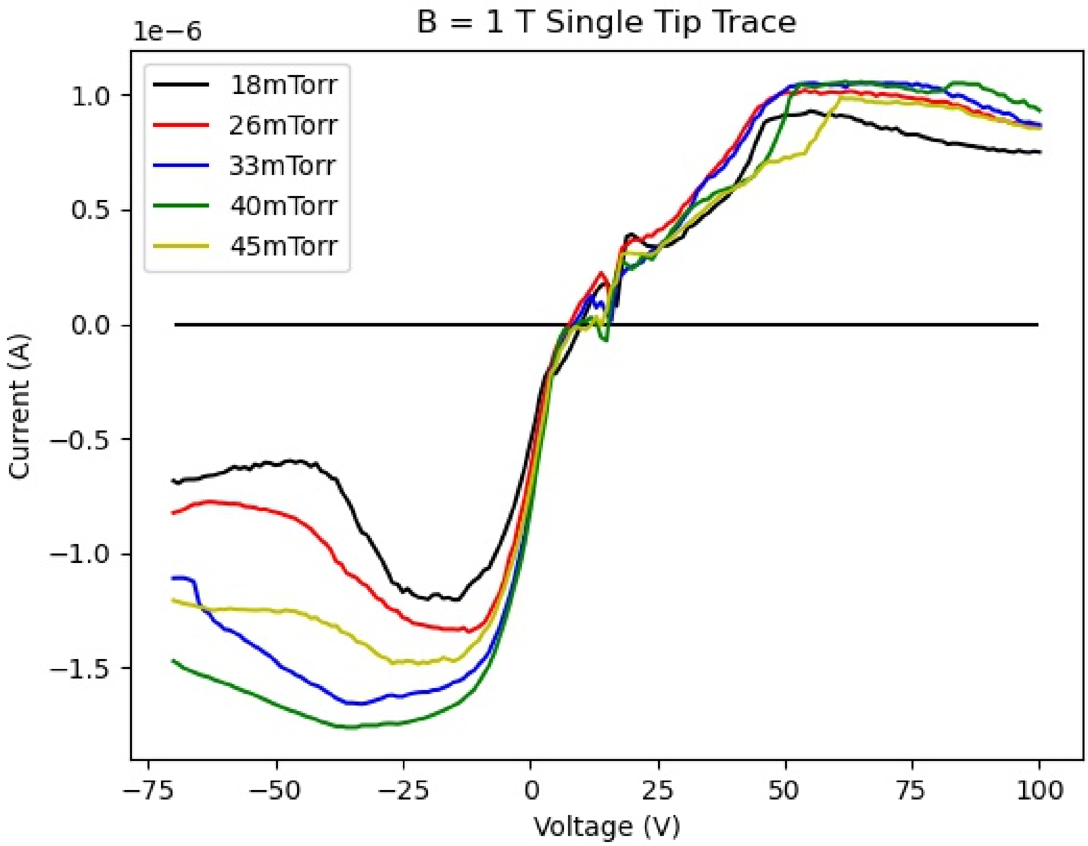

Figure 4.10: Single tip Langmuir probe I-V trace of MDPX plasma for multiple pressures with an input power, $P_{RF} = 1$ W. The plot shows the current collected by the probe over a sweep of voltages from -70 V to 100 V with an applied magnetic field, $B = 1$ T.

Figures 4.8 - 4.10 show the modification of single tip Langmuir probe measurements when a strong magnetic field is present. The magnitude of current values measured when $B = 0$ T are between 0 and 1 mA, whereas with a magnetic field, the current magnitude quickly decreases to approximately 1 μA; about 1000 times less. Although all pressures tested in each figure give similar trends for the respective field strength, the trends shown with a magnetic field present give nearly symmetric measurements around the x-axis at 0 A of current. Whereas, the trend with no field present gives the expected result of a typical I-V probe trace over a voltage sweep. The only similarities the two regimes seem share are the ion saturation portion of the traces. The floating potential remains within a range of a few volts for both regimes (between ∼7 V and ∼15 V). The electron temperature, T_e, can be calculated by the equation:

$$V = V_s - \frac{kT_e}{2e} ln\left(\frac{m_i}{2\pi m_e}\right) \tag{4.4}$$

where V is the probe potential, V_s the potential at the sheath edge, k is the Boltzmann constant, m_i is the average ion mass, and m_e is the electron mass. The difference $V - V_s$ represents the voltage across the sheath. Therefore, we can approximate the electron temperature to be between 1.5 and 3.2 eV thus the temperature of the background plasma may not change much with a magnetic field (or filaments) present.

Prior to the transition region of the probe trace is the ion saturation region. The ion saturation portion for the $B = 0$ T case is very stable and exhibits the expected result of a typical Langmuir probe voltage sweep. The information collected from the ion saturation region for $B > 0$ T was a subset of the data from a segmented range of V_p = -75 V to V_p = -50 V, which corresponds to the more linear portions of the saturation. All three voltage sweeps at field exhibit similar behavior in the ion saturation region. Although initially there is some evidence of linearity, when the probe voltage increases above 50 V, the probe measurements tend to a local minimum before increasing in the transition region. The results of the data collected and analyzed is presented in the figure below.

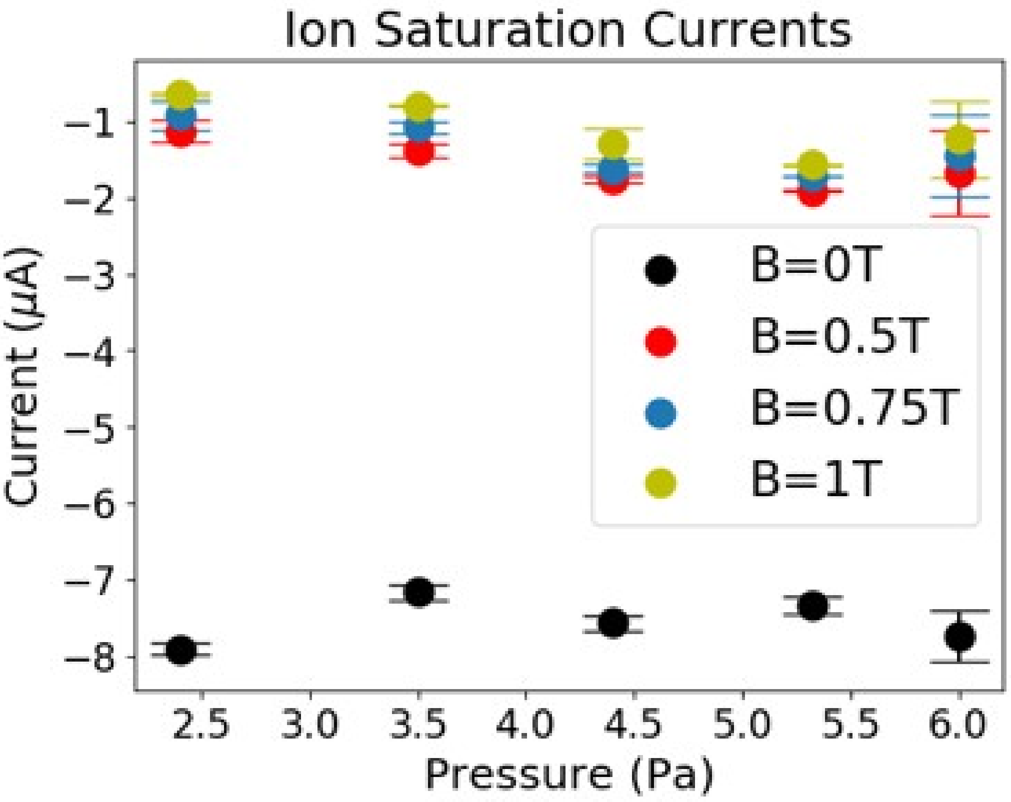

Figure 4.11: Measured ion saturation current as a function of pressure and magnetic fields in MDPX at fixed RF power. There is an initially large (∼ a factor of 8) drop of the ion saturation current between B = 0 T and B = 0.5 T, but only a modest (< factor of 2) change in the ion saturation current between B = 0.5 T and B = 1 T.

There may be some information able to be extracted from the analysis in figure 4.11. The ion density can be calculated from the ion saturation current by the equation:

$$I_{sat} = 0.6 q_e n_i A_{probe} c_s \tag{4.5}$$

where q_e is the electron charge, n_e represents the electron/ion density (invoking quasineutrality), and c_s being the sound speed such that,

$$c_s = \sqrt{\frac{k_b T_e}{m_i}} \tag{4.6}$$

where k_b is the Boltzmann constant, T_e is the electron temperature assuming $T_e >> T_i$, and m_i the mass of the ions. Solving for n_e in equation 3.3, we can estimate the ion density given the approximate ion saturation values from Figure 4.11 for the four cases.

In the figure, measurements of the average ion saturation current for a single tip cylindrical Langmuir probe of radius, $r = 0.5$ mm and length, $l = 8$ mm is shown. The average and standard deviation for the collected currents for bias voltages between V_p = -70 and -50 V for a neutral pressures in the range, p = 2.4 to 6.0 Pa (18 to 45 mTorr) and for magnetic fields from B = 0 to 1 T. For the B = 0 case, the I_{sat} currents for the pressures tested all fall between -7 and -8 μA. However, for the $B \neq 0$ case, the I_{sat} currents all fall between ∼-0.5 μA and ∼-2.5 μA. There is an initial drop (∼ a factor of 7 or 8) in current between B = 0 T and B = 0.5 T, but only a modest drop (∼ a factor of 2 or less) between B = 0.5 T and B = 1 T. With a closer inspection of this drop in current, under the assumption that the ions are at room temperature, the ion gyroradius is calculated to be $\rho_i = 0.32$ mm. This is smaller than the radius of the probe itself, therefore, the initial drop in current could be due to a geometric reduction in the effective collection area.

Typically in an unmagnetized plasma, the probe collects charges in a uniform volume around the probe tip. Though with a high magnetic field present, the collection volume is in the form of an enlongated flux tube of ions/electrons. With a bias on the probe such that $V_{probe} >> V_p$, where V_p is the plasma potential, ions and electrons stream towards the probe depending on the sign of bias. This can lead to possible erroneous current measurements or simply measurements that do not follow Langmuir probe theory. Nevertheless, the magnetic field probe results may indicate that the electron/ion density may not change significantly when transitioning from a uniform background plasma regime (i.e. $B = 0$ T) to a self-organized filamented plasma regime (i.e. $B \geq 0.5$ T).

Thus, with the electron/ion densities remaining about the same, the Debye lengths also remain about the same (~ 0.38 to 0.68 mm). Additionally, the Larmor radius (gyroradius) for the magnetic fields at which the probe diagnostics were performed take on values of ~ 0.16 to 0.32 mm. Therefore, the second condition, $\rho_i \leq \lambda_{De}$, is satisfied.

4.2 Characterization of Filaments in Other Gas Species

The argon filament results are illuminating; particularly in regard to the possible role of ion magnetization(i.e. Hall parameter) in filament morphology. As shown in section 1.1.3, the Hall parameter is proportional to B/P (Eq.[1.28]) but when incorporating different gases, the mass term cannot be neglected. Therefore, the Hall parameter can also have a weak dependence on mass as shown in Eq[4.7] below.

$$H \sim \frac{B}{\sqrt{m}P} \tag{4.7}$$

Using different gas species for plasma generation enables a more fine-tuned exploration of the Hall parameter. Given the characteristic magnetic field and pressure ranges, neon plasmas allow for a coarse scan of magnetization space whereas krypton allows for a finer scan compared to the argon scan due to their respective masses.

4.2.1 New Python Analysis

With the acquired filament image data with plasmas of different neutral gas species such as in figures 3.7 and 3.8, the primary objective was to classify filamentation much like the argon experiment. Although in the case of krypton specifically, new 4-arm spiral filaments were observed, but the original python code only accounted for Type 1, 2, and 3 because those were the filament morphologies found in the argon pressure scan and discharge experiments. The *FIJI* shape parameters that allowed a successful characterization of the three filament types in argon were found to be insufficient to properly capture the broader structural variations that occurred, for example, in krypton plasmas. Therefore, a more refined shape analysis technique needed to be developed.

In order to build this type of routine, the foundation of the processing method needed to be based on the raw pixel values of the images the *FIJI* macro used to acquire the raw pixel values can be seen in Appendix C. If a routine is able to access the raw images, locate each filament in a given image and perform a complete azimuthal walk at a particular radius around the filament (in two dimensions), we should be able to resolve almost any type of filament observed. This approach is illustrated graphically in Fig. 4.12. Here, a circular path is drawn around a four-armed filament. The pixel intensity as a function of azimuthal angle is plotted revealing the four peaks.

The code uses a multi pass approach for each identified filament to ensure a robust identification method. Figure 4.13 shows a direct comparison of the output of the of the original and newer filament identification methods for the previous argon data. This results illustrates that the new identification method is benchmarked against the original with excellent agreement. Appendix C provides extended detail into the preparation of the updated Python script used for the new analysis technique.

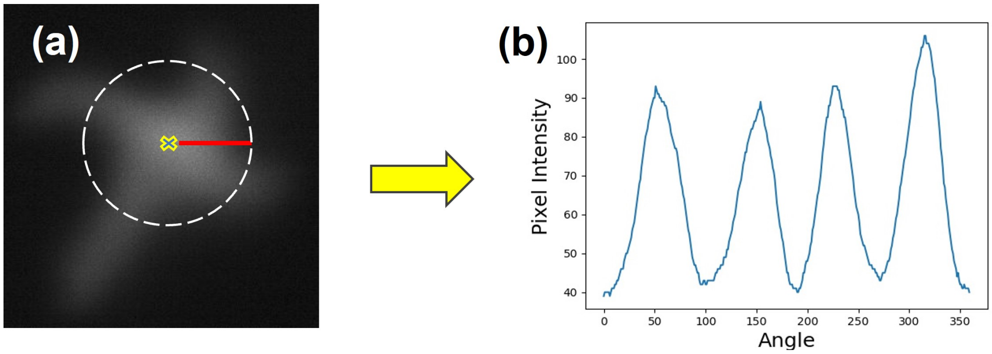

Figure 4.12: Visualization of the new python algorithm. The origin of the determined radius for each filament (4-arm shown here) is placed at the center of mass of the object. An angle which is stepped from 0 to 360 is used in combination with polar coordinates to ”walk” around the filament as shown in (a). The output array of pixel values after the walk is plotted in (b). As the angle increases, the pixels go from dark to bright as the walk crosses the arms of the filament. The number of peaks correspond to the number of arms and therefore the type of filament.

A requirement is the confirmation that the new analysis method yields valid results. To verify that the new routine can give the desired results, it was first tested with the argon data such that the results of the new routine should match the results of the original. The comparison is shown in figure 4.13. As seen in the figure, the results match extremely well. The original magnetic field scan results by pressure are illustrated on the top of the image while the same results from the new method are illustrated on the bottom.

The advantage to using the new method is the ability to categorize higher order filaments (i.e. > than type 3).

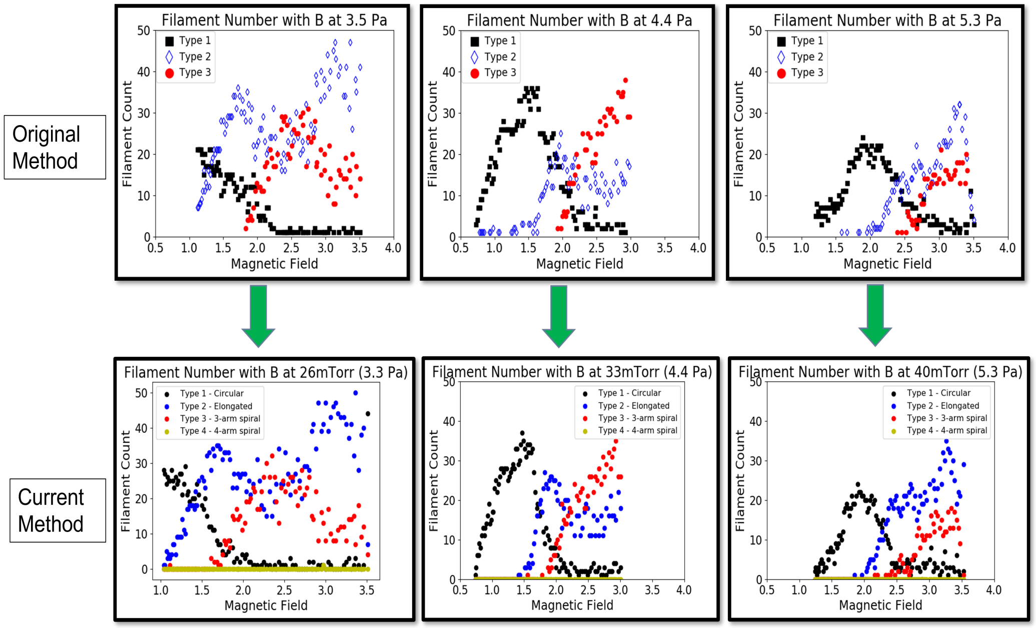

Figure 4.13: Comparison of the original analysis method to the new analysis method. The new method agrees very well with the original method but is not limited to the categorization of only three types of filaments.

The images shown in the top half of figure 4.13 labeled ”Original Method” are the same figures presented in figure 4.1 earlier in this chapter. Whereas, the figures on the bottom half are the same data as in figure 4.1 but presented with the new method of filament classification. The same set of data presented by the two methods agree with one another very well. Therefore the new method is verified as an accurate method of filament classification and will be applied to all three plasmas presented below (neon, argon, and krypton).

4.2.2 Plasmas in Other Gas Species

The filament analysis for all of the gases tested follow similar processes as described in the previous section. Each plasma was subjected to a magnetic field discharge at three separate pressure values. The new filament classification routine was applied to the collected data for those experiments and the results are shown in figures 4.15-4.17.

All three figures show the magnetic field discharge experiment results for the various pressures tested similarly to argon in figure 4.2. **Neon filaments** were found at slightly lower pressures than argon (p = 2.6, 4, and 4.4 Pa) over the same magnetic field range but exhibit more turbulent behavior (as described in section 3.2) above 1.5 T. Neon filaments appeared at a lower field strength than argon filaments, which agrees with predictions based on ion magnetization thresholds.

Argon filament behaviors and morphologies are discussed in sections 4.1.1 and 4.1.2. For argon, Type 2 filaments begin to follow a similar trend the Type 1 and 3 filaments follow, but as seen in helium and neon, at high magnetization, the plasma filaments transition into a ”turbulent mode” in where the Type 2 filaments dominate. The point of this transition into a turbulent regime is unknown and seems to occur when the ion Hall parameter is above a value of 2.

Following in a similar trend with increasing mass, **krypton filaments** were observed at higher pressures than both neon and argon (p = 4.4, 6, and 6.6 Pa). The morphologies are also consistent with those found in neon and argon plasmas. Circular filaments, elongated filaments, and spirals are observed, however, both three and four arm structures exist freely in krypton. The trend with magnetic field strength in krypton is very comparable to the observed trend in argon. Type 1 filaments are the first observed at lower fields beginning $\sim$ B = 0.5 T and increase in number to a point as magnetic field increases. Subsequently Type 2 filaments appear in krypton $\sim$ B = 1.5 T for pressures of 4.4 and 6 Pa and between 2 and 2.5 T for 6.6 Pa. These filaments also increase in number as magnetic field increases as seen in argon and neon. While Type 3 filaments begin to appear with B $\geq$ 3.0 T and Type 4 filaments at B $\sim$ 3.2 T.

Type 4 filaments, as discussed in the above section (3.2.1), are new filaments found to exist in krypton at high magnetic fields. These structures were predicted by M. Menati et al. [28] through simulations which modeled the initial formation of the filament structure (refer to fig 1.8). The comparison is shown in figure 4.14.

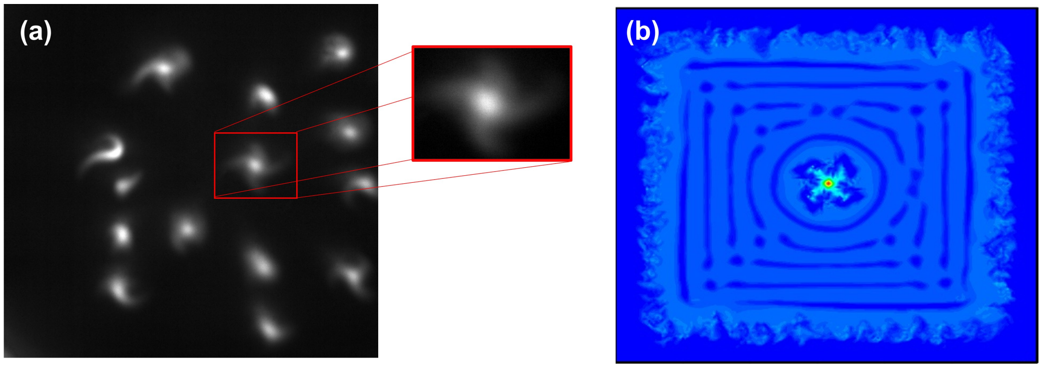

Mohamad Menati, et al., Phys. Plasmas **27**, 022101 (2020)

Figure 4.14: This figure shows the existence of the 4-arm filament in a krypton plasma at $\boldsymbol{B}$ = 2.2 T, pressure of $\boldsymbol{p}$ = 5.6 Pa (42 mTorr), and a power of $\mathbf{P_{RF}}$ = 3 W in part (a). The illustration in part (b) shows the results of the filamentation model simulated in argon by M. Menati. The Type 4 filament was predicted to appear prior to finding this type for the first time.

Now that we are able to appropriately identify all types of filaments observed (and any new filaments that may appear), it is logical to revisit the modified ion Hall parameter to investigate the potential role that ion magnetization has on filamentation formation in neon and krypton in addition to argon. The following figures depict the behavior of filament type for the different plasmas at the various pressures tested.

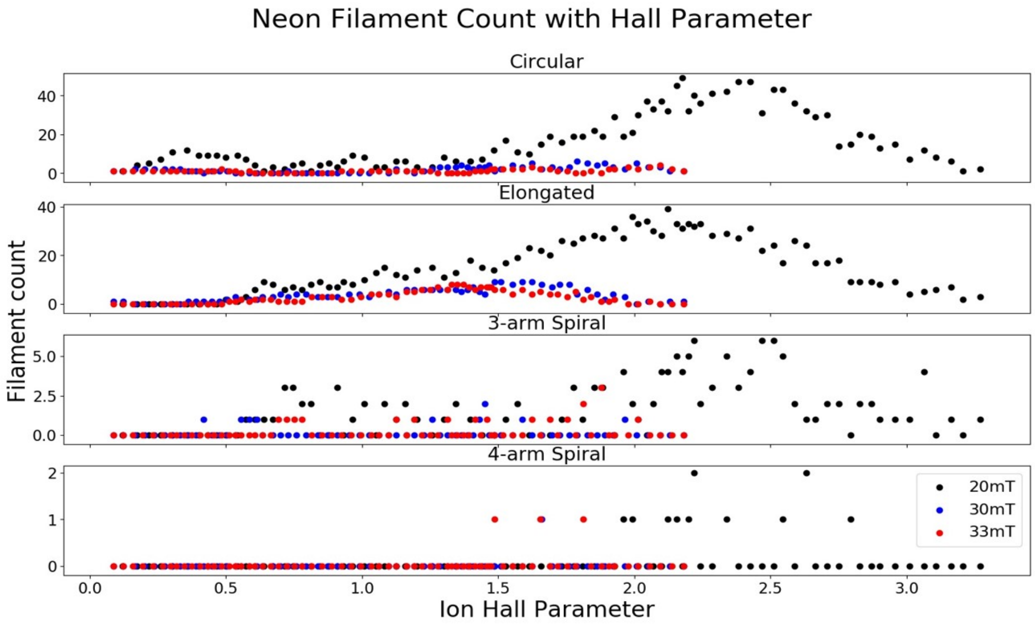

Figure 4.15: Characterization of the filament type as a function of ion Hall parameter in a neon plasma with the three pressures shown (p = 2.6, 4, and 4.3 Pa). This figure shows the turbulent nature of neon and the partial break-down of the analysis code. Type 1, 2, and 3 filaments are represented well by the data, however Type 4 filaments have not yet been observed in neon but the algorithm identifies the presence of Type 4 filaments in the plasma. The pattern of Type 1 filaments occurring first at lower magnetization with Type 2 and 3 structures forming successively at higher magnetization.

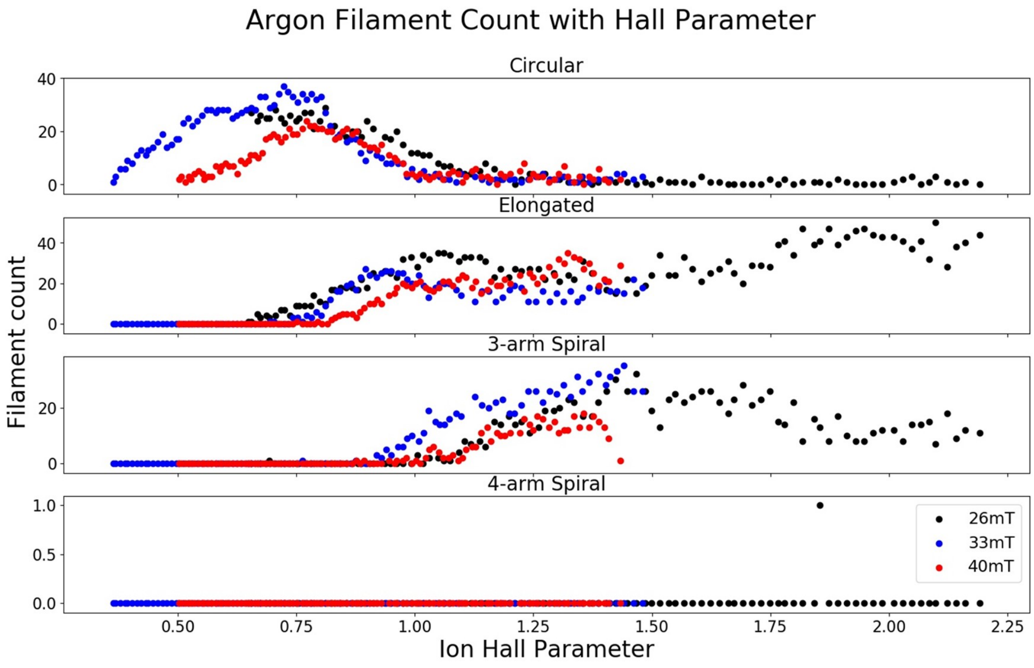

Figure 4.16: Characterization of the filament type as a function of ion Hall parameter in an argon plasma as presented in Figure 3.2. The three pressures tested are shown in this figure (p = 3.5, 4.4, 5.3 Pa).

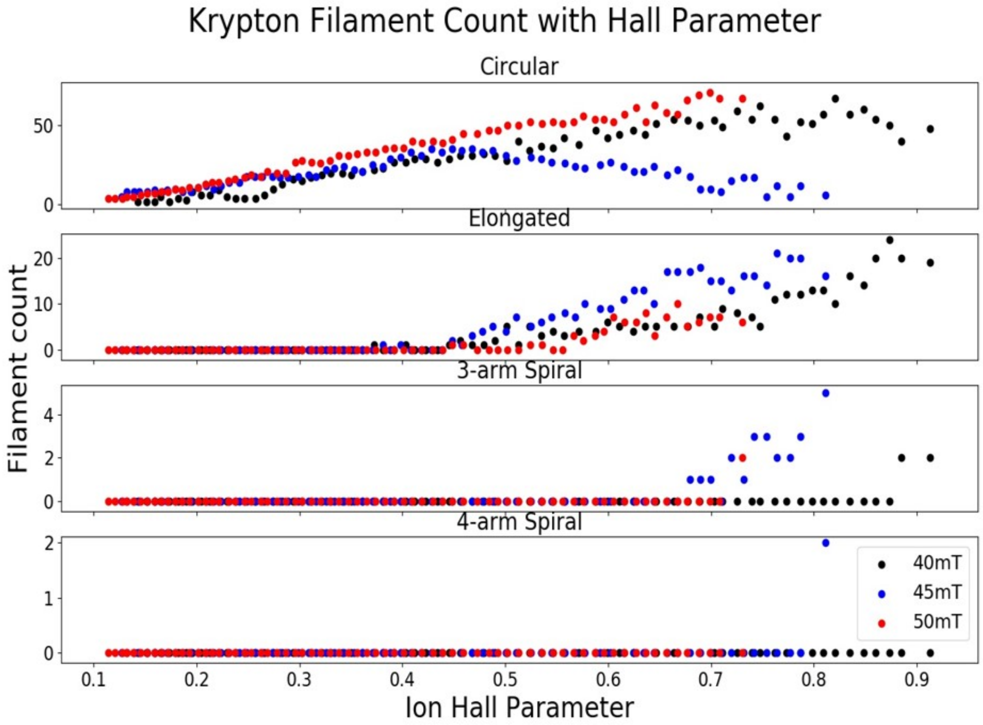

Figure 4.17: Characterization of the filament type as a function of ion Hall parameter in a krypton plasma with the three pressures tested shown ($p = 5.3$, 6, and 6.6 Pa). This figure shows a similar pattern as seen in figure 3.12 with argon. Each type of filament is observed successively as a function of magnetization beginning with Type 1 and progressing through Type 4 with the latter forming at relatively high Hall parameter (at magnetization $\sim$ 10 times higher than the magnetization threshold of Type 1 filaments).

The figures above represent the formation of filaments in different plasmas as a function of Hall parameter. Due to the effect of the mass factor in the denominator of the ion Hall parameter function, the ion Hall parameter space for the MDPX operating range of 0 T to 3.5 T, this corresponds to ion Hall parameter range from 0 to 2 for krypton vs 0 to 3.5 for neon. The results yield a very similar pattern of results as in figure 3.2 with argon. The circular filaments appear to populate the system initially followed by Type 2, 3, and 4 successively. These results are shown quite clearly in the argon and krypton experiments, whereas with the neon experiment, the results are consistent but not as clear. Finally, it is noted that in spite of the significant efforts that have been placed in testing and benchmarking the analysis codes, additional work can always be done to refine the analysis. An example of this the identification of a single Type 4 filament in the neon results when - upon visual inspection - it is not obvious that a Type 4 is present. Nonetheless, we remain highly confident that in spite of this, the analysis technique is accurate, reproducible, and fairly robust.

It also follows that the magnitude of the difference in the ”turn-on” point for the different filament types (particularly for types 1-3) may increase with mass. For neon, Type 2 and 3 filaments begin to populate the system at approximately the same value of magnetization of 0.4 while Type 1 filaments occur at a value of around 0.2 such that the difference is about 0.2. In argon, The difference between Type 1 and 2 filaments is around 0.3 which is a similar difference between the Type 2 and 3. The difference between Type 1 and 2 filaments in krypton is much larger with a value of about 1. Furthermore, the difference in magnetization between Type 2 and 3 is a value of about

0.5. The most apparent change in the difference in magnetization between the filament types seems to occur for the Type 2 and Type 3 separation.

It should be noted that although the ion Hall parameter may prove to be an acceptable metric used to represent the data, there may be an even more appropriate metric that could be used to display the data such that more physical mechanisms/correlations can be seen clearly. The ion Hall parameter is used in previous works by T. Hall and M. Menati [23, 24] and is seen to have a strong correlation to the data represented. Furthermore, the ion Hall parameter incorporates pressure, magnetic field, and mass which are the controllable parameters within the experiment. Therefore it is used as the main functional criterion for this work.

To complete the analysis, it is in our interest to investigate the connection of physical quantities to the filament geometries. As discussed in section 4.1.1, the size of the filament is dependent on the magnetic field applied. Therefore, it follows that there may be some connection between the size of the ion gyro orbit to the size of the filament. Figure 4.18 shows the ratio of the effective radius of Type 1 (circular) filaments to the ion gyroradius as a function of ion Hall parameter (magnetization). The data shows that the size of the filament effective radius, when compared to the gyroradius, initially increases nonlinearly with ion magnetization for all three plasma types. It is seen more clearly in neon that at an ion Hall parameter of around 1 or 1.5, the size ratio begins to plateau such that the effective radius tends to a value between 10 and 20 times the size of the gyroradius. The argon data may begin to show a similar trend. Due to the mass of krypton, higher magnetic fields are required to magnetize the krypton ions to the same degree. However, the trend in the krypton data initially seems to follow the same pattern as seen in argon and neon. Thus, as ion magnetization increases, the initial data suggests that the size of the filaments may have some dependence on the size of the ion gyroradius.

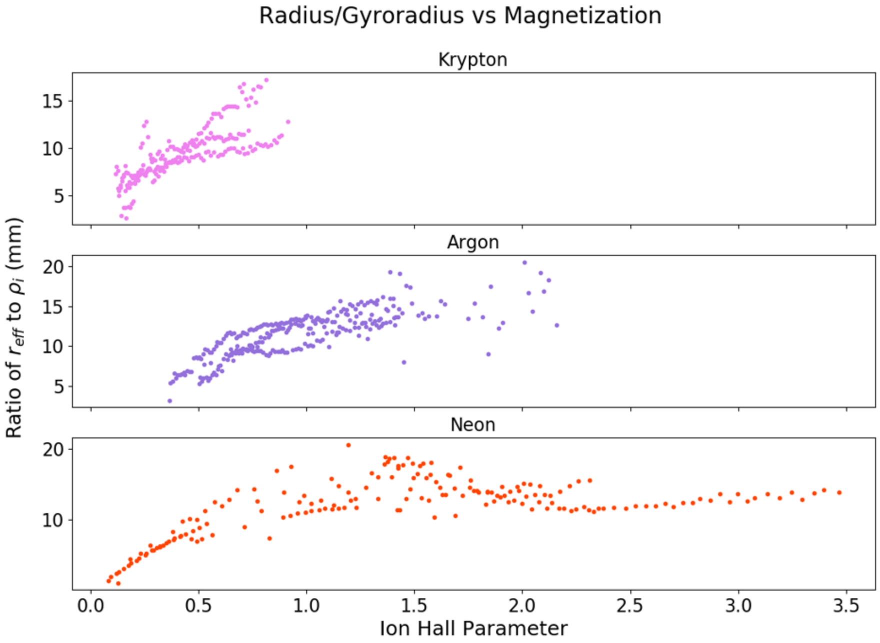

Figure 4.18: Ratio of the Type 1 (circular) filament effective radius to ion gyroradius as a function of ion Hall parameter. The size ratio initially increases nonlinearly with ion Hall parameter for all three plasma types. There is evidence that the size ratio may plateau to a value between 10 and 20 after the ions are magnetized (i.e. above a Hall parameter value of 1). This is more clear in neon, however there is some indication of this same trend in argon. Ratios in krypton initially show similarities, though higher magnetic fields are required to increase the magnetization of krypton ions.

Chapter 5

Summary and Future Studies

To summarize this work, all experiments were performed at Auburn University with the help of the Magnetized Plasma Research Lab (MPRL) group members in the MDPX lab. The project initially began with the intent to recreate the self-organizational plasma filament phenomenon, found in Max Planck, in the octagonal MDPX CCP chamber. This, and much more was accomplished during the scope of the filamentation project. In this final chapter, the project progression, success, additional work to be applied, and new configurations for single filament experiments will be discussed.

5.1 Summary of Work

In the first chapter, the filamentation phenomenon was introduced along with simulations which produced similar plasma instabilities. The phenomena was produced successfully in the MDPX facility with both a side view (for confirmation through comparison with the Max Planck experiment) and a top-down view of the plasma structures from above. It was shown that these structures were:

1. Confirmed to be the same filamentation phenomena first reported by Konopka et al.
2. In very well agreement with filament simulations produced by Mohamad et al. with MDPX device conditions which predicted the filamentation of the plasma from the side and from above.

Because filaments are created in high magnetic field environments, the charged particles are subject to imposed magnetic forces. These forces result in the charged particles transitioning from straight line motion to a gyromotion where the ions and electrons revolve around magnetic field lines with a certain frequency dependent on mass and the strength of the field. Additionally with low temperature, weakly ionized plasmas, there are three separate species of particles that exist in the same volume of space; the ions, electrons, and neutral atoms. The motion of the different species produces collisions that are dependent on the number of particles, the cross-sectional area of the different species, and their thermal velocity. The combination of these two concepts give rise to the Hall parameter which describes the magnetization of the plasma and scales with magnetic field and pressure.

Lastly, a brief theoretical framework was introduced to attempt to give a foundation for the formation of filament structures in a weakly ionized, low temperature plasma. The main contributor to the structure formation simulated in ECR plasmas was found to be the drift wave instability. When this simulation was adapted to MDPX conditions, the different mode solutions (l = 0, 2, 3, and 4) produced results that closely match to the filament structures seen in the experiments. Therefore, the notion of the drift wave instability was suggested to be used as a basis for the construction of a physical filament theory.

Next, chapter 2 explained the experimental hardware configuration. The main components of the experiment were the ocatgonal vacuum chamber in which CCPs were generated, and the MDPX device. The 4 T superconducting magnet provided the uniform magnetic fields required to produce the filaments. The vacuum configuration that was applied was a powered lower electrode, a floating upper electrode, and an FTO doped glass square placed in the cutout of the upper electrode to maintain a uniform potential across the electrode but also allow optical access into the plasma from above. The neutral gas system flows the selected gas type into the chamber and power is deposited into the chamber to create a coupatively coupled low temperature weakly ionized plasma. A description of the camera system for the Ximea 4 MP cmos and the associated camtool software was given such that two cameras were used to view and record the plasma; one from the side and the other from above. This system was successfully used to take single images and record videos of the plasmas created. No probes or dust were inserted into the chamber for the experiments to be performed.

Chapter 3 outlined and described the two-fold experiments performed on the MDPX device and the pre-processing method used to prepare the data for analysis. The first experiment involved scanning through neutral gas pressures, while holding magnetic field and power input constant, to explore the response of the structure to changes in pressure. The observations showed filaments exist within a range of neutral gas pressure and evolve in morphology over this range. This result agreed with the simulation predictions. The second experiment scanned through magnetic field space while holding neutral pressure and power input constant. The filament morphology changed with magnetic field suggesting that the morphology of the structures have some dependence on both magnetic field and pressure. *FIJI* was then used to extract image data for all filaments in the image stacks to prepare the data for a custom analysis code.

Finally, in chapter 4, the Python analysis method was presented in addition to a new, more robust improvement of the original analysis method. The Python code allowed for reliable categorization of filaments by shape where they can be classified as Type 1 through 4. Moreover, the code provided a raw count for the number of filaments by type as a function of magnetic field. The analysis lead to interesting results when comparing filament morphology behavior with the magnetization level of the ions (i.e. the ion Hall parameter). There may be evidence of a ”threshold condition” for each filament type in the plasmas tested in correlation to certain ion Hall parameter values.

Overall, the success of the filamentation project proved to be quite high. Results of this project provided the beginning steps to developing a working filament theory, filament regimes were well documented, new processing methods were developed, and a possible correlation to the ion Hall parameter was uncovered. These new and exciting avenues provide more insight into the filament instabilities that were first reported nearly 20 years ago. While there is much information extracted throughout this project, much more work remains to give a complete physical picture of the plasma filamentation phenomenon.

5.2 Filament Dynamics

This dissertation project was formed to exclusively explore the morphology of plasma filaments in different neutral gas species and the general dependence on plasma conditions. Because of the bounds of the project purpose imposed, this project only presents singular snapshots in time of the system under different plasma conditions. Although this was successful in exploring the structural morphology, the full description of the filament phenomena must include the morphology in addition to the temporal dynamics exhibited by the filaments.

At any point in time in which filaments are formed, there are dynamic behaviors that are exhibited by each filament. These include both global and local temporal dynamics. When filaments are formed, it is observed that there is a common translational motion among the system of filaments. This motion generally seems to have some systemic ”slow” drift, typically on the order of a couple of millimeters per second. This could be a product of a global $E \times B$ drift imposed by the ambipolar diffusion of the plasma and the uniform magnetic field applied.

Although the filaments all seem to have a general global drift direction in common, there is also local motion for each of the filaments. The individual filaments also have local translational and rotational motion. Figure 5.1 is a montage of 10 images of a single filament over 10 seconds at a rate of one image taken every second (1 Hz). The figure shows an example of how a single filament can exhibit local rotational behavior. Additionally in figure 5.2, the rotational dynamics of four separate filaments in the same region of the system at a fixed power of $P_{RF} = 1$ W, a pressure of $p = 3.5$ Pa (26 mTorr), and a magentic field of $B = 2$ T is shown. There is a clear frequency of rotation with respect to the x-axis for all four filaments. However, they all seem to have slightly different angular velocities.

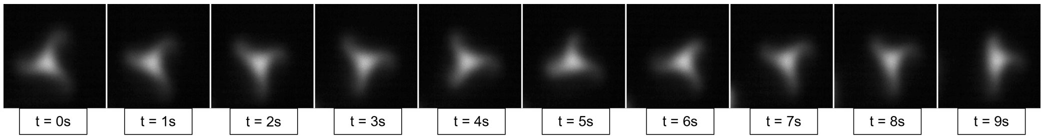

Figure 5.1: 10 second montage of a close-up of a single filament in an argon plasma. The images in the montage are taken at a frame rate of 1 image per second and show the dynamics of the local rotation of a Type 3 filament in the system. The filament is observed to rotate clockwise while roughly maintaining its geometric shape.

Because the filaments exhibit different rotational and translational motion even while existing within the same areas of the system (i.e. interfilamentary distance << system size), there may be local effects that lead to the differences in motion and morphology. These differences might be due to local changes in electric fields or local changes in densities. In a magnetized plasma, any electric field produced can lead to an $E \times B$ drift, while changes in density (i.e. pressure gradients) can lead to a $\nabla n \times B$ drift. If filaments are driven by drift wave instabilities which lead to gradients in density, as discussed in chapter 1, it may follow that these same gradients give rise to the $\nabla n \times B$ rotational drift behaviors observed.

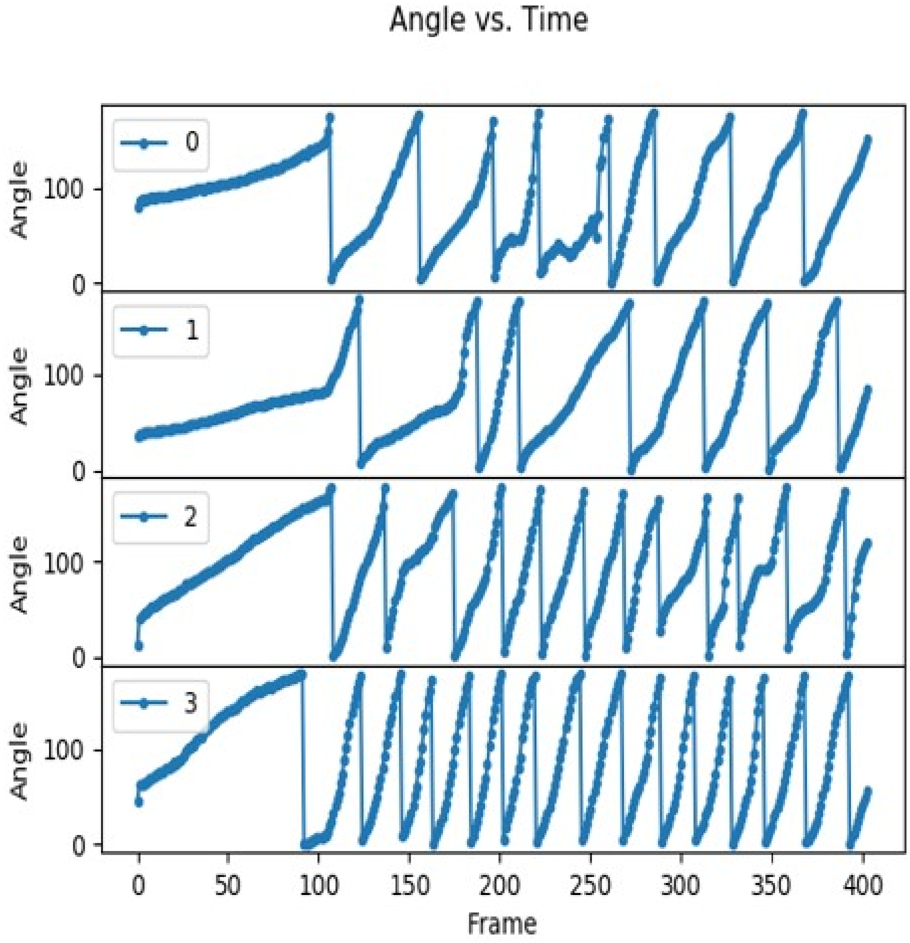

Figure 5.2: An illustration of the rotational dynamics for four separate filaments in the same region of the system over ten seconds (video was recorded at 40 frames per second). The degree angle ranges from 0 to 180, thus the "discontinuous" jumps shown is the axial tracking measurement along the x-direction reverting to the origin, but the filament continues to rotate. Therefore, one rotation can be defined to begin at one peak and complete a full rotation at every other peak. Moreover, even though the filaments are in the same area, they all seem to have slightly different angular velocities.

In addition to the temporal dynamics, filaments also exhibit the ability to ”appear” in the system out from the background plasma as well as ”disappear” into the background plasma. Moreover, two filaments can combine into one filament while the reverse process is also seen (one filament can split into two). All of these behaviors have been observed but more research must be conducted to gain a better understanding of the underlying physical mechanisms. Understanding the local dynamics may give additional clues to how the filaments are formed, maintained, and the reason for their shape morphology.

5.3 Filament Confinement

In more recent experiments, new configurations have led to filaments being confined to form within a designated region in the system. Using a conducting copper ring, it is believed that this imposes a potential well in which the filaments are then confined to. Figure 5.3 shows two different configurations that allow for filament confinement.

The ability to confine filaments and designate where individual filaments form can prove to be very useful in future experiments. It has been shown that filaments can affect dust dynamics and particle growth [15, 38]. Therefore, confining filaments to form in a specified location can give the researcher a more controlled experiment to compare dust data in filamented regions to that in non-filamented regions. In addition, there are challenges in diagnos-

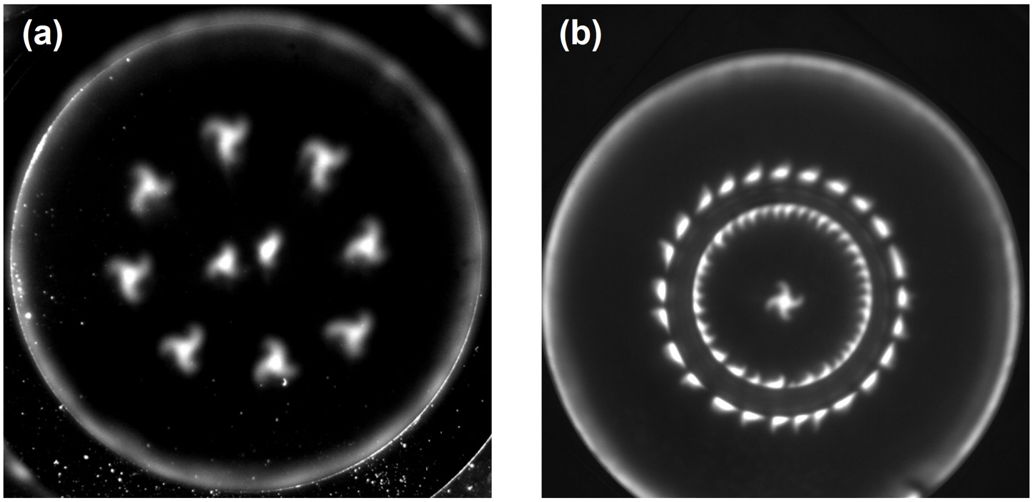

Figure 5.3: Images of argon filaments confined within a copper ring. (a) Filaments produced at 2 T with a neutral pressure of 4.6 Pa (35 mTorr) at 1 W of power. The filaments self-organized in a 3 $\frac{1}{4}$ inch outer diameter (OD) copper gasket with eight Type 3 filaments formed concentrically around two central filaments. (b) A single Type 4 filament confined in a 2 $\frac{1}{8}$ inch OD copper casket at a magnetic field of 2 T, pressure of 5.3 Pa (40 mTorr), and 2 W of power.

tics of filaments in the plasma. Some of these challenges include the mobility of individual filaments, the tendency for filaments to either be disrupted by, or form on, objects placed in the plasma (i.e. Langmuir probes, etc.), and the difficulty of using Langmuir probes at high magnetic fields as discussed in section 4.1.3. Ensuring that filaments form and remain in one location allows for exterior diagnostic techniques such as spectroscopy and Laser Induced Fluorescence (LIF).

Lastly, figure 5.4 shows that a singular filament can be confined and subsequently by changing neutral pressure - which also changes the ion/electron magnetization - a single filament can be observed to progress through different types of morphologies. Thus, external diagnostics and fast camera data may be able to provide additional information regarding the change of a filament from one morphology type to another.

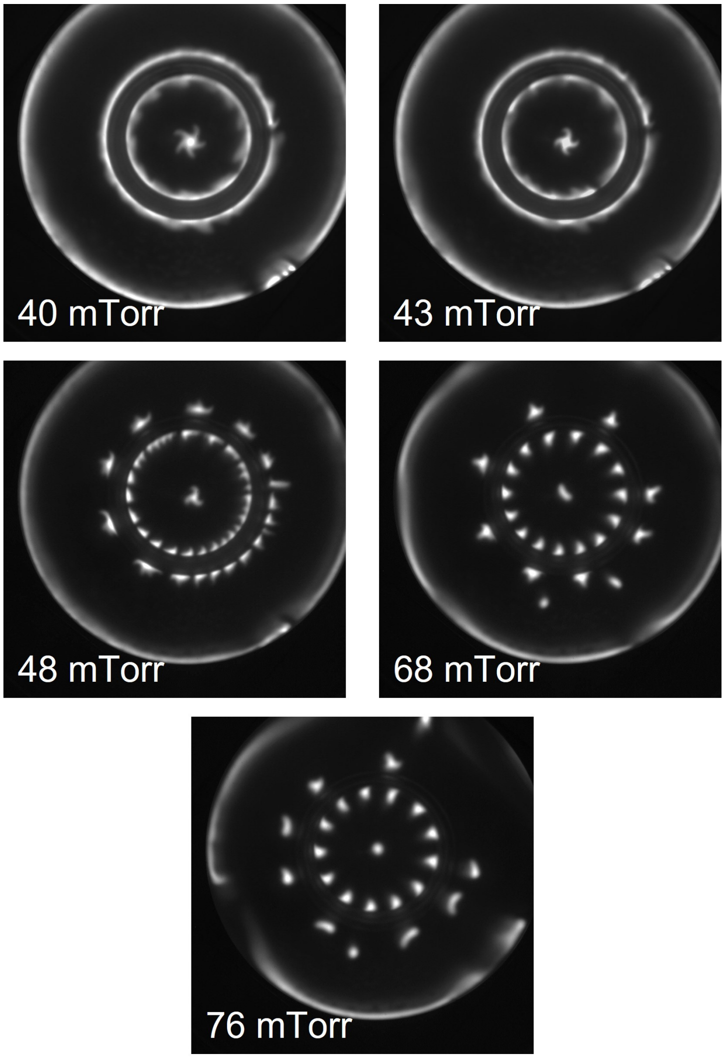

Figure 5.4: A single filament formed in the center of a $2\ \frac{1}{8}$ in OD copper gasket with a maintained magnet field of 2.5 T and power input of 2 W. The filament is formed and at 3.5 Pa (40 mTorr) a five-arm filament is observed (a newly observed filament type). Increasing the pressure in the system, the filament is seen to evolve through different morphologies.

Understanding filament dynamics can provide important information about the physical characteristics of the filaments themselves. Performing detailed experiments on confined singular filaments may reveal the underlying mechanisms that lead to the dynamics observed. Although there is still much more to be done to explain our observations, the filament phenomenon is much better understood as a result of this work. The pattern of self-organization is often seen in weakly ionized, low temperature plasmas in many systems, and filament studies can help to understand the fundamental actions that lead to the observed patterns. More importantly, the new physics being uncovered by these studies can be applied to a wider range of areas that incorporate low temperature plasmas. Ultimately, it is the role of science and its researchers to propel the community forward into the future with more understanding of our reality for the betterment of humanity. This work is intended to be a stepping stone in that long-lasting endeavor.

Bibliography

[1] Lewi Tonks. “The Birth of “Plasma””. In: *American Journal of Physics* 35.9 (Sept. 1967), pp. 857–858. DOI: `10.1119/1.1974266`.

[2] A. Piel and A. Meltzer. “Dusty plasmas - the state of understanding from an experimentalist’s view”. In: *Advances in Space Research* 29.9 (2002), pp. 1255–1264. DOI: `https://doi.org/10.1016/S0273-1177(02)00194-1`.

[3] A. Piel and A. Meltzer. “Dynamical processes in complex plasmas”. In: *Plasma Phys. Control. Fusion* 44.R1 (2002), pp. 1–26. DOI: `http://dx.doi.org/10.1088/0741-3335/44/1/201`.

[4] Robert L. Merlino and John A. Goree. “Dusty Plasmas in the Laboratory, Industry, and Space”. In: *Physics Today* 1.57 (2004), pp. 32–38. DOI: `https://doi.org/10.1063/1.1784300`.

[5] G. E. Morfill and H. Thomas. “Plasma crystal”. In: *Journal of Vacuum Science and Technology A* 14.2 (Mar. 1996), pp. 490–495. DOI: `http://doi.org/10.1116/1.580113`.

[6] S. Krasheninnikov, A. Smolyakov, and A. Kukushkin. “Dust in Fusion Plasmas”. In: *On the Edge of Magnetic Fusion Devices.* Springer International Publishing, 2020, pp. 89–113.

[7] S. Ratynskaia, A. Bortolon, and S. I. Krasheninnikov. “Dust and powder in fusion plasmas: recent developments in theory, modeling, and experiments”. In: *Reviews of Modern Plasma Physics* 6.1 (Aug. 2022). DOI: `10.1007/s41614-022-00081-5`.

[8] R. D. Smirnov et al. “Dust dynamics and radiation in fusion plasmas”. In: *2009 IEEE International Conference on Plasma Science - Abstracts.* 2009, p. 1. DOI: `10.1109/PLASMA.2009.5227235`.

[9] D. A. Mendis. “Dust in Cosmic Plasma Environment”. In: *Astrophysics and Space Science* 65 (1979), pp. 5–12.

[10] F. Verheest. “Waves and Instabilities in Dusty Plasmas”. In: *Space Science Reviews* 77 (1996), pp. 267–302.

[11] C. K. Goertz. “Dusty plasmas in the solar system”. In: *Reviews of Geophysics* 27.2 (1989), pp. 271–292. DOI: `https://doi.org/10.1029/RG027i002p00271`.

[12] T. Hall et al. “Methods for the characterization of imposed, ordered structures in MDPX”. In: *Phys. of Plasmas* 25.10 (Oct. 2018). DOI: `10.1063/1.5049594`.

[13] T. Hall and Jr. E. Thomas. “Dynamics of dust particles confined in imposed potential structures in strongly magnetized, low-temperature plasmas”. In: *Phys. Rev. E* 102 (2 Aug. 2020), p. 023208. DOI: `10.1103/PhysRevE.102.023208`.

[14] E. Thomas et al. “Preliminary characteristics of magnetic field and plasma performance in the Magnetized Dusty Plasma Experiment (MDPX)”. In: *J. Plasma Physics* 80.6 (2014), pp. 803–808. DOI: `https://doi.org/10.1017/S0022377814000270`.

[15] U. Konopka et al. “Complex Plasmas in Strong Magnetic Fields”. In: *AIP Conference Proceedings* 799.1 (2005), pp. 181–184. DOI: `https://doi.org/10.1063/1.2134595`.

[16] U. Konopka et al. “Circular, Spiral and Point-like Filamentation of a Magnetized, Radio Frequency Discharge”. In: *American Physical Society, 54th Annual Meeting of the APS Division of Plasma Physics* (2012).

[17] M. Schwabe et al. “Pattern Formation in a Complex Plasma in High Magnetic Fields”. In: *Phys. Rev. Lett.* 106 (21 May 2011), p. 215004. DOI: `10.1103/PhysRevLett.106.215004`.

[18] P. Bandyopadhyay et al. “Observation of spacio-temporal pattern in magnetised rf plasma”. In: *AIP Conference Proceedings* 1582.1 (2014), pp. 281–287. DOI: `https://doi.org/10.1063/1.4865365`.

[19] Francis F. Chen. *lntroduction to plasma physics and controlled fusion.* Springer Cham, 1974. ISBN: 978-3-319-22309-4.

[20] S. Khrapak. “Practical expression for an effective ion-neutral collision frequency in flowing plasmas of some noble gases”. In: *J. Plasma Physics* 79.6 (2013), pp. 1123–1124. DOI: `10.1017/S0022377813001025`.

[21] A. V. Phelps. *Phelps database.* URL: `https://us.lxcat.net/cache/646ee3fb54ab3/`. accessed: 10.12.2022.

[22] Spencer Leblanc. “Investigation of Probe-Induced Dust Voids in a Weakly Magnetized Dusty Plasma”. PhD thesis. Auburn University, 2019.

[23] Taylor Hall. “Microparticle Dynamics in the Presence of Externally Imposed, Ordered Structures in a Magnetized Low Temperature Plasma”. PhD thesis. Auburn University, 2019.

[24] Mohamad Menati. “Filamentation and Formation of Imposed Patterns in Low Pressure Magnetized Electric Discharges: A Numerical Approach”. PhD thesis. Auburn University, 2020.

[25] T. Ikehata et al. “Persistent Spiral-Arm Structure of a Rotating Plasma in a Stationary Gas”. In: *Phys. Rev. Lett.* 81.9 (Aug. 1998), pp. 1853–1856.

[26] Y. Amagishi, Y. Yoshikawa, and J. Ohara. “Shear-Flow Instabilities of a Rotating Mercuryin Presence of a Magnetic Field”. In: *J. Phys. Soc. Jpn.* 60 (1991), pp. 2496–2499.

[27] M. Menati, E. Thomas, and M. Kushner. "Filamentation of capacitively coupled plasmas in large magnetic fields". In: *Physics of Plasmas* 26.6 (June 2019).

[28] M. Menati et al. "Experimental observation and numerical investigation of filamentary structures in magnetized plasmas". In: *Physics of Plasmas* 27.2 (Feb. 2020), p. 022101. DOI: `10.1063/1.5135761`.

[29] M. S. Barnes, T. J. Cotler, and M E. Elta. "A staggered-mesh finite-difference numerical method for solving the transport equations in low pressure rf glow discharges". In: *Journal of Computational Physics* 77.1 (1988), pp. 53–72. DOI: `https://doi.org/10.1016/0021-9991(88)90156-8`.

[30] S. Williams et al. "Experimental observations of multiple modes of filamentary structures in the magnetized dusty plasma experiment (MDPX) device". In: *Physics of Plasmas* 29.1 (Jan. 2022). DOI: `10.1063/5.0065516`.

[31] A. Okamoto et al. "Multipole Vortices in an ECR Plasma". In: *J. Plasma Fusion Res. SERIES* 4 (2001), pp. 363–367.

[32] M. Kono and M. Tanaka. "Spiral Structures in Rotating Plasmas". In: *Phys. Rev. Lett.* 84.19 (May 2000), pp. 4369–4372. DOI: `10.1103/PhysRevLett.84.4369`.

[33] T. Ikehata et al. “Persistent Spiral-Arm Structure of a Rotating Plasma in a Stationary Gas”. In: *Phys. Rev. Lett.* 81 (0 Aug. 1998), pp. 1853–1856. DOI: `10.1103/PhysRevLett.81.1853`.

[34] M. Tanaka and M. Kono. “Spiral Pattern Formation in a Rotating Cylindrical Plasma”. In: *J. Plasma Fusion Res. SERIES* 4 (Oct. 2001), pp. 131–137.

[35] L. V. Shubnikov and Yu. N. Ryabinin V. I. Khotkevich Yu. D. Shepelev. “Magnetic Properties of Superconducting Metals and Alloys”. In: *Zh. Eksper. Teor. Fiz.* 7 (1937), pp. 221–237.

[36] M. Tinkham. *Introduction to Superconductivity: Second Edition*. NY: McGraw-Hill, 1996. ISBN: 0486435032.

[37] J. Schindelin, I. Arganda-Carreras, and E. Frise et al. “Fiji: an open-source platform for biological-image analysis.” In: *Nat Methods* 9 (2012), pp. 676–682. DOI: `10.1038/nmeth.2019`.

[38] E. Thomas et al. “The impact of plasma pattern formation on particle growth in strongly magnetized, low temperature plasmas”. In: *APS Annual Gaseous Electronics Meeting Abstracts*. 2021, KW74–001.

Appendix A

FIJI Custom Macro

This appendix explains the macro that was built to record each pixel value and its location in every image in an image stack. The purpose was to pre-process the data and store the information in a user-friendly way in order to upload the information into a custom built python code that allowed for a more robust filament analysis.

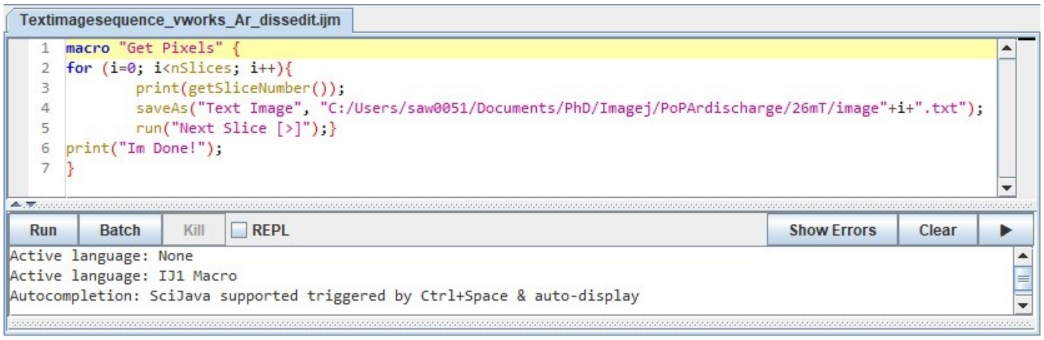

```
macro "Get Pixels" {
for (i=0; i<nSlices; i++){
	print(getSliceNumber());
	saveAs("Text Image", "C:/Users/saw0051/Documents/PhD/Imagej/PoPArdischarge/26mT/image"+i+".txt");
	run("Next Slice [>]");}
print("Im Done!");
}
```

```
Active language: None
Active language: IJ1 Macro
Autocompletion: SciJava supported triggered by Ctrl+Space & auto-display
```

Figure A.1: Custom FIJI macro which enables the user to save all pixel values and pixel location for any number of images in an image stack.

Appendix B

Argon Analysis Scheme

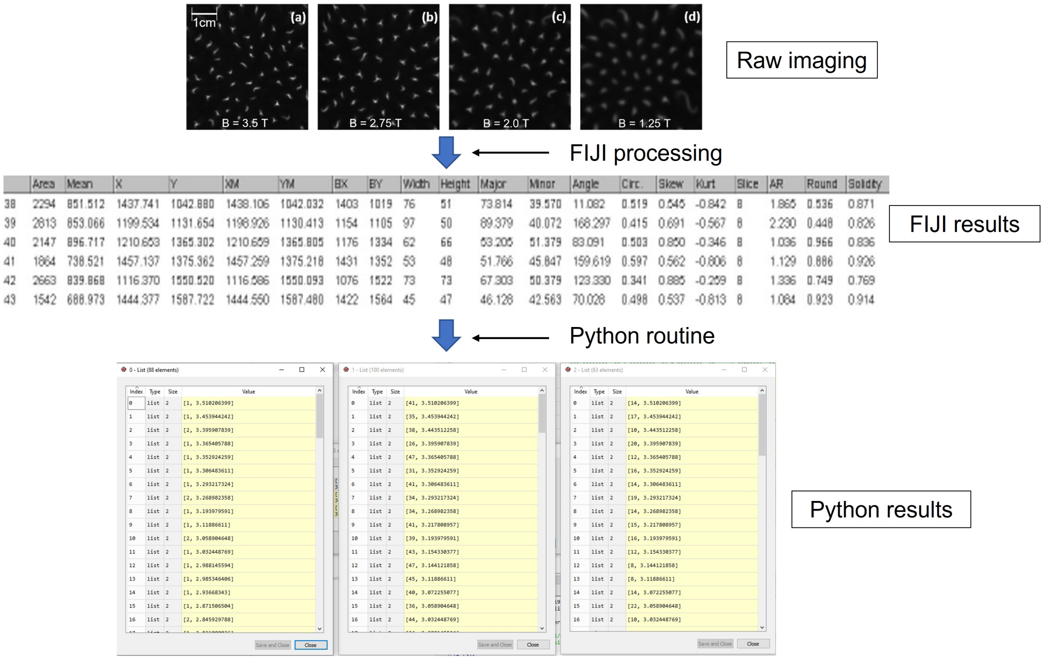

	Area	Mean	X	Y	XM	YM	BX	BY	Width	Height	Major	Minor	Angle	Circ.	Skew	Kurt	Slice	AR	Round	Solidity
38	2294	851.512	1437.741	1042.880	1438.106	1042.032	1403	1019	76	51	73.814	39.570	11.082	0.519	0.545	-0.842	8	1.865	0.536	0.871
39	2813	853.066	1199.534	1131.654	1198.926	1130.413	1154	1105	97	50	89.379	40.072	168.297	0.415	0.691	-0.567	8	2.230	0.448	0.826
40	2147	896.717	1210.653	1365.302	1210.609	1365.805	1176	1334	62	66	53.205	51.379	83.091	0.503	0.850	-0.346	8	1.036	0.966	0.836
41	1864	738.521	1457.137	1375.362	1457.259	1375.218	1431	1352	53	48	51.766	45.847	159.619	0.597	0.562	-0.806	8	1.129	0.886	0.926
42	2663	839.868	1116.370	1550.520	1116.586	1550.093	1076	1522	73	73	67.303	50.379	123.330	0.341	0.885	-0.259	8	1.336	0.749	0.769
43	1542	688.973	1444.377	1587.722	1444.550	1587.480	1422	1564	45	47	46.128	42.563	70.028	0.498	0.537	-0.813	8	1.084	0.923	0.914

0 - List (88 elements)

Index	Type	Size	Value
0	list	2	[1, 3.510206399]
1	list	2	[1, 3.453944242]
2	list	2	[2, 3.395907839]
3	list	2	[1, 3.365405788]
4	list	2	[1, 3.352924259]
5	list	2	[1, 3.306483611]
6	list	2	[1, 3.293217324]
7	list	2	[2, 3.268982358]
8	list	2	[1, 3.193979591]
9	list	2	[1, 3.11886611]
10	list	2	[2, 3.058904648]
11	list	2	[1, 3.032448769]
12	list	2	[1, 2.988145594]
13	list	2	[1, 2.985346406]
14	list	2	[1, 2.93668343]
15	list	2	[1, 2.871506504]
16	list	2	[2, 2.845929788]

1 - List (100 elements)

Index	Type	Size	Value
0	list	2	[41, 3.510206399]
1	list	2	[35, 3.453944242]
2	list	2	[38, 3.443512258]
3	list	2	[26, 3.395907839]
4	list	2	[47, 3.365405788]
5	list	2	[31, 3.352924259]
6	list	2	[41, 3.306483611]
7	list	2	[34, 3.293217324]
8	list	2	[34, 3.268982358]
9	list	2	[41, 3.217808957]
10	list	2	[39, 3.193979591]
11	list	2	[43, 3.154330377]
12	list	2	[47, 3.144121858]
13	list	2	[45, 3.11886611]
14	list	2	[40, 3.072255077]
15	list	2	[36, 3.058904648]
16	list	2	[44, 3.032448769]

2 - List (63 elements)

Index	Type	Size	Value
0	list	2	[14, 3.510206399]
1	list	2	[17, 3.453944242]
2	list	2	[10, 3.443512258]
3	list	2	[20, 3.395907839]
4	list	2	[12, 3.365405788]
5	list	2	[16, 3.352924259]
6	list	2	[14, 3.306483611]
7	list	2	[19, 3.293217324]
8	list	2	[14, 3.268982358]
9	list	2	[15, 3.217808957]
10	list	2	[16, 3.193979591]
11	list	2	[12, 3.154330377]
12	list	2	[8, 3.144121858]
13	list	2	[8, 3.11886611]
14	list	2	[14, 3.072255077]
15	list	2	[22, 3.058904648]
16	list	2	[10, 3.032448769]

Figure B.1: This figure shows the flow of data for the argon analysis presented in chapter 4 section 4.1. The raw data captured by the Ximea camera is pictured at the top. The Fiji pre-processing steps are then used to produce a Results window where the tagged filaments are presented with the shape information and their stack position (i.e. image number). Subsequently, the information in the results window is uploaded into python where the custom routine outputs the results into three different lists (a sample of that list is shown in the bottom of the figure). Each list describes the three filament types and contains the stack position, the number of filaments of that type in each stack, and the magnetic field strength for the stack number. The first list (from left to right) is corresponds to Type 1, the second Type 2, and the third is Type 3.

Appendix C

Python Method

To achieve a more rubust analysis method that relied on raw data as opposed to the *FIJI* shape parameter outputs, an *FIJI* macro was built to store each 16-bit image in terms of its pixel values as a .txt file. After storing the raw images successfully, the *ANALYZE PARTCILES* plug-in method is implemented to retrieve the results window. Recall, the wand tool used in the plug-in successfully identifies objects in the image scan and outputs useful information for each object. The plug-in outputs X and Y pixel coordinates for the center of mass of each filament in addition to a ”Bounding Rectangle” which is the smallest rectangle that encloses the object. The coordinates of the upper left corner of the rectangle is also given in the results window. The results window is saved as an excel file as previously done in the argon analysis method.

The new routine uploads the results window and the 16-bit image files of pixel values into the terminal and the image files are sorted correctly by image number. This is important because the routine will cross reference the stack number (i.e. the image number) of the filament and store each filament array in a dictionary list keyed by the stack (image) number. The bounding rectangle dimensions are used to specify a unique constant radius, r, for each filament that is used for the circular walk implemented for the filament analysis. Given a raw image file, the code uses the center of mass X and Y position output for each filament from the *FIJI* preprocessing and sets that position as the origin for the radius determined above. Next, the angle is set to 0 and then a sequence of polar coordinates is used to output the raw value of the pixel given by the radius for the range of angle from 0 to 360. This process is repeated for each filament in the array list for each dictionary key until all keys (i.e. all images) are processed. This is illustrated in figure 3.8(a). The array of pixel values for each filament is stored in a dictionary keyed by image number.

After the raw pixel values are stored, the routine takes each array and applies a smoothing function to smooth the raw data. The results of the smoothing process is shown in figure 3.8(b). When smoothed, the relevant intensity peaks within the array are located, stored, and the total number of peaks is counted. A series of conditional statements is implemented to accurately interpret the peak information algorithmically including if no peaks exist. The routine counts the peaks according to the conditional statements and stores the information accordingly for every filament in every image.

After each image is processed the number of filaments of each type can be plotted as in the argon analysis.